OPEN SOURCE NMR RELAXOMETRY PLATFORM

by

MICHAEL TWIEG

Submitted in partial fulfillment of the requirements

For the degree of Master of Science

Thesis Adviser: Dr. Mark Griswold

Department of Electrical Engineering and Computer Science

CASE WESTERN RESERVE UNIVERSITY

January 2013

CASE WESTERN RESERVE UNIVERSITY

SCHOOL OF GRADUATE STUDIES

We hereby approve the thesis/dissertation of

Michael Twieg

Master of Science
candidate for the _____degree *.

Mark Griswold
(signed)_____
(chair of the committee)

Kenneth Loparo
_____

Francis Merat
_____

_____

_____

_____

July 23, 2012
(date) _____

*We also certify that written approval has been obtained for any
proprietary material contained therein.

Table of Contents

List of tables

List of figures

Acknowledgements

Open Source NMR Relaxometry Platform

Abstract

by

MICHAEL TWIEG

We present a low cost, open source hardware platform for use in NMR relaxometry experiments. The platform is capable of a wide variety of relaxometry experiments comprising many magnet, coil, and sample combinations. The majority of the RF chain is broadband, allowing operation over a large frequency range with only minor adjustments to the hardware. Experiments can be performed in a host-controlled mode in conjunction with a PC, or in a standalone mode for mobile applications. The high degree of flexibility and low cost of the platform makes NMR relaxometry accessible to applications where cost, size, or flexibility were previously prohibitive. The system is based on off-the-shelf components, along with some custom-fabricated parts, and can be replicated by engineers with suitable skills and resources. The design of the platform is open source.

Chapter 1: NMR relaxometry theory and applications

1-1 Content overview

Chapter one introduces the field of NMR relaxometry and its application. The basic principles of NMR physics will be introduced, including magnetization, precession, relaxation, and spin echoes. The Bloch equations and the effects of self diffusion will also be derived. The influence of static field inhomogeneity and its impact on NMR relaxometry will also be addressed. Finally, the field of NMR relaxometry and some of its various applications will be discussed.

Chapter two describes the general hardware aspects of NMR systems. A generalized NMR system will be divided into its basic components, and their roles within the NMR system are discussed separately. We will show how the specifications for each component are determined according to the specific requirements and limitations of the application, and how we implement our hardware according to these specifications. Finally, we will evaluate the performance of each component and its impact on the overall system performance.

Chapter three covers the theory and implementation of NMR relaxometry experiments on our platform. First we will discuss various pulse sequences and how they can be used to obtain contrast according to various relaxation mechanisms. Secondly we will explain how pulses are synthesized and how NMR signals are sampled with the actual platform hardware, and how these events are combined into the desired sequences. Thirdly, we will explore how the sequences are executed by the platform firmware, and how sequences and experiments are defined within the firmware. Finally, we will discuss

the user interfaces featured in the platform, and how data is stored and transferred within the platform and between the platform and host.

Chapter four discusses the analysis of the overall platform performance and experimental results. First we will discuss how sampled data from the platform is analyzed using Fourier transforms and curve fitting algorithms. Secondly, we will explain how sequence parameters can be calibrated for best performance. Thirdly, we compare empirical measurements of signal to noise ratio and flip angle calibration with theoretical predictions. Finally, we will demonstrate several examples of relaxometry experiments and discuss their results.

Chapter five will provide an overview of the platform's specifications and applications. Potential improvements to the platform hardware will be discussed. Finally, we will speculate on future applications for the platform in research.

1-2 Introduction

Since its discovery, nuclear magnetic resonance (NMR) has shown to be an excellent method of observing the nature and behavior of matter on the molecular scale. While NMR was at first studied only within the fields of physics and chemistry, it has since spread to a wide variety of disciplines and industries. Currently the most well known application of NMR is medical magnetic resonance imaging (MRI), but it has also found applications such as the investigation of molecular structures, porous media, quality control for food products, inspection of polymer quality, and many more [2–10].

NMR is a particularly powerful tool because, given the correct magnet and coil configuration, it can non-invasively penetrate into objects and provide spatial maps of

many different material properties (which is the basis of MRI). Despite its power of insight, it does not require any chemical reactions to occur and does not use any ionizing radiation, and is thus a completely nondestructive method.

Arguably NMR's greatest weakness is the cost and complexity associated with the various hardware components required to perform many studies. However, many simple studies, especially those that do not require imaging, have much simpler requirements that can be satisfied at lower cost. One subset of NMR studies with such low requirements is NMR relaxometry. Despite its relative simplicity, NMR relaxometry can provide valuable insight into many physical and chemical processes and structures.

The main motivation for the development of our relaxometry platform was to make NMR relaxometry more accessible to researchers by lowering the cost and complexity of the hardware, while still offering high performance and flexibility. The platform allows for a wide variety of applications with various field strengths, magnet and coil geometries, and samples. A secondary goal was to construct a system that was small and portable, such that it could even be worn. As designed, the platform can be used with its own battery, and it is small and light enough for mobile applications. The platform is compatible with a large variety of different magnet and coil designers, customized for the relaxometry application. However, the main magnet for such a system is typically highly inhomogeneous, and requires specialized acquisition techniques to ensure that the required signals are received with high sensitivity.

1-3 Fundamentals of NMR physics

Sample magnetization

The basis of NMR is that atomic particles possess a net spin, characterized by the spin quantum number (*s* in the context of electrons, *I* in the context of nucleons). The spin quantum number is quantized, and has allowed values of positive integers and half integers. We will restrict our discussion to protons (in the form of hydrogen ^{1}H), and therefore use *I* as the spin quantum number, which has a value of ½. The secondary spin quantum number m_I describes the magnitude and direction of the angular momentum of the nuclear spin, and can have values from –*I* to +*I* in integer steps. The spin of the particle gives rise to a magnetic moment μ, which is given by:

$$\mu = \gamma m_I \hbar$$
<div align="right">Equation 1-3-1</div>

Where γ is the gyromagnetic ratio of the nucleus ($\gamma = 267.5\,rad/s$ for ^{1}H) and $\hbar$ is the reduced Planck's constant. For nuclei with no orbital angular momentum (such as ^{1}H), this can also be written as:

$$\vec{\mu} = \gamma \vec{I}$$
<div align="right">Equation 1-3-2</div>

Where $\vec{I}$ is the spin angular momentum vector. In the absence of an external magnetic field, the different spin states described by m_I are degenerate, meaning that all states occupy the same energy level. At thermal equilibrium the members of a population of nuclei will have their states evenly distributed, and the net m_I, and the net magnetization of the population, will be zero [11].

If an external, static magnetic field $\vec{B}_0$ is introduced to the population of nuclei, the different states m_I will no longer have the same energy level, and thus the population

of spins will be biased parallel to $\vec{B_0}$. The spins will effectively polarize themselves to align with $\vec{B_0}$, giving rise to a net equilibrium magnetization $\vec{M_0}$ [12]:

$$\vec{M}_0 = N\gamma^2\hbar^2 I(I+1)\frac{\vec{B_0}}{3kT} \qquad \text{Equation 1-3-3}$$

Where N is the number of spins per unit volume, I is the nuclear spin quantum number ($I = \frac{1}{2}$ for ^{1}H), k is Boltzmann's constant, and T is temperature.

The coordinate system describing a NMR experiment is typically defined such that $\vec{B_0}$ is aligned with the $\hat{z}$ direction. Therefore from here on the static field $\vec{B_0}$ will be referred to simply as B_0, and it will be assumed that it is in the $\hat{z}$ direction.

Larmor precession

When a macroscopic magnetization exists, the basic theory of nuclear precession can be adequately described with classical, rather than quantum mechanics. A magnetic moment $\vec{\mu}$ will experience a torque $\vec{\Gamma}$ in the presence of an external magnetic field $\vec{B}$:

$$\vec{\Gamma} = \vec{\mu} \times \vec{B} \qquad \text{Equation 1-3-4}$$

The torque results in a change in the angular momentum vector $\hat{I}$:

$$\frac{d\vec{I}}{dt} = \vec{\Gamma} \qquad \text{Equation 1-3-5}$$

Combining equations 1-3-2, 1-3-4, and 1-3-5 yields the following:

$$\frac{d\vec{\mu}}{dt} = \gamma\vec{\mu} \times \vec{B} \qquad \text{Equation 1-3-6}$$

Equation 1-3-6 states that when a nuclear moment $\vec{\mu}$ and $\vec{B}$ are not aligned, $\vec{\mu}$ will rotate around $\vec{B}$ with a frequency equal to ω [11]:

$$\omega = \gamma B \qquad\qquad \text{Equation 1-3-7}$$

This phenomenon is called precession, and ω is known as the precession angular frequency. We may rewrite equation 1-3-6 by splitting $\vec{\mu}$ and $\vec{B}$ into their longitudinal and complex transverse components:

$$\mu_z = \vec{\mu} \cdot \hat{z} \qquad\qquad \text{Equation 1-3-8}$$

$$\mu_{xy} = \vec{\mu} \cdot (\hat{x} + i\hat{y}) \qquad\qquad \text{Equation 1-3-9}$$

$$B_z = \vec{B} \cdot \hat{z} \qquad\qquad \text{Equation 1-3-10}$$

$$B_{xy} = \vec{B} \cdot (\hat{x} + i\hat{y}) \qquad\qquad \text{Equation 1-3-11}$$

$$d\mu_z(t)/dt = i\gamma/2 \left[\mu_{xy}(t)B_{xy}^*(t) - \mu_{xy}^*(t)B_{xy}(t) \right] \qquad\qquad \text{Equation 1-3-12}$$

$$d\mu_{xy}(t)/dt = -i\gamma \left[\mu_{xy}(t)B_z(t) - \mu_z(t)B_{xy}(t) \right] \qquad\qquad \text{Equation 1-3-13}$$

If we consider the case where $\vec{B}$ is static with magnitude B_0 and is aligned with the $\hat{z}$ direction, we find that equations 1-3-12 and 1-3-13 reduce to:

$$d\mu_z(t)/dt = 0 \qquad\qquad \text{Equation 1-3-14}$$

$$d\mu_{xy}(t)/dt = -i\gamma\mu_{xy}(t)B_0 \qquad\qquad \text{Equation 1-3-15}$$

Which have the solutions:

$$\mu_z(t) = \mu_z(0) \qquad\qquad \text{Equation 1-3-16}$$

$$\mu_{xy}(t) = \mu_{xy}(0)e^{-i\omega_0 t} \qquad\qquad \text{Equation 1-3-17}$$

Where $\omega_0 = \gamma B_0$ is the Larmor precession frequency [11].

These equations are valid in the laboratory reference frame, which is stationary. However, a more convenient way of describing NMR magnetization is with the rotating

6

reference frame, in which the coordinate system rotates in the transverse plane at an angular frequency Ω, which is normally set to be equal to ω_0. Coordinates and variables in the rotating reference frame are denoted with ' (for example $\hat{x}'$, B_1', μ_{xy}', etc). For the case where $\Omega = \omega_0$, equations 1-3-12 and 1-3-13 become:

$$d\mu_z(t)\Big/dt = i\gamma\Big/2 \left[\mu_{xy}'(t)B_{xy}'^*(t) - \mu_{xy}'^*(t)B_{xy}'(t)\right] \qquad \text{Equation 1-3-18}$$

$$d\mu_{xy}'(t)\Big/dt = i\gamma\mu_z(t)B_{xy}'(t) \qquad \text{Equation 1-3-19}$$

And for our case of simple Larmor precession, equations 1-3-16 and 1-3-17 reduce to:

$$\mu_z(t) = \mu_z(0) \qquad \text{Equation 1-3-20}$$

$$\mu_{xy}'(t) = \mu_{xy}'(0) \qquad \text{Equation 1-3-21}$$

We can see that the Larmor precession component of the transverse magnetization has disappeared from the equations [11]. The transverse magnetization is still precessing in the laboratory frame, but is stationary in the rotating reference frame.

Excitation via an RF magnetic field

Now we will consider the case where, in addition to the static field B_0, we introduce a circularly polarized magnetic field in the transverse plane with magnitude B_1.

$$B_{xy}(t) = B_1 e^{-i\omega_0 t} \qquad \text{Equation 1-3-22}$$

When expressed in the rotating reference frame, B_1 is constant and points in the $\hat{x}'$ direction:

$$B_{xy}'(t) = B_1 \qquad \text{Equation 1-3-23}$$

The differential equations 1-3-18 and 1-3-19 then become:

$$\frac{d\mu_z(t)}{dt} = \frac{i\gamma}{2} B_1 \left[\mu'_{xy}(t) - \mu'^*_{xy}(t) \right] \qquad \text{Equation 1-3-24}$$

$$\frac{d\mu_z(t)}{dt} = \gamma \mu'_y B_1 \qquad \text{Equation 1-3-25}$$

$$\frac{d\mu'_{xy}(t)}{dt} = i\gamma \mu_z(t) B_1 \qquad \text{Equation 1-3-26}$$

We can see that these equations describe rotation of the magnetization around the $\hat{x}'$ direction in the rotating frame. The rate of this precession ω_1 is given by $\omega_1 = \gamma B_1$ [11]. This precession describes how RF fields are able to manipulate magnetization, for example by tipping it from the longitudinal axis $\hat{z}$ into the transverse plane. RF fields are needed to perturb the equilibrium longitudinal magnetization into the transverse plane in order for precession to be detected.

An RF pulse is primarily characterized by its flip angle, which describes the overall rotation of $\vec{\mu}$ about $\vec{B}_1$. For example, a RF pulse with a flip angle of 90° may rotate longitudinal magnetization completely into the transverse plane, and a 180° pulse may invert longitudinal magnetization into the $-\hat{z}$ direction.

NMR relaxation and the Bloch equations

The previous equations describing Larmor precession are valid for an idealized magnetic moment $\vec{\mu}$. However, in real NMR experiments we consider the overall magnetization $\vec{M}$ from a sample, which is composed of the contributions of many spins each with their own $\vec{\mu}$ [11]. Large populations of spins undergo relaxation processes that do not occur for isolated spins.

Longitudinal relaxation, also called spin-lattice relaxation or T_1 relaxation, is the process by which the longitudinal component of $\vec{M}$ approaches its thermal equilibrium

value M_0 (see equation 1-3-3). Longitudinal magnetization obeys the following linear differential equation:

$$dM_z(t)\Big/dt = \frac{M_0 - M_z(t)}{T_1}$$

Equation 1-3-27

So longitudinal relaxation takes the form of an exponential decay towards M_0 with a time constant equal to T_1 [11].

Transverse relaxation, also called spin-spin relaxation or T_2 relaxation, is the process by which the transverse component of $\vec{M}$ approaches zero. Transverse relaxation obeys the following linear differential equation:

$$dM_{xy}(t)\Big/dt = \frac{-M_{xy}(t)}{T_2}$$

Equation 1-3-28

So transverse relaxation takes the form of an exponential decay towards zero with a time constant equal to T_2 [11].

Relaxation can be integrated into the previous equations in the following way:

$$dM_z(t)\Big/dt = i\gamma\Big/2 \left[M'_{xy}(t)B'^{*}_{xy}(t) - M'^{*}_{xy}(t)B'_{xy}(t) \right] + \frac{M_0 - M_z(t)}{T_1}$$

Equation 1-3-29

$$d\mu'_{xy}(t)\Big/dt = i\gamma M_z(t)B'_{xy}(t) - \frac{M'_{xy}(t)}{T_2}$$

Equation 1-3-30

These are the fundamental Bloch equations in the rotating reference frame, simplified for on-resonance magnetization. Equation 1-3-31 below shows the correct equation for M'_{xy} when off resonance is considered:

$$dM'_{xy}(t)\Big/dt = i\gamma M_z(t)B'_{xy}(t) - i\Delta\omega M'_{xy}(t) - \frac{M'_{xy}(t)}{T_2}$$

Equation 1-3-31

Where $\Delta\omega$ is the off resonance frequency [11].

9

The earliest NMR experiments were performed with continuous RF excitation, while continuous absorption [13] or emission [14] of energy due to Larmor precession was observed. Later on, experiments used pulsed RF to quickly tip, or excite, longitudinal magnetization into the transverse plane, and it was found that precession persisted long after the end of the RF pulse itself. The precession which persists after an excitation pulse is referred to as free induction decay, or FID [15].

Suppose that the static field B_0 is perfectly homogeneous ($\Delta\omega$ and ΔB_z are zero), and that the sample magnetization has reached its thermal equilibrium ($\vec{M} = M_0 \cdot \hat{z}$). If we apply a 90° excitation, then all of M_z will be tipped into the transverse plane where it precesses as a FID. The FID will decay according to T_2, and M_z will relax from zero back towards M_0 according to T_1.
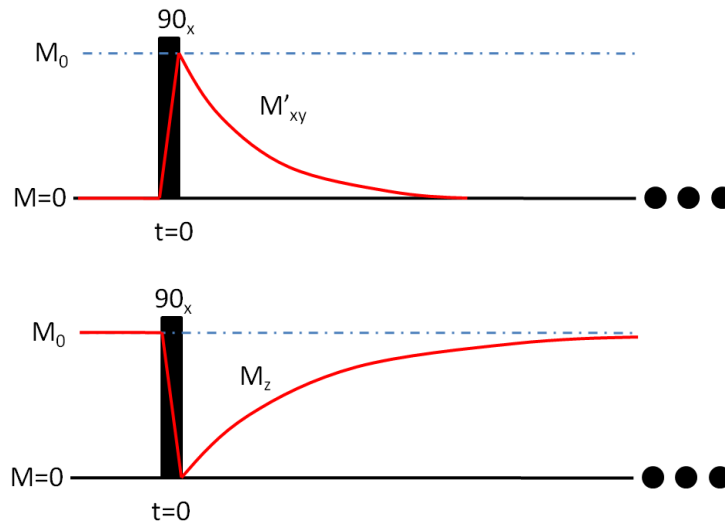
Figure 1-3-1) Diagrams of a simple FID experiment. At $t < 0$, M_z has reached the thermal equilibrium value M_0, and M_{xy} is 0. At $t = 0$, a 90° RF pulse in the $\hat{x}'$ direction tips all of M_z into M'_{xy}. a) shows the decay of M'_{xy} (solid red line) according to T_2 b) shows the regrowth of M_z (solid red line) towards M_0 (dashed blue line) according to T_1.

Transverse relaxation and longitudinal relaxation are relevant because they provide a macroscopic fingerprint of microscopic phenomenon in the environment of the spins. The exact mechanisms of this relaxation are beyond the scope of this work, but there are

countless examples of prior studies that confirm that NMR relaxation can provide key insight into the environment of a material at a molecular scale.

B_0 inhomogeneity and T_2*

In the case where the static field is not perfectly homogeneous within the volume of a sample under test (SUT), the macroscopic behavior of the transverse magnetization will differ from the ideal FID. This is because any field inhomogeneity will result in a frequency inhomogeneity, which will contribute to dephasing of the spins within the SUT. This results in an apparent change to the shape of the overall FID. The exact shape of the FID will depend on the exact nature of the inhomogeneity, but the overall result is that the FID will decay at a rate faster than its spin-spin relaxation rate T_2. The new inhomogeneity-weighted decay time constant is referred to as T_2* (even though this does not necessarily obey a purely exponential decay [11]).
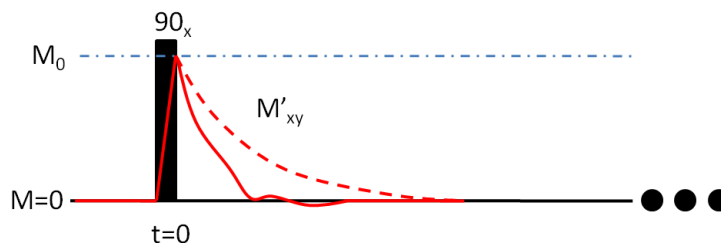
Figure 1-3-2) Distortion of the FID due to B_0 inhomogeneity results in an effective T_2* which is less than T_2. The shape of this FID will depend on the specific nature of the inhomogeneity, and may not be exponential. The dashed red line shows a hypothetical FID in a homogeneous field, while the solid red line shows the FID in the presence of field inhomogeneity.

In many cases, inhomogeneity is so severe that T_2* is far less than T_2, making observation of T_2 impossible from a simple FID experiment. In such cases, spin echoes must be used to rephase the magnetization.

Spin echoes

      The Hahn echo (sometimes referred to simply as a spin echo) is a technique used to observe the FID in the presence of B_0 inhomogeneities, and was originally described by Erwin Hahn [16]. In a simple Hahn echo experiment, an excitation pulse in the $\hat{x}'$ direction occurring at $t = 0$ tips some or all of M_z into the transverse plane (initially in the $\hat{y}'$ direction). The transverse magnetization is allowed to precess and decay according to T_2^*. At some time $t = \tau$, there is another RF pulse with a tip angle of 180° (again in the $\hat{x}'$ direction), called a refocusing pulse. The refocusing pulse rotates the magnetic moment $\vec{\mu}$ of each spin around the x' axis, such that their transverse moments become:

$$\overrightarrow{\mu'_{xy}}\left(\tau^+\right) = \overrightarrow{\mu'^*_{xy}}\left(\tau^-\right)$$
<div align="right">Equation 1-3-32</div>

This can also be viewed as a phase reversal of each spin:

$$\theta\left(\tau^+\right) = -\theta\left(\tau^-\right)$$
<div align="right">Equation 1-3-33</div>

After the refocusing pulse, each spin will continue to precess at its own off resonant frequency and in the same direction, but now instead of the phase of each spin continuing to diverge from zero, it will converge towards zero at the same rate. The result is that at time $t = 2\tau$, the phase of all spins will again be zero, and they will be coherent until they again dephase. Aside from the Hahn echo, there are various other spin echo types that rephase magnetization in their own way. However for the scope of this work, only Hahn echoes will be considered.
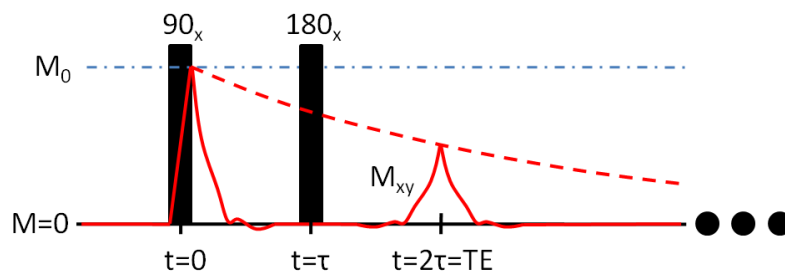
Figure 1-3-3) Diagram of a Hahn echo experiment. The amplitude of the spin echo (solid red line) at t=TE will be the same as the amplitude of the ideal FID without inhomogeneity (dashed red line).

Though the spin echo restores coherency in the spins at time $t = 2\tau$ (also called the echo time TE), transverse relaxation still occurs due to spin-spin relaxation during that time, and that loss in transverse magnetization cannot be restored by the refocusing pulse (because it is due to random processes which cannot be reversed). Thus the peak amplitude of the spin echo will still be weighted by T_2 decay. This allows T_2 weighted experiments to be performed even in the presence of strong inhomogeneity in B_0.

Self-diffusion

In a spin echo experiment performed in an inhomogeneous field, the amplitude of the spin echo at the echo time TE will be equal to the initial magnetization, attenuated by T_2 relaxation. This is the case when the Larmor precession frequency (and therefore $\Delta\omega$) of each spin remains constant throughout the experiment. If this is not the case, either due to motion of the nuclei or changes in ΔB_0 during the experiment, the time of the echo coherence, or the amplitude of the echo, may be altered. One particularly relevant example of this is molecular self-diffusion.

Self-diffusion is the phenomenon that describes the Brownian motion of particles in a medium when the overall chemical gradient is equal to zero. The self-diffusion coefficient D of some particles in a medium describes the mean square spatial deviation $\left\langle \delta^2 \right\rangle$ of the spins per unit time τ_d :

13

$$D = \frac{\left\langle \delta^2 \right\rangle}{2\tau_d}$$

Equation 1-3-34

Suppose the strength of our static field B_0 is not constant over space, and instead varies linearly in one arbitrary direction $\hat{g}$ such that its $\hat{z}$ component B_z as a function of position $\vec{r}$ is given by:

$$B_z(\vec{r}) = B_z(0) + G_0 \vec{r} \cdot \hat{g}$$

Equation 1-3-35

This is commonly referred to as a field gradient, where G_0 is called the gradient strength, in Teslas per meter. It can be found that if a population of spins is allowed to self diffuse with D in a linear gradient G_0 for time t, the spins will evolve with a random distribution of phase [11]:

$$\left\langle \phi^2 \right\rangle = \frac{G_0^2 \gamma^2 \left\langle \delta_{\hat{r}}^2 \right\rangle t^3}{3\tau_d} = \frac{2}{3} G_0^2 \gamma^2 D t^3$$

Equation 1-3-36

This dephasing causes a loss in overall transverse magnetization (ignoring the effects of T_2) according to [11]:

$$M_{xy}(t) = M_{xy}(0) e^{-\left\langle \phi^2 \right\rangle / 2}$$

Equation 1-3-37

$$M_{xy}(t) = M_{xy}(0) e^{-\frac{1}{3}\gamma^2 G_0^2 t^3 D}$$

Equation 1-3-38

This decay is often much faster than T_2 decay, especially in viscous liquids and strong gradients. However, the effect of self-diffusion on the magnetization can be mitigated through the use of spin echoes. Consider a simple Hahn echo experiment as described previously. During the interval $0 < t < \tau$, the magnetization will relax according to equation 1-3-38 above. At $t = \tau^-$:

$$M_{xy}(\tau^-) = M_{xy}(0)e^{-\frac{1}{3}\gamma^2 G_0^2 \tau^3 D}$$

<div align="right">Equation 1-3-39</div>

At $t = \tau$ the refocusing pulse reverses the phase of each spin. Starting from $t = \tau^+$, the magnetization continues to dephase from $M_{xy}(\tau^+)$ according to equation 1-3-38, and at $t = 2\tau$, a spin echo will occur with:

$$M_{xy}(2\tau) = M_{xy}(\tau^+)e^{-\frac{1}{3}\gamma^2 G_0^2 \tau^3 D}$$

<div align="right">Equation 1-3-40</div>

Substituting equation 1-3-39 into equation 1-3-40 yields:

$$M_{xy}(2\tau) = M_{xy}(0)e^{-\frac{2}{3}\gamma^2 G_0^2 \tau^3 D}$$

<div align="right">Equation 1-3-41</div>

Contrast this with the magnetization of a free induction decay experiment with no refocusing pulse after the same period time 2τ:

$$M_{xy}(2\tau) = M_{xy}(0)e^{-\frac{8}{3}\gamma^2 G_0^2 \tau^3 D}$$

<div align="right">Equation 1-3-42</div>

And it is seen that the contribution from self-diffusion to transverse decay is decreased by a factor of four. This suppression of diffusion effects by using spin echoes is called the Carr-Purcell mechanism [17].

If we factor spin-spin relaxation back into equation 1-3-40, then the spin echo amplitude will be:

$$M_{xy}(2\tau) = M_{xy}(0)e^{-\frac{2}{3}\gamma^2 G_0^2 \tau^3 D}e^{-2\tau/T_2}$$

<div align="right">Equation 1-3-43</div>

Substituting t for 2τ yields the function of the echo amplitude vs. time:

$$M_{xy}(t) = M_{xy}(0)e^{-\frac{1}{3}\gamma^2 G_0^2 \tau^2 Dt}e^{-t/T_2}$$

<div align="right">Equation 1-3-44</div>

Which can be rewritten as:

$$M_{xy}(t) = M_{xy}(0)e^{-t/T_{2a}}$$

<div align="right">Equation 1-3-45</div>

Where T_{2a} is the apparent transverse relaxation time constant given by [11]:

$$T_{2a} = \left(\frac{1}{3} \gamma^2 G_0^2 \tau^2 D + \frac{1}{T_2} \right)^{-1}$$

<div align="right">Equation 1-3-46</div>

We can see from equation 1-3-46 that the effective relaxation time of a population of spins is weighted by many factors, including the sample's intrinsic T_2, self diffusion coefficient D, the gradient strength G_0, and the TE (where $TE = 2\tau$) of the Hahn echo sequence. As the quantity $\frac{1}{3}\gamma^2 G_0^2 \tau^2 D$ decreases such that $\frac{1}{3}\gamma^2 G_0^2 \tau^2 D \ll \frac{1}{T_2}$, T_{2a} will approach the sample's intrinsic T_2.

In practice, it is possible to refocus the magnetization multiple times and generate multiple spin echoes in order to further suppress the effects of self diffusion and inhomogeneity on transverse relaxation. The CP and CPMG techniques are examples of such sequences wherein many spin echoes are generated from one excitation pulse. The CPMG experiment is described in more detail in chapter 3.

Spatial frequency encoding in static gradients

Since this work is directed at NMR experiments in which there is a strong static field inhomogeneity, the effects of this gradient on signal evolution must be considered. Consider a sample of nuclei with some thickness l in the $\hat{y}$ direction and is centered at $y = 0$. The sample is in the presence of a static magnetic field B_0 in the $\hat{z}$ direction with a gradient G_0 in the $\hat{y}$ direction:

$$B_0(y) = B_0(0) + G_0 y$$

<div align="right">Equation 1-3-47</div>

Now suppose we wish to apply an RF pulse that tips the entire sample into the transverse plane. All the spins must be excited at their Larmor frequency, but the sample has a distribution of Larmor frequencies in the $\hat{y}$ direction, and thus an associated bandwidth [11].

$$\Delta f = \gamma G_0 \Delta y = \gamma G_0 l \qquad \text{Equation 1-3-48}$$

To excite the entire volume, the RF pulse must have an effective tip angle of 90° over the bandwidth $\Delta f = \gamma G_0 l$. If the bandwidth of the pulse is such that Δy is less than l, then only the portion of the sample with Larmor frequencies within that bandwidth will be excited. This effect is often exploited in both NMR and MRI to selectively excite specific volumes of interest while rejecting contributions from other regions.

It is often desired for a RF pulse to have a uniform flip angle within some bandwidth and volume of interest, and a flip angle of zero everywhere else. However, practical limitations on the hardware and sequence parameters require that this condition not be perfectly met. Real pulses will have a distribution of flip angles as a function of frequency (and therefore space). As will be explored later, this can potentially cause the observed magnetization to differ from what is predicted by ideal RF pulses.

Similarly to how the application of a static gradient field allows for volume selection by controlling the bandwidth of the RF pulses, the NMR signal itself will be given spatial-frequency encoding. Consider a sample whose magnetization varies in the $\hat{y}$ direction according to some function $M_{xy}(y)$. In the presence of a static gradient G_0, also in the $\hat{y}$ direction, the magnetization from the sample at location y will precess in the rotating reference frame according to (neglecting all relaxation effects):

$$M'_{xy}(y,t) = M'_{xy}(y,0)e^{-i\gamma G_0 yt} \qquad \text{Equation 1-3-49}$$

The overall magnetization of the sample can be derived by integrating this contribution over the entire span of the sample in the $\hat{y}$ direction:

$$M'_{xy}(t) = \int M'_{xy}(y)e^{-i\gamma G_0 yt}dy \qquad \text{Equation 1-3-50}$$

The form of this equation is the Fourier transform, and thus the time-domain magnetization detected from all the spins is the Fourier transform of the spatial magnetization in the $\hat{y}$ direction [11]. This phenomenon is the basis of magnetic resonance imaging (MRI).

This work does not deal with the topic of imaging, but the effects of a gradient on the frequency content of the NMR signal are still relevant. For applications with a high G_0, the thickness l of the sample will generally be much greater than the thickness of the slice Δy selected by the RF pulses. Therefore the slice thickness of the magnetization excited by the RF pulses will be determined by the bandwidth of the RF pulses:

$$\Delta y = \Delta f \Big/ \gamma G_0 \qquad \text{Equation 1-3-51}$$

And since G_0 is constant throughout the experiment, the echo bandwidth will be equal to:

$$\Delta f = \gamma G_0 \Delta y \qquad \text{Equation 1-3-52}$$

And thus when the gradient strength and direction is constant throughout an experiment, the bandwidth of the spin echoes will tend to have the same bandwidth as the RF pulses (neglecting factors such as relaxation, flip angle inhomogeneity, etc).

1-4 NMR relaxometry

NMR relaxometry is the observation of chemical and physical properties and processes in a SUT through the measurement of apparent relaxation rates. The principle contrast mechanisms in NMR relaxometry experiments are T_1, T_2, and D. NMR relaxometry is convenient because these contrast mechanisms do not have strict requirements for the strength or spatial homogeneity of B_0 and B_1, which are often responsible for the high cost of NMR systems. In addition, relaxometry experiments do not necessarily require a gradient system. T_1 and T_2 can be observed in the absence of any gradients, while diffusion effects do require some gradient. However, for diffusion effects, the strength or direction of the gradient does not need to be controlled, and can merely be static (though control over gradients allows for more degrees of freedom in the experiment). Static gradients can easily be generated by the fringe field of any type of magnet.

The relatively simple requirements of NMR relaxometry systems make them appealing for applications where factors such as low cost and small size are important. Here we list a few example applications found in literature and industry that are be compatible with the capabilities of our relaxometry platform.

Self diffusion coefficient measurement

NMR relaxometry is by far the most common method of measuring the self diffusion coefficient of liquids. Many studies of the measurement of D using single sided NMR probes with static gradients have been published, and show good accuracy despite the simplicity of the hardware involved [7], [18]. In addition to measurements performed

on simple liquid samples, Flaum [6] and Rata et al [7] have shown the use of single-sided NMR relaxometry in studies of restricted self diffusion in porous media.

Solid state NMR material characterization

Single sided NMR relaxometry has gained acceptance as a method for investigating the structure of solid samples, especially in polymers. Single sided NMR systems are especially suited to solid state media because their strong static gradients allow for very high bandwidth operation and thus very short echo times, enabling them to resolve very fast relaxation processes seen in solids.

Various studies have demonstrated that there is a close correlation between crosslinking density in polymers and transverse relaxation time. Blümich et al and Goga have shown that such dependencies are easily detectable with single sided relaxometry [2], [10]. Their studies show the use of NMR relaxometry in detecting the degree of vulcanization in tire rubber, damage and stress in PVC piping, and the curing of polymer adhesives.

Perlo et al has also shown the use of a single sided system for one dimensional stray field imaging (STRAFI). This type of imaging technique does not rely on controllable gradients, but instead relies on displacement of the SUT in the direction of the static gradient in order to form a one dimensional profile of the SUT's NMR properties [19]. Therefore this application is suitable for our platform.

Quality control in edible products

NMR relaxometry has also found niche roles in quality control for edible products. The bakery, confectionary, and margarine industries have accepted NMR relaxometry as a standard means of measuring solid fat content in raw ingredients [4],

[20]. NMR relaxometry has also become a standard method of measuring moisture and oil content in oil-bearing crops [9]. Guthausen et al have shown the use of a NMR MOUSE for the measurement of fat content in various foods without removing them from their packaging [8]. Stork et al have demonstrated the use of a "semi-single-sided" magnet array for detecting oxygen content in commercial table water [5]. All of these applications are compatible with the capabilities of our relaxometry platform.

Throughout the course of this work, we will demonstrate that the platform is capable of performing similar experiments to those listed above. In addition, we will show that the platform has a degree of versatility and mobility not yet seen in any NMR system. We hope that this will allow for new avenues of research into mobile and wearable applications, especially for biomedical applications.

Chapter 2: Hardware design and verification

In this chapter we will discuss the role of various components of the NMR platform, and how their characteristics were specified according to the desired applications. We will also discuss the implementation of the hardware, and measurements of the performance of each component.

2-1 The Magnet

The properties of the NMR magnet define many of the capabilities and limitations of an NMR system. The strength of the magnetic field B_0 within the volume of interest (and the nuclei of interest) determines the system's Larmor frequency f_0. The equilibrium magnetization M_0 of the sample will also be proportional to B_0. The spatial profile of the field within the volume of interest also determines what experiments and applications are feasible with the magnet. Applications such as imaging (MRI) and spectroscopy typically require very homogeneous B_0, while other simple NMR experiments, such as measurement of relaxation and diffusion in bulk samples, do not.

The physical shape and size of the magnet and its B_0 will also determine its suitability for various applications. Closed magnets, in which the volume of interest is surrounded by the magnet, can generally achieve higher field strengths and more homogeneous B_0 than open/single sided magnets, where the volume of interest is completely outside of the magnet. However, closed magnets are limited to subjects that fit inside the magnet's volume, while single sided magnets may be used with objects much larger than the magnet itself.

There are three major magnet varieties that are useful for creating NMR/MRI systems. Permanent magnets generate a static field which requires no electronics, are relatively inexpensive, and can have moderate field strengths up to 1T. However, permanent magnets often suffer temperature drift and manufacturing variance, and are thus not suitable for applications requiring a stable and homogeneous B_0. Resistive electromagnets use conventional current carrying conductors to create a magnetic field. These systems can generate strong and homogeneous fields, but require large amounts of power and cooling due to the magnet's resistance. Superconducting electromagnets are the highest performing magnet type, since they can generate a very strong and homogeneous B_0 while effectively dissipating no power. However they require sophisticated cooling systems and construction to maintain a superconducting state, making superconducting magnets very expensive.

For this work, we chose to create a single sided magnet array comprised of permanent rare earth magnets. There are a wide variety of published permanent magnet designs, but all exhibit a relatively strong static gradient G_0 relative to B_0. A strong G_0 is useful for high resolution 1-D imaging (STRAFI) [7], and for diffusion measurement of high viscosity samples. However, a high G_0 results in a narrower slice thickness for a given bandwidth, and thus a smaller volume of sample that can be analyzed, and lower SNR per equivalent bandwidth. Also, measurement of T_2 is difficult in low viscosity samples due to the heavy effective weighting of self-diffusion on transverse relaxation.

Because of these factors, we chose to design a novel magnet array with a significantly lower gradient, while still maintaining acceptable B_0, homogeneity, weight, and penetration depth. A simple cross sectional diagram of the magnet array is shown

below. B_0 is primarily in the $\hat{z}$ direction, while G_0 is in the y direction. The length of the magnets (in the $\hat{x}$ direction) is two inches. We initially targeted a penetration depth of y=7 mm from the magnet surface, on the basis that it would be deep enough for in-vivo biosensor applications, while providing an adequate compromise in sensitivity.
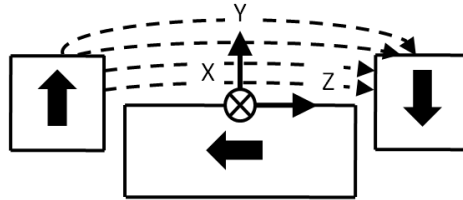
Figure 2-1-1) Schematic cross sectional diagram of our custom single sided magnet array, showing the coordinate system used. Black arrows indicate the polarization of the permanent magnets, and dashed lines show the static field B_0.

The magnetic field of the magnet array was simulated with Finite Element Method Magnetics (FEMM) 4.2, a simple free 2D Finite Element Method program [21]. At a distance of 7 mm from the top surface of the center magnet, the field strength at z=0 and x=0 was predicted to be 235.9 mT, and the gradient in the y direction was 7.01 T/m (averaged between y=6 mm and y=8 mm).
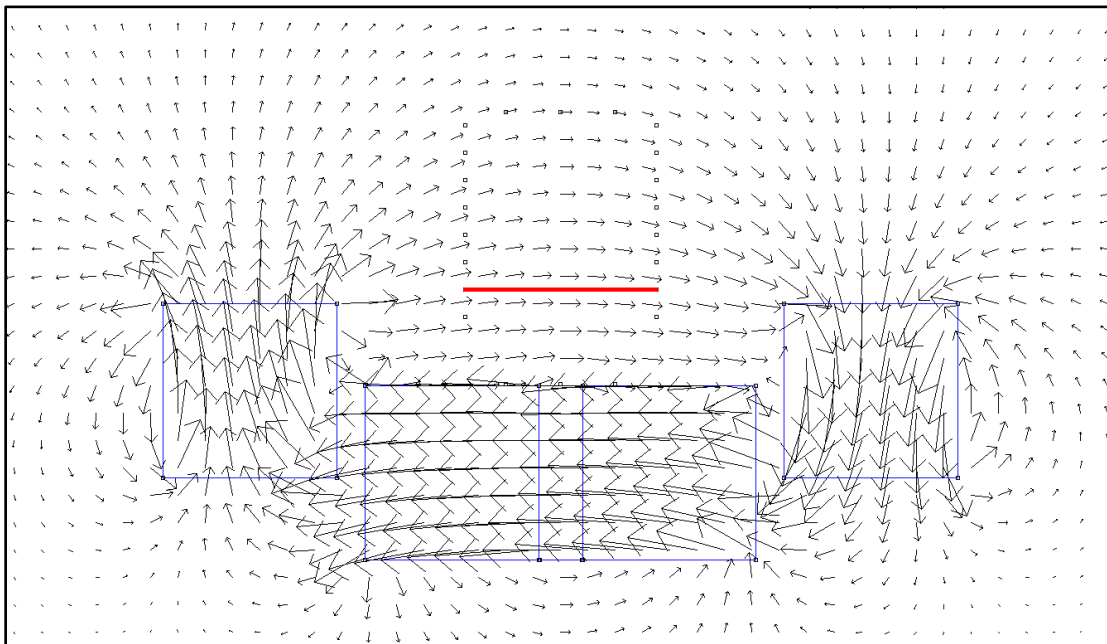
Figure 2-1-2) Simulated vector plot of our custom surface magnet array. The red line shows the intended sensitive volume at y=7 mm.
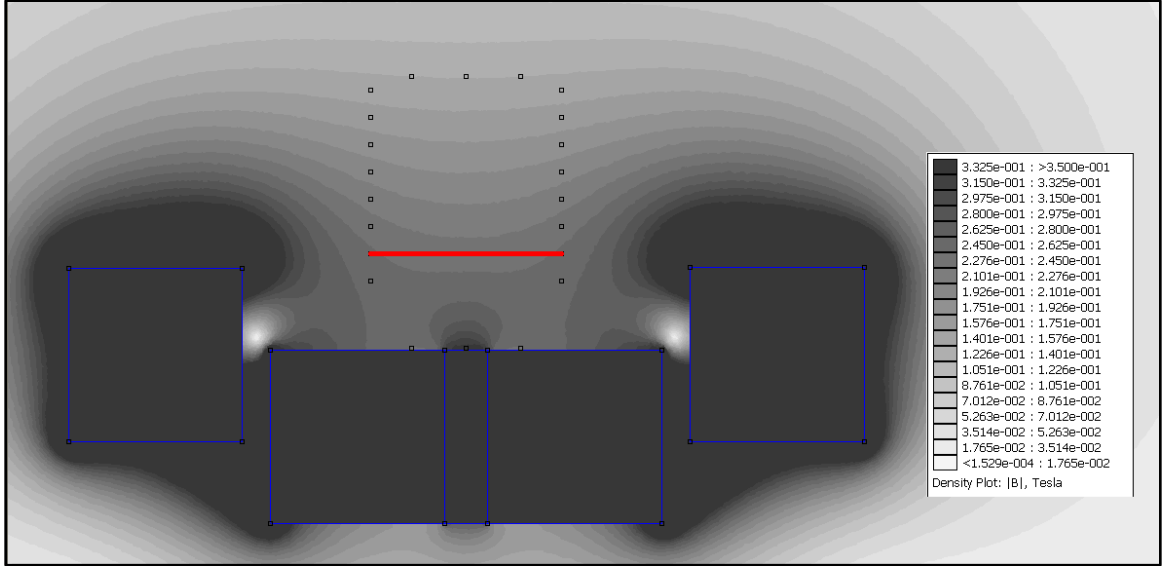
Figure 2-1-3) Simulated field density plot of our custom surface magnet array. The red line shows the intended sensitive volume at y=7 mm.

The magnet was constructed using permanent magnets obtained from Applied Magnets. The harness for the array was fabricated using a Projet SD 3000 3D printer from 3D Systems Corporation. The array measures 70x64x24 mm and weighs approximately 0.6 lbs without a coil mounted. After construction, the B_z of the array at y=7 mm was roughly measured using a DTM-151 Teslameter from GMW Associates. The measured B_0 at this depth was approximately 196.1 mT, corresponding to a f_0=8.35 MHz for protons. Based on this measurement, all subsequent experiments were performed at 8.35 MHz.

An apparatus for mapping B_z in the $\hat{y}$ direction was constructed, allowing for accurate and repeatable measurements of both B_0 and G_0 as a function of y. The Teslameter probe was sensitive in the $\hat{z}$ direction, and measurements of B_z and the actual y were taken along the y-axis from y=3.4 mm to y=12.9 mm in steps of 0.5 mm. This measurement was repeated in four passes. The four passes were averaged together to give the data shown in figure 2-1-4 below:
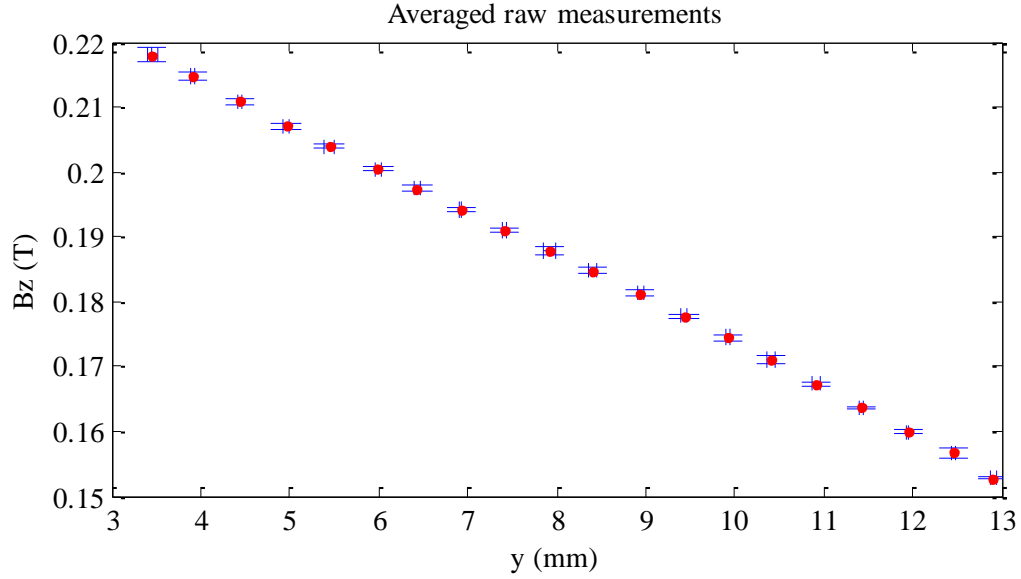
Figure 2-1-4) Field measurements of the custom surface magnet vs. y. The y and B_z values of four passes were averaged together.

Though this curve appears very linear, its gradient varied significantly, and thus we wanted to determine the spatial profile of G_0. To determine the gradient at a given y, the measurements within a small given window Δy were applied to a linear fit, and the slope of this line was taken as the gradient, while the value of the line at y was taken as the true value of B_z at y. The results are shown below for $\Delta y = 6$ mm:
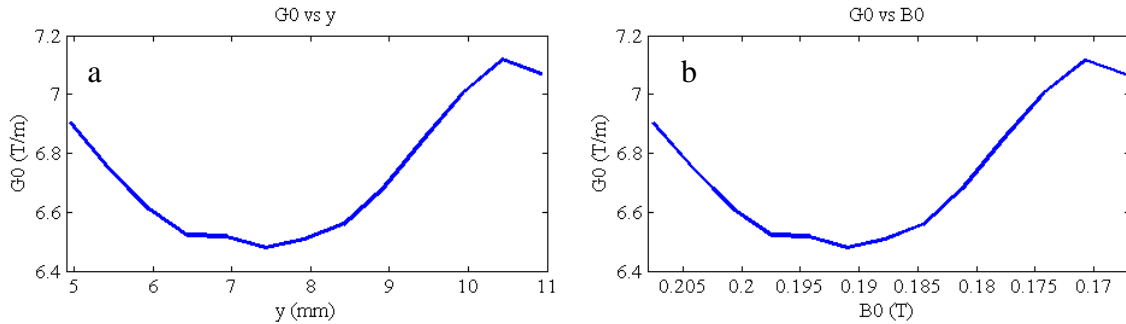
Figure 2-1-5 a) Fit G_0 vs. y using fitting window of 6mm b) Fit G_0 vs. B_0 using fitting window of 6 mm.

These detailed measurements showed that our chosen frequency of 8.35 MHz actually was located at y=6.65 mm, and the G_0 at this field strength was 6.52 T/m. The difference in these measurements and the simulated results was mostly due to the fact that the real magnet is of finite length, while FEMM assumes infinite length in the $\hat{x}$ direction.

26

Variation in the individual magnets' strength and errors in the harness's dimensions also contribute to this disagreement.

Despite the lower than expected field strength, the magnet's G_0/B_0 ratio was significantly lower than other single sided arrays of comparable weight and size, making it suitable for mobile relaxometry experiments with good penetration depth.

2-2 The RF Coil

The purpose of the RF coils in an NMR system is to both manipulate and sense the magnetization of the sample. An NMR system may contain separate sets of coils for B_1 transmission and signal reception, and often each is comprised of multiple coils in an array. A single transmit/receive (TR) coil may also be used.

Coils are characterized by their ability to sense and transmit B fields with high sensitivity and low losses and noise. One important coil parameter is B_1 efficiency (specified in Tesla per amp or Tesla per $\sqrt{W}$), which describes the relationship between the current or power delivered to the coil with the B_1 field it transmits or receives at a certain location in space relative to the coil. Another specification of a coil is the quality factor Q, which describes the ratio between the reactive and resistive impedance of the coil at its operating frequency.

$$Q = \left| X \middle/ R \right|$$ Equation 2-2-1

For a transmitting coil, the power P required to generate a certain B_1 will be inversely proportional to its Q [12]:

$$B_1 \propto P \middle/ Q$$ Equation 2-2-2

For a receiving coil, the SNR of the received signal will be proportional to the square root of Q (assuming the bandwidth of the received signal is less than the bandwidth of the coil) [12]:

$$SNR \propto \sqrt{Q}$$
<div align="right">Equation 2-2-3</div>

Also, the bandwidth of an impedance matched coil (assuming a simple matching network tuned to one frequency) will be inversely proportional to Q:

$$BW \propto \frac{1}{Q}$$
<div align="right">Equation 2-2-4</div>

While high Q is usually desirable, it may sometimes be necessary to decrease Q for applications that require a wide bandwidth.

The physical shape and size of a RF coil will determine its electrical properties, as well as which applications it is suited for. There are a vast variety of coil geometries in use for NMR, but the scope of this work will confine itself to simple coil geometries suitable for small systems. Volume coils, such as solenoid coils, can have relatively high Q. Because the sample is inside the coil itself, it will also have a high B_1 efficiency and good homogeneity. While the high Q and B_1 efficiency of volume coils often results in good SNR, they are not suitable for applications where the dimensions of the coil are restricted, or where the sample is much larger than the volume of interest. In such applications, flat surface coils are often necessary. While surface coils generally have lower Q than volume coils, their ability to excite specific volumes of interest in large samples will often give better overall B_1 efficiency and SNR, especially with shallow penetration depths. However, surface coils usually suffer from poorer B_1 homogeneity than volume coils.

For surface sensor applications, the space allocated to the RF coils is severely limited since the coils must occupy a space between the magnet surface and the sample. Since the thickness of the coils effectively decreases the penetration depth of the overall sensor, it was desirable to construct these coils to be as thin as possible. For this reason we chose to use single T/R surface coils for single sided applications.

The RF surface coils used in this work were made from double sided or 4-layer copper clad printed circuit board, which can be etched or milled for excellent precision and repeatability. All measurements of the TR coils were performed using a E5061A vector network analyzer (VNA) from Agilent.
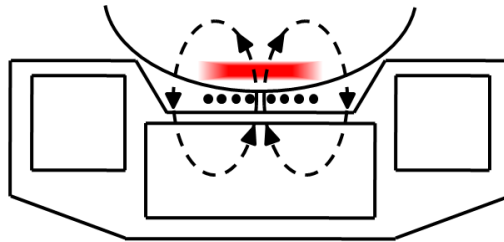
Figure 2-2-1) Cross sectional diagram of the magnet and harness with a flat surface coil. Black dots show the location of coil conductors, and dashed lines show an example B_1 field. The SUT is much larger than the probe itself, but only a small slice of it (shaded red) is excited by the coil.
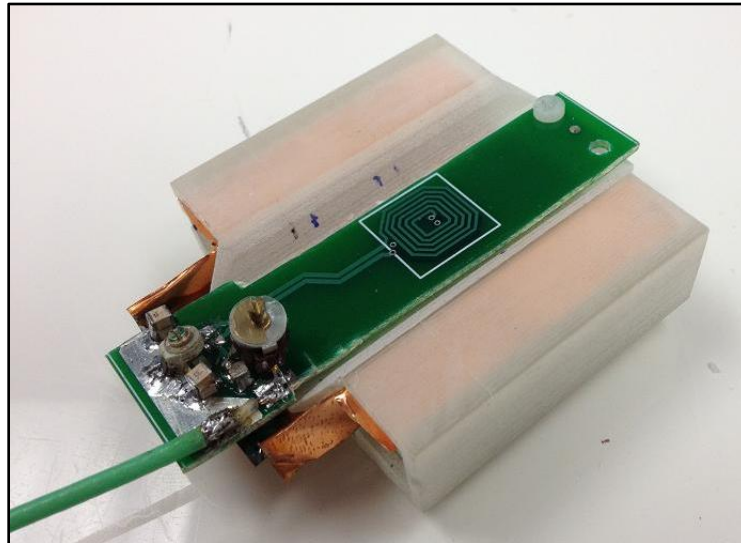
Figure 2-2-2) Photo of the surface magnet fitted with the spiral surface coil. The 50 Ω matching network is local to the coil, allowing it to be connected with common 50 Ω coaxial cable.

Coil impedance at 8.35 MHz (measured with VNA)	Z=3.877+j155.1 Ω
Coil outer radius	7.15 mm
Coil inner radius	4.2 mm
Coil thickness	1.7 mm
Number of turns	N=20 of 1oz copper
Calculated B_1 efficiency (simulated with FEMM)	1.4 mT/A

Table 2-2-1) Properties of the spiral surface coil in figure 2-2-2. These properties are measured and simulated with the coil mounted on the magnet, with 1.7 mm of spacing between the magnet harness and the bottom of the coil. This is the configuration used for the measurement of drying adhesives in section 4-6.

We also used a simple solenoid volume coil with small liquid samples that did not require a surface sensor. The solenoid coil's higher Q and B_1 efficiency yielded a higher SNR, and required less power for RF pulses.
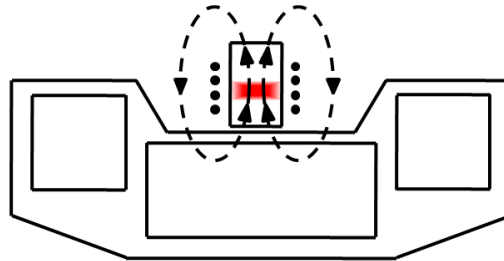
Figure 2-2-3) Cross sectional diagram of the magnet and harness with solenoid volume coil. Black dots show the location of coil conductors, and dashed lines show an example B_1 field. The SUT fits inside the coil, and only a small slice of it (shaded red) is excited.
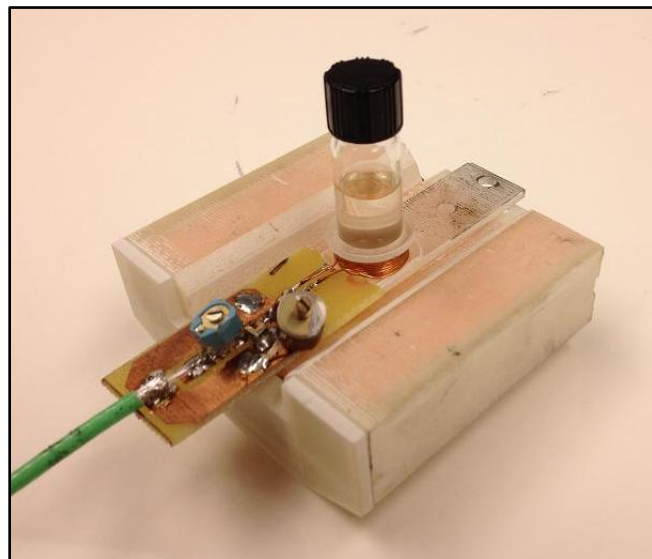
Figure 2-2-4) Photo of the surface magnet fitted with the solenoid volume coil. The coil was designed to hold small glass vials for the SUT. A SUT of canola oil is shown in the coil.

Coil impedance at 8.35 MHz (measured with VNA)	Z=0.95+j90.8 Ω
Coil radius	6.7 mm
Inner radius of sample holder	5.2 mm
Cross sectional area of vial volume	77.8 mm^2
Coil height	4 mm
Number of turns	N=11 of 28AWG wire
Calculated B_1 efficiency [12]	988 µT/A

Table 2-2-2) Properties of the solenoid volume coil in figure 2-2-4. These properties are measured and calculated with the coil mounted on the magnet such that the center of the coil lies 5.5 mm from the surface of the harness (y=7 mm). This is the configuration used for all experiments of liquid samples.

Coil integration and matching

For our platform, we desired the coil and magnet to not be directly integrated into the platform hardware (as opposed to many spectroscopy systems that integrate the magnet, coils, and other electronics in one enclosure). Thus the magnet and coils were designed as separate components that can be combined at will, effectively making a standalone NMR probe. A 50 Ω coil impedance matching network [22] was integrated into the probe assembly so that it could be connected to with a simple 50 Ω coaxial cable. The platform was also given a 50 Ω coil port (see section 2-3), allowing us to easily switch between multiple probes, and also allowing the probe to be moved and positioned independently of the platform hardware.

Magnet shielding and dead time

While a coil's operation may be predictable when operating in free space, it suffers from some non-ideal behavior when placed inside the magnet's B_0. The magnets themselves are conductive, and thus the magnetic and electric fields from the RF coil will induce currents in the magnets. These currents will result in additional Ohmic losses, lowering the overall Q and B_1 efficiency of the coil.

The strong RF fields and currents which occur during transmit pulses also give rise to electromechanical disturbances in the system. All currents in the coil and magnet

will produce Lorentz forces, causing vibration and "ringing" in both the coil and the magnet itself, called magnetoacoustic ringing. Such motion can cause disturbances in B_0, and create interference in the received signal. These effects may persist for significant periods of time (hundreds of microseconds) even after the end of a transmit pulse [23]. Though this usually has no noticeable impact on the coil's measured electrical characteristics, it can be problematic in experiments that require fast recovery of the detected signal after transmit pulses.

To address the problems caused by magnetoacoustic ringing, we put thin copper sheets on the inner surface of the magnet, as suggested previously by Anferova et al [22]. The eddy currents caused by the RF coil circulate almost entirely in the copper sheets, rather than the magnet, which shields the magnet from the magnetic and electric fields from the coil. The copper may still vibrate due to Lorentz forces, but the vibration in the magnets is greatly reduced, resulting in less disturbance to B_0.

The construction of the RF coil also has significant impacts on its dead time. In agreement with these previous publications [22], [23], we observed that surface coils made from etched PCBs had much less ringing than solenoid coils made from wound magnet wire. This was likely due to the conductors in etched coils being much more rigidly fixed than the windings of wound coils. Also being shorter in the direction of G_0 meant that surface coils were subject to less net force between the top and bottom of the coil, thus reducing the net force between the coil windings.

By applying the copper shield to the surface magnet and using an etched surface coil, we were able to reduce the dead time of the system to under 25 µs. We define the dead time measurement by the amount of time after the end of the transmit pulse that the

disturbances in the baseband signal drop below the noise floor. Figure 2-2-5 shows the

benefit of magnet shielding in reducing artifacts due to magnetoacoustic ringing.
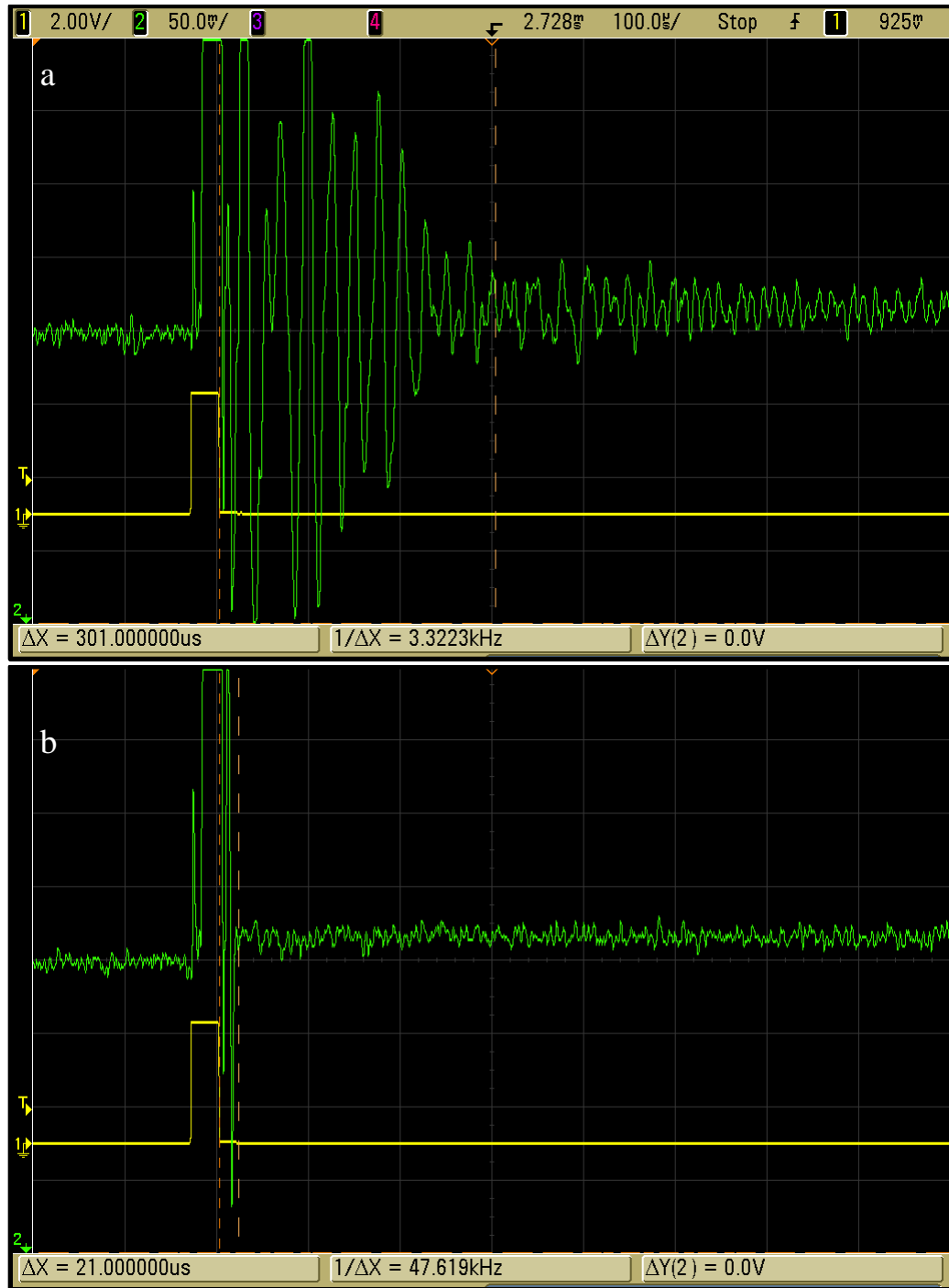
Figure 2-2-5) Oscilloscope captures of the TXSW signal (channel 1, yellow) and the in-phase baseband signal (channel 2, green) after a RF pulse. Acquired when using a solenoid volume coil. a) Without copper shielding on the magnets, very large magnetoacoustic ringing is observed, and persists above the noise floor for nearly a millisecond. b) After adding copper shielding, magnetoacoustic ringing is damped below the noise floor within 21 µs after the end of the RF pulse. Data is captured with trace averaging (N=16).

Probe shielding

Due to the low signal powers typical of single sided NMR experiments, the NMR probe (comprised of the magnet and RF coil) is very susceptible to interference from external fields. Special care must be taken to ensure that such interference does not contaminate the NMR signal. For this reason, we perform most of our experiments with the probe inside a shielded enclosure. The 50 Ω cable from the coil is passed through the enclosure with a BNC feedthrough, and connects to the platform hardware via BNC coaxial cable.

In some experiments in which mobility is required, or when the object to be scanned does not fit in the enclosure, this shielding method is not acceptable. Therefore we also created a modified probe designed specifically for use without a shielded enclosure. The RF coil was implemented as a butterfly surface coil consisting of two adjacent spiral coils wound in opposite direction, and connected in series. When perturbed with an external B field, each half of the butterfly coil will contribute an equal and opposite EMF, and thus such external fields induce no overall signal in the coil (assuming the field is uniform over the entire coil). Magnetization that is local to either spiral, on the other hand, will cause an unbalanced EMF. This allows butterfly coils to reject ambient magnetic fields while still being sensitive to local magnetization.

Additionally, the coil is fitted with a grounded screen, which is fabricated by etching a single sided PCB (thickness of 1.62 mm). This screen forces all external field lines to terminate at circuit ground, rather than on the coil itself. The screen is slotted in order to inhibit eddy currents in its surface that would also shield the B field and reduce the coil's B_1 efficiency. An added benefit of the screen is that it significantly reduces the

coupling of the coil to the sample via conservative E fields, which reduces the effect of sample loading on the coil [22].
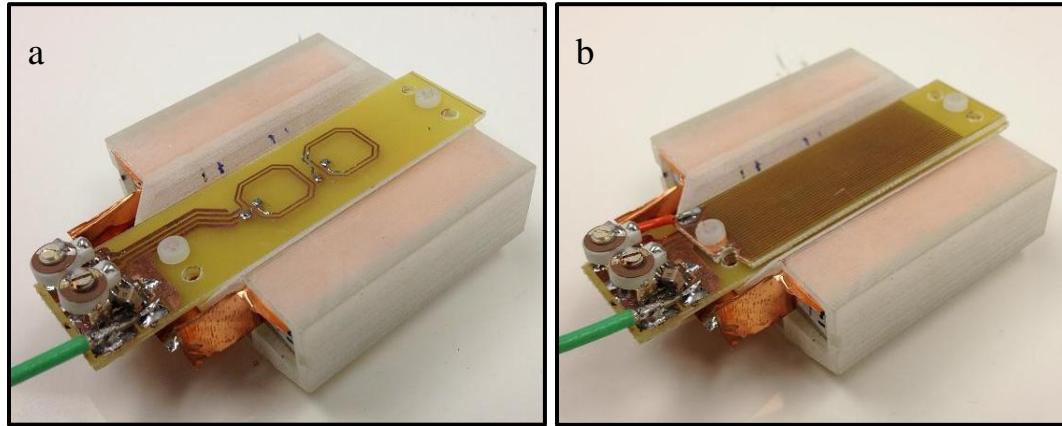
Figure 2-2-6) Photos of the NMR surface probe. a) The probe uses a butterfly surface coil to null out external B fields. b) External E fields are shielded with the addition of a slotted screen on top of the coil.

These measures do incur a penalty to the sensitivity of the probe, as well as decreasing the overall penetration depth. However, the loss in sensitivity is more than compensated for by the immunity to interference (which would otherwise be many times the thermal noise floor of the system).

2-3 Transmit Receive Switch (TRSW)

Systems using only one coil for transmit and receive require a transmit/receive switch (TRSW) in order to change whether the coil is coupled to the transmit power amplifier during the transmit phase or the RF receive chain during the receive phase. A TR switch has three ports: TX, RX, and Coil. When transmitting, the TX and Coil ports will be coupled together, and isolated from RX. When receiving, the RX and Coil ports will be coupled together, and isolated from TX.

The performance of a TR switch is judged based on the isolation and attenuation between the ports in both states of operation. Attenuation between TX and Coil during

the transmit state should be low in order to not severely impact the overall efficiency of the TPA. Attenuation between Coil and RX during the receive state must be low in order to not severely degrade the overall SNR of the system. Isolation between Coil and RX during the transmit state must be enough so that the receive chain is not damaged by power leaking through. Isolation between TX and RX during the receive state must be high in order to prevent significant DC artifacts at baseband.

We utilized a broadband TRSW design using MA4P7470F-1072T PIN diodes [24] from M/A-COM Technology Solutions. The TRSW is composed of two single-pole single-throw (SPST) switches, each of which can be controlled independently. Each PIN diode is biased with a negative voltage V_r while in the off state, and is forward biased with 105 mA of current in the on state. Each of the SPST switches is controlled by its own logic input signal, called TXSW and RXSW.
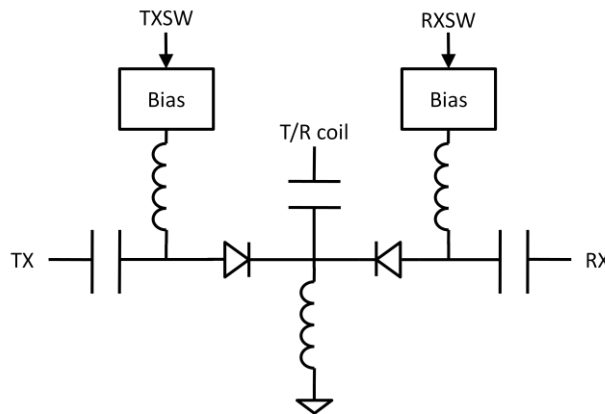
Figure 2-3-1) Simplified diagram of the TRSW. Each bias block provides a 105 mA forward bias current to its PIN diode when on, and a -V_r reverse bias voltage when off

We measured the small signal performance of the TRSW using the VNA. All measurements were performed with an incident power level of 10 dBm, with Vr=-13.5 V. Of primary importance is the isolation provided between the TX and RX ports, due to the

risk of damage to the RF receive chain during RF pulses. The isolation of the TRSW is shown in figures 2-3-2 and 2-3-3.

TX to Coil isolation
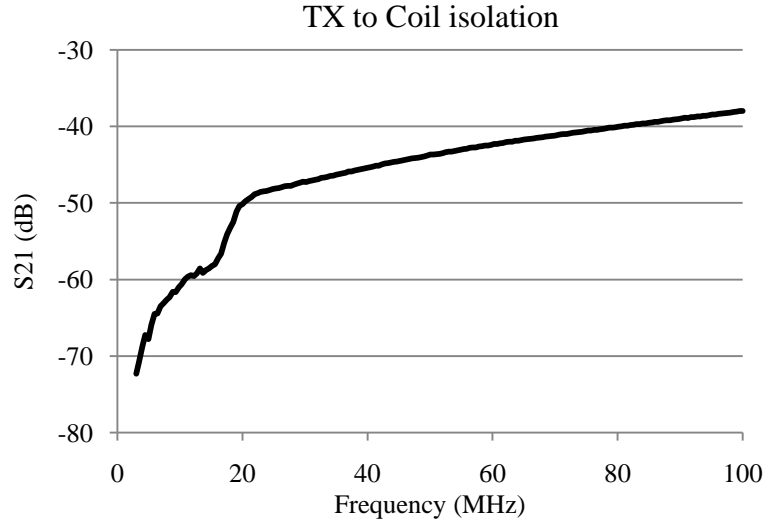
Figure 2-3-2) Isolation between TX and RX ports when RXSW is on and TXSW is off

TX to RX isolation
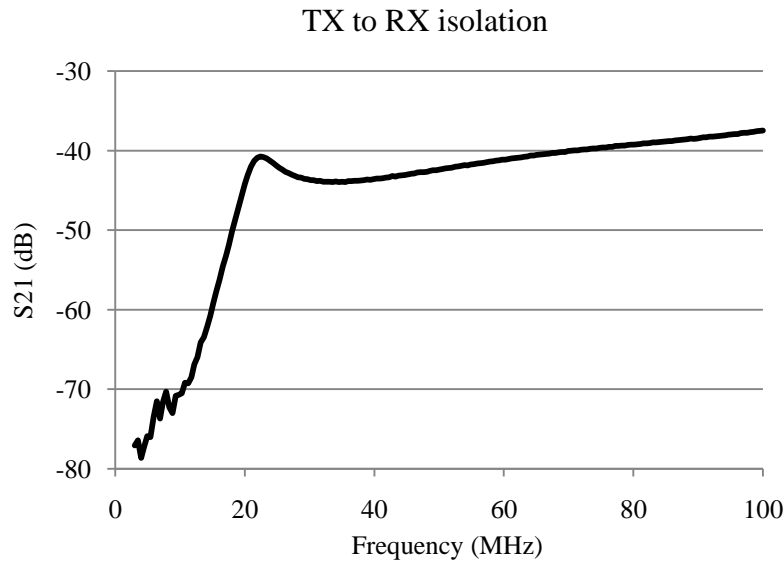
Figure 2-3-3) Isolation between TX and RX ports when RXSW is off and TXSW is on

The Isolation between the TX and RX ports was always less than -35 dB, suggesting that the RF receive amplifier chain will not be damaged by RF pulses up to 55 dBm, or 316 W (see section 2-4). However, PIN diode switches cannot be linearly approximated under all conditions, especially in the reverse biased state. If the peak RF voltage applied to a reverse biased PIN diode causes a positive bias voltage across the

diode at any time, it will cause carrier generation inside the PIN diode. Depending on the magnitude and frequency of this positive bias, the pin diode's intrinsic region may begin to conduct, causing the switch's isolation to degrade. We therefore apply methodology proposed by [25] to determine the relationship between the safe operating area (SOA) of the TRSW and the reverse bias voltage V_r. Figure 2-3-4 shows the maximum RF power allowed by this methodology as a function of frequency, and for two different values of V_r.
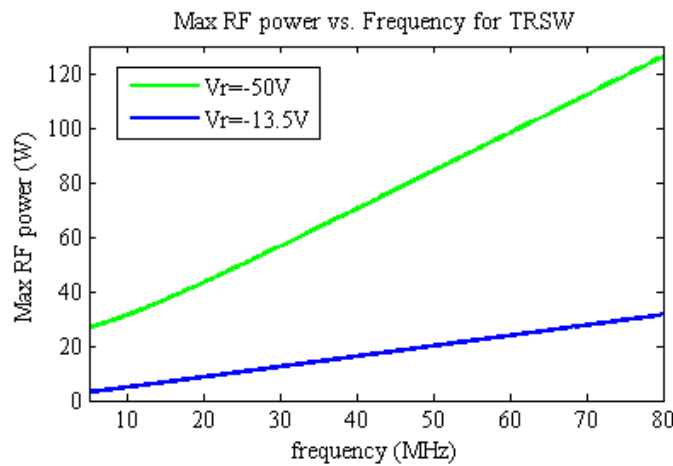
Figure 2-3-4) Maximum permissible RF power isolated by the TRSW for two example reverse bias voltages. Duty cycle is assumed to be 10%.

We can see that at low frequencies, the maximum power we can safely isolate with the TRSW is limited by V_r, especially at low RF frequencies, where V_r must be approximately equal to the peak RF voltage. For example, at a RF frequency of 8.35 MHz and a V_r of -13.5 V, we are limited to a peak RF voltage of 20.5V, or a RF power of 4.23 W. This is enough for many experiments, such as those done with our solenoid volume coil, but will be insufficient for most surface coil applications. For such experiments, we may use a V_r up to -60 V, which allows much higher RF power levels (though the operation of the TRSW with larger V_r will result in additional artifacts due to RF chain recovery). The generation of V_r is discussed in greater detail in section 2-8.

Also of interest is the attenuation between the TX and Coil ports during pulse transmission, and the attenuation between the Coil and RX ports during reception.

TX to Coil attenuation
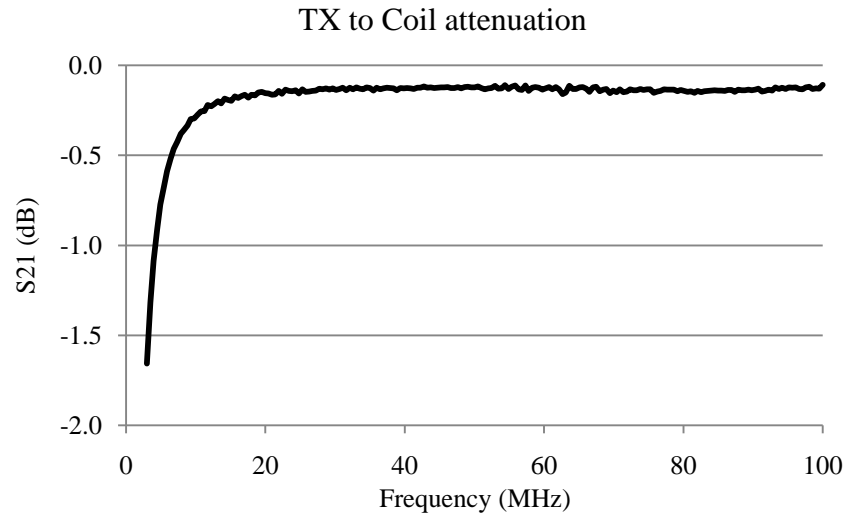
Figure 2-3-5) Attenuation from TX to Coil port when TXSW is on, RXSW is off

Coil to RX attenuation
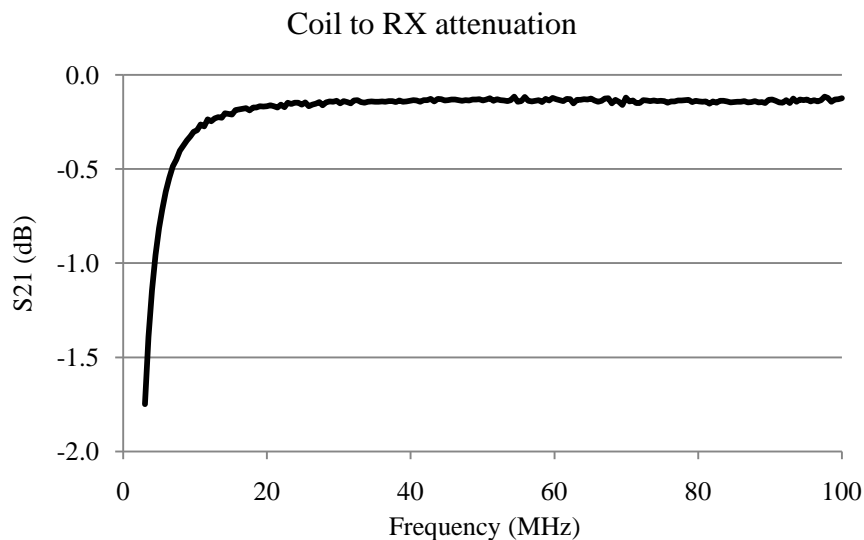
Figure 2-3-6) Attenuation from Coil to RX port when TXSW is off, RXSW is on

It can be seen that the TRSW has a useable bandwidth extending across the entire measured range (3-100 MHz). However it should be noted that the increase in attenuation between Coil and RX at frequencies below 10 MHz will have a significant impact on the system's noise figure (see section 2-6 below).

2-4 Transmit Power Amplifier (TPA)

In order to generate the high B_1 necessary for NMR experiments, a RF transmit power amplifier (TPA) is required. The properties of the TPA, including gain, peak power, average power, dynamic range, and bandwidth, are dictated by the specific sequences required, and the RF coil's B_1 efficiency and Q. The TPA often allows for amplitude modulation of the pulse envelope, yielding many different pulse shapes. The scope of this work deals only with rectangular RF pulses that are only modulated by their duration, peak amplitude, and phase.

The specifications for the TPA are determined mainly by the desired sequence, and the RF coil. Therefore we suggest a hypothetical sequence/coil combination that puts a high demand on the TPA performance. These parameters are based on the spiral surface coil presented in section 2-2 (see table 2-2-1):

f_0	8.35 MHz
Maximum flip angle	180°
Bandwidth of maximum flip angle pulse	200 KHz
Average Transmit duty cycle	10%
B_1 efficiency	1.4 mT/A
Coil ESR	3.877 Ω

Table 2-4-1) Experiment parameters for hypothetical TPA output power.

A rectangular transmit pulse with BW=200 KHz, given by the -3 dB cutoff of the pulse's frequency spectrum, will be approximately 5 μs in duration. To achieve a 180° flip angle in 5 μs requires a ω_1 of 6.28×10^5 rad/s. Because this coil generates a linearly polarized, as opposed to circularly polarized B field, the required B_1 amplitude is 4.7 mT. The pulse will require 3.36 amps peak (2.374 A rms), which gives a power of 21.85 W in the coil (assuming a lossless matching network). The peak power required is 23.82 W after factoring the loss of the TRSW. The average power will thus be 2.382 W at the specified duty cycle.

There are various classes of RF power amplifiers with varying capabilities. Linear power amplifier classes such as A, B, and C offer simplicity, and the ability to modulate the output amplitude by varying the input amplitude. They can also be designed to have wide operating bandwidths. However the linear class amplifiers are inherently inefficient (generally less than 60%), and a tradeoff between linearity, bandwidth, and efficiency is necessary [26].

For applications requiring higher power, such as the one specified above, linear amplifiers are not attractive for small or mobile systems because of their low efficiency. Switching amplifier topologies, such as classes D, E, and F, boast efficiencies higher than linear classes [26]. However they must be tuned to a specific frequency range in order to operate efficiently. Also, they cannot be amplitude modulated by their RF input amplitude (a method called low level modulation). For these amplifier classes, amplitude modulation requires modulating the amplifier's supply voltage (a method called high level modulation), which requires additional circuitry to implement.

For our surface magnet application we chose to construct a TPA based on the Current Mode Class D (CMCD) topology [27]. While silicon-based devices are well established for small, mobile linear amplifiers, they have limited efficiencies for very high frequency switching. For this project, we have adopted gallium-nitride (GaN) FETs, an emerging transistor technology originally intended for use in switch mode power supplies [28]. GaN FETs have a heterojunction structure which yields higher electron mobility than doped silicon. This allows devices to have a low R_{DSon} while maintaining a very small geometry and fast switching speeds, making them excellent candidates in any high frequency power switching application. We chose to utilize EPC1005 GaN FETs

from EPC as the switching transistors in our CMCD. The FETs are driven by a LM5113 gate driver IC. The RF input from the control board is fed to a LT1713 comparator with complementary outputs, which provide the logic signals for the LM5113. The TPA can be deactivated by controlling the logic signal TPAEN, which forces both FETs into an OFF state. The output of the CMCD is fed to a 1:2 transformer balun that boosts the output voltage and provides isolation of common mode currents to the TRSW. A simplified diagram of the CMCD TPA is shown below:
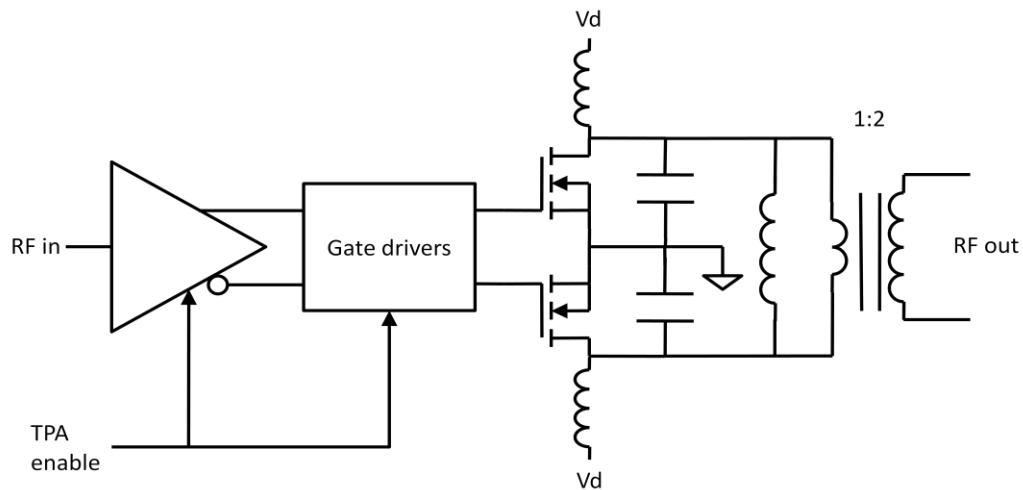
Figure 2-4-1) Simplified schematic of the CMCD TPA

The CMCD topology boasts high efficiency due to the fact that it achieves zero-voltage-switching (ZVS) on its drains. The parasitic drain to source capacitance (C_{DS}) of each FET is absorbed into the resonant tank on the output, and therefore does not contribute to switching losses [27]. Figure 2-4-2 below shows the drain waveforms on each FET, as well as the total output voltage. All data is collected with the TPA loaded by a broadband 50 Ω, -38.5 dB attenuator.
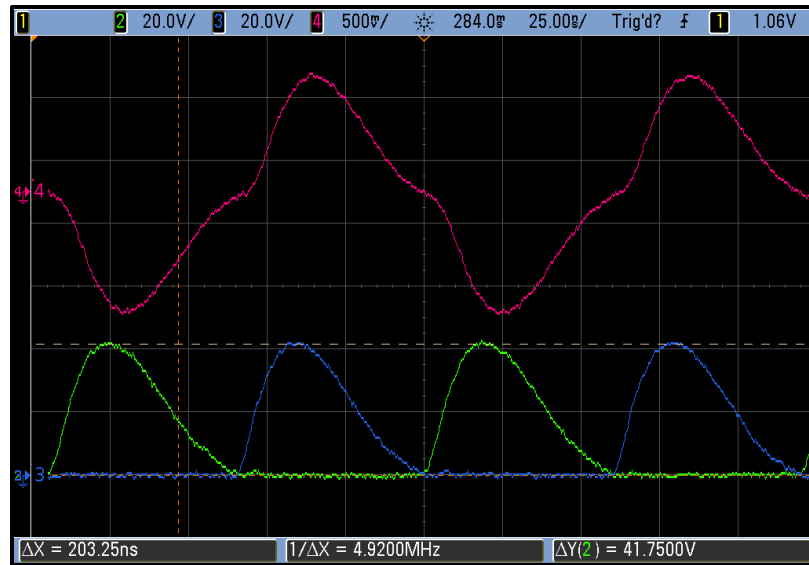
Figure 2-4-2) Oscilloscope capture of the 8.35 MHz CMCD TPA waveforms. CH2 and CH3 (green and blue, respectively) are the drain voltages of each GaN FET. CH4 (magenta) is the output, after -38.5 dB of attenuation. These waveforms were recorded at full power (V_D=12V).

Figure 2-4-3 below shows the spectral content of the RF output at full power, measured using a CXA series N9000A signal analyzer (SA) from Agilent. The output contains significant odd harmonics, while even harmonics are suppressed due to the push-pull operation of the CMCD. Approximately 3.8% of the total output power is lost in these harmonics.
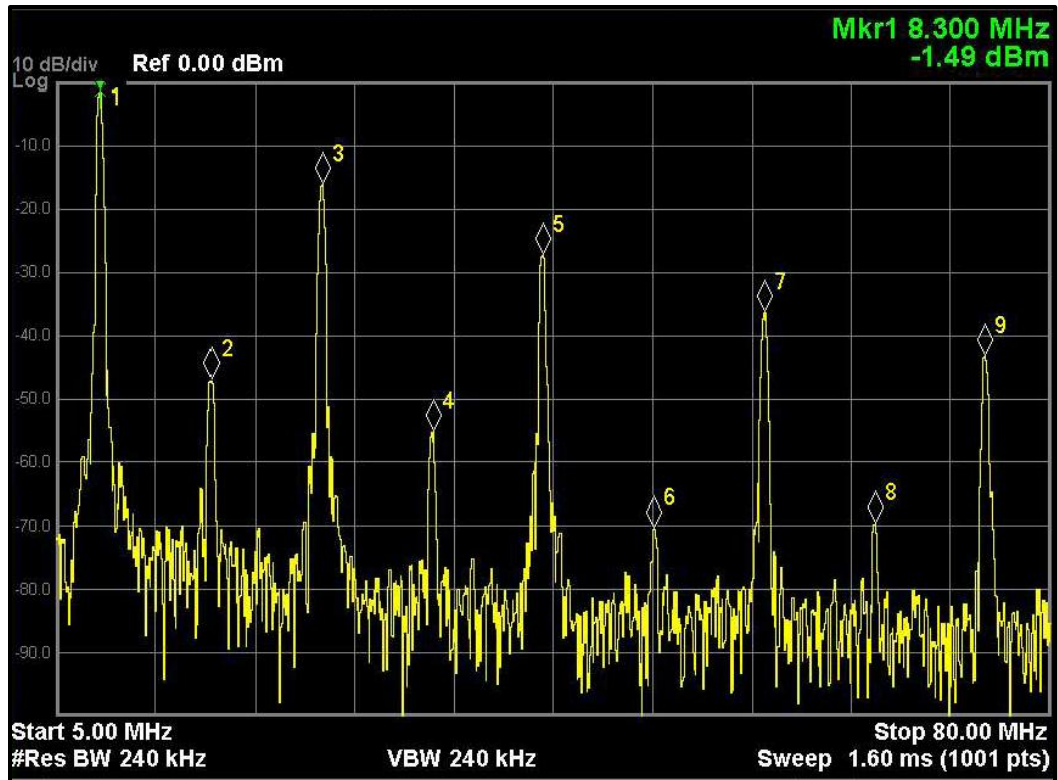
Figure 2-4-3) Spectral content of the 8.35MHz TPA output at full power (V_D=12 V), with -48.5 dB of attenuation. As shown, strong odd harmonics are present, while even harmonics are suppressed.

The efficiency of the TPA was measured by viewing the output power of the fundamental frequency on the signal analyzer. The RF output was attenuated by -48.00 dB before being fed to the signal analyzer input. The DC supply current, DC supply voltage, and fundamental power were measured simultaneously during a 150 ms pulse to calculate power draw and power output, and thus efficiency. These measurements of power consumption include only power drawn from the TPA output stage (drain power), and do not include power for the control circuitry or the RF input. The power drawn by the control circuitry at 8.35 MHz was separately measured to be 0.14 A at 12 V (independent of output power level), while the RF input power was 0 dBm. This additional information can be used to calculate the overall power added efficiency (PAE) of the TPA.

44
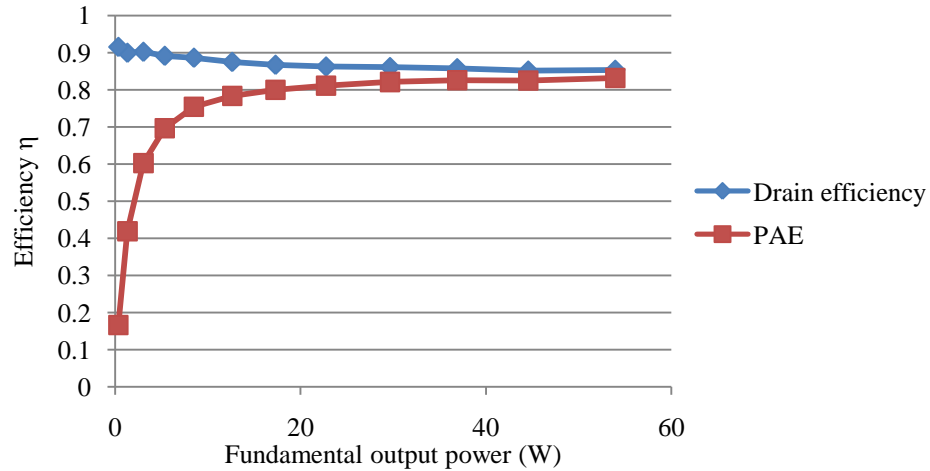
Figure 2-4-4) Plots of drain efficiency and power added efficiency (PAE) vs. fundamental output power.

The measured output power can also be used to calculate the RMS amplitude of the fundamental component of the TPA output. The following plot shows the output amplitude of the TPA vs. V_D. There is some loss of linearity at $V_D<4$ V due to the severe nonlinearity of C_{DS} in the FETs.
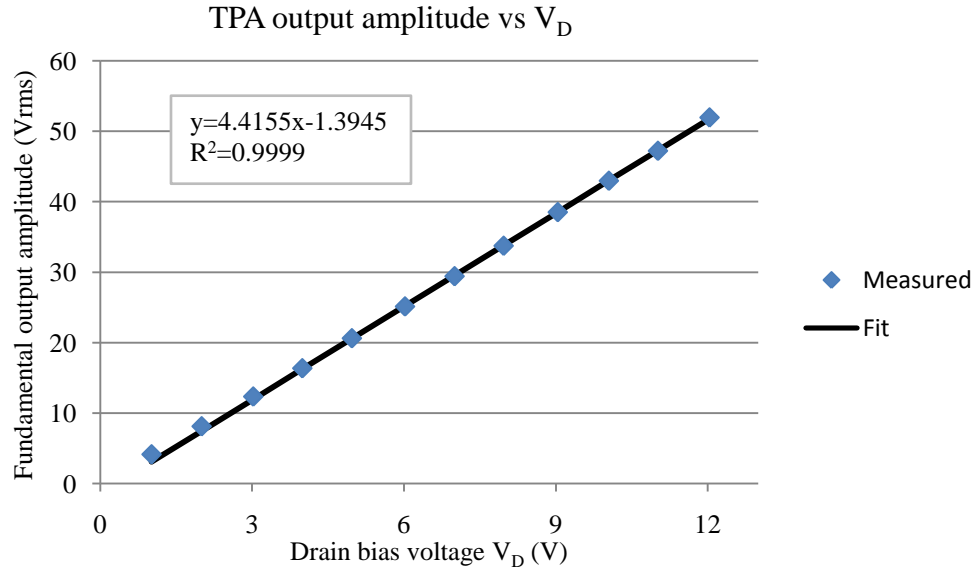
Figure 2-4-5) Plot of TPA output amplitude vs. V_D. This amplitude is calculated from the power of the fundamental signal. The displayed fit and R^2 is derived from measured data with V_D between 4 V and 12 V. The fit is extrapolated to $V_D<4$ to show the deviation of the measured data in that range.

45

2-5 Buck modulator

For controlling the amplitude of the RF pulses, we devised a buck converter that converts the 12-18 V system supply into a variable 0-12 VDC bias voltage for the TPA. The buck modulator regulates a constant DC bias V_D to the TPA during each RF pulse, but changes the V_D bias in between RF pulses in order to allow each pulse to have different amplitudes. The buck modulator is not intended to change the shape of the envelope for RF pulses (other than its overall amplitude).

Because the time between RF pulses can be as little as 30 μs in some experiments, and because the TPA demands short pulses of high power, it was desirable for the buck modulator to have a high closed loop bandwidth in order to accurately control the RF pulse amplitudes. For this reason we utilized a high frequency voltage-mode buck converter based similar to that demonstrated in [27]. Like the TPA, we also base this buck converter on GaN FETs from EPC. The converter operates at a switching frequency of 1.54 MHz, and has an open loop crossover frequency of 300 KHz with a phase margin of 55 degrees.
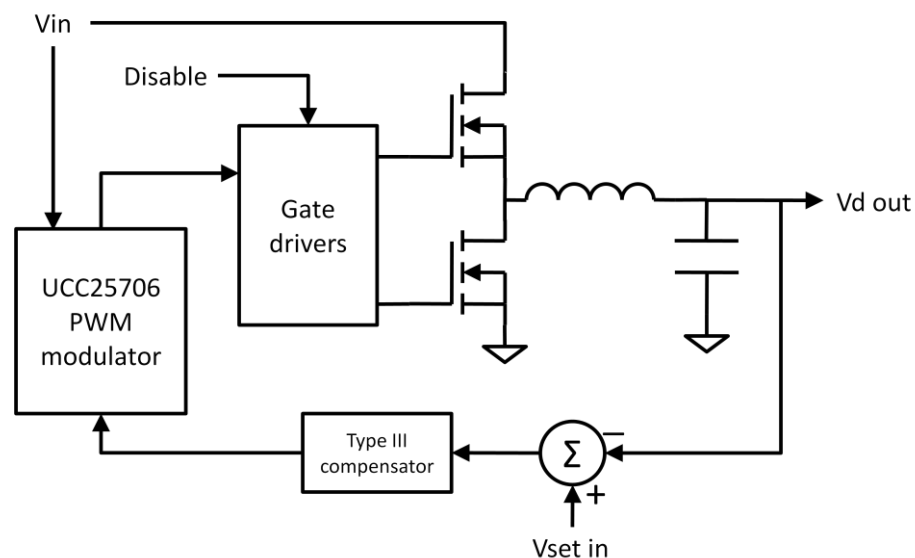
Figure 2-5-1) Simplified schematic of the buck modulator

Unlike the modulator in [27], our buck modulator did not use RF current feedback from the TPA, but rather output voltage feedback from V_D. V_D is controlled by a control voltage Vset, as shown in figure 2-5-1. The following figures show the transient response of the buck modulator in response to a step input on its set point. For small signal conditions, the converter has a rise/fall time of 3.1 µs, and a settling time of 11 µs.
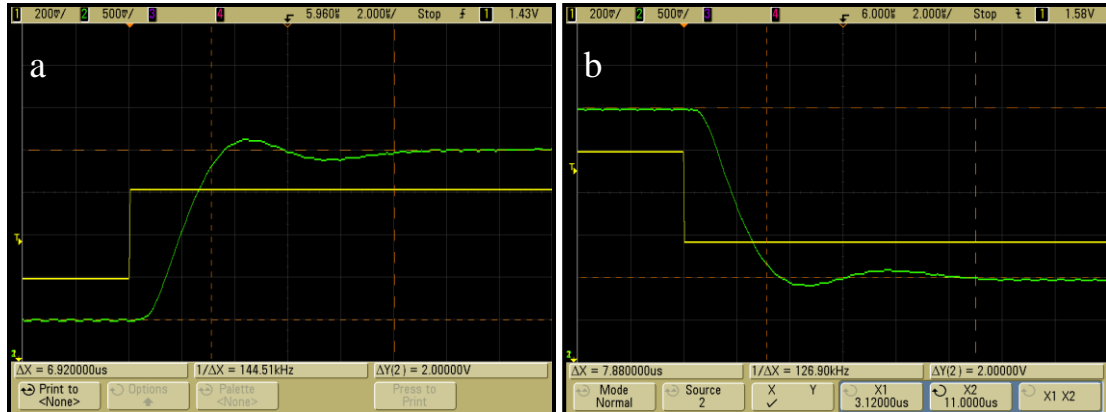
Figure 2-5-2) Small signal step response of buck modulator between 6 V and 8 V. CH1 (yellow) is the Vset input, and CH2 (green) is the V_D output. Trace averaging was performed (N=128) to filter out ripple voltage.

For large signal conditions, in which the duty cycle of the PWM modulator reaches its limits (0-86%), the response times of the converter are degraded, but still fast enough for operation with very short pulse spacings (down to 20 µs).
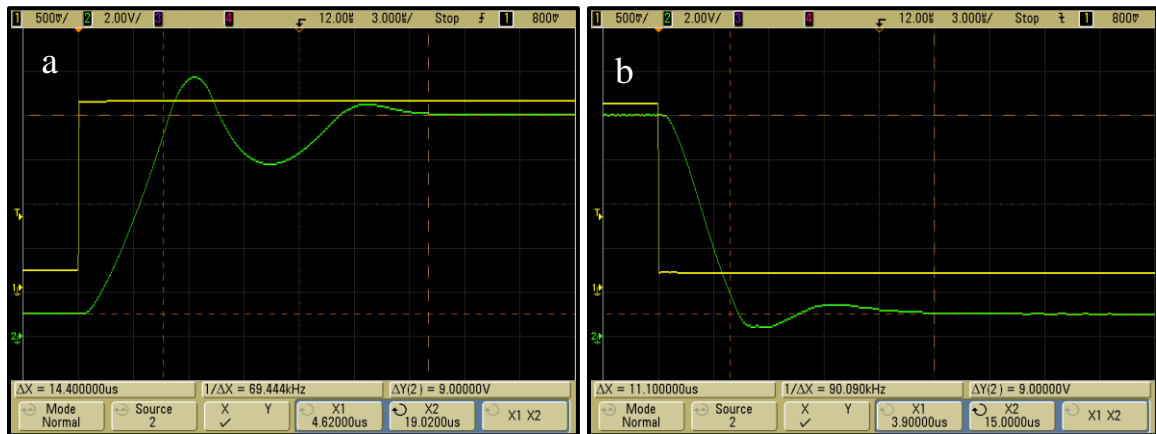
Figure 2-5-3) Large signal step response of buck modulator between 1 V and 10 V. Here the PWM modulator operates in its nonlinear range, causing distortion and slower settling time on the output

The efficiency of the buck modulator was measured by simultaneously measuring its input and output voltages and currents under varying loads. Measurements were taken with V_D set to both 12 VDC and 6 VDC. Vin was nominally set to 15 VDC. Figure 2-5-4 shows the efficiency results. These measurements include power consumed by the control circuitry and gate drivers.
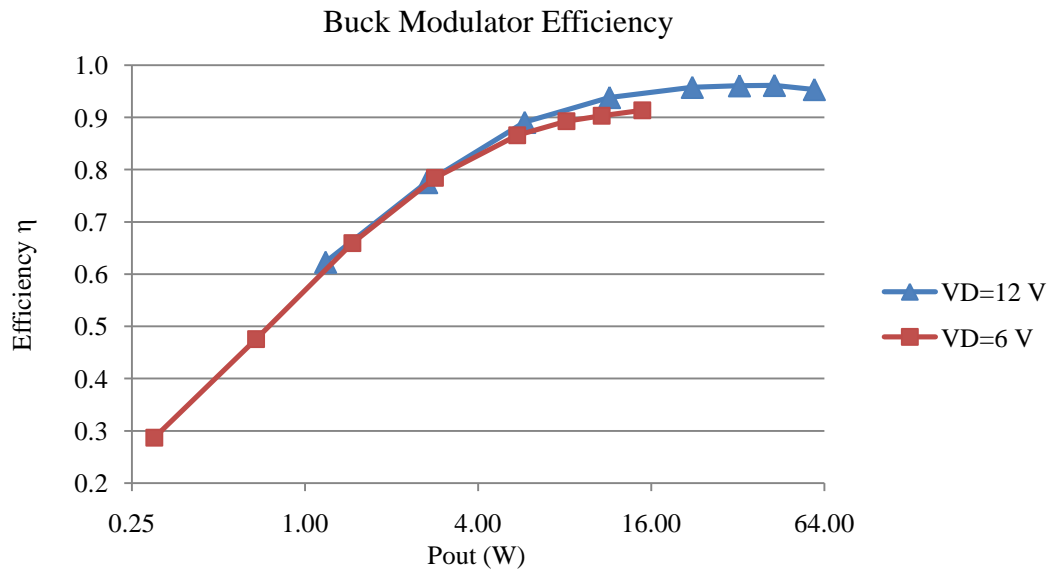
Figure 2-5-4) Efficiency of the buck modulator vs. output power

2-6 Low Noise Amplifier and RF Receive Chain (RFamp)

In a typical NMR system, the signal received by the sample magnetization is very weak and must be amplified significantly before it is sampled by the system. This is done by a low noise amplifier (LNA). The LNA is often followed by additional RF amplifiers to provide additional gain, and the combination of these gain stages is called the RF receive chain. The performance of the overall RF receive chain is primarily described by its gain and noise figure (NF). The RF chain's noise figure indicates how much the

inherent noise of the amplifiers (or any stage in the signal chain) degrades the SNR of the original signal [29].

The RF receive chain should be designed such that the maximum dynamic range (DR) of the NMR signal lies completely within the dynamic range of the receive chain. In this context, dynamic range is described as the range of signal power between the noise floor and the largest undistorted signal power. The ratio of these power limits is referred to as the dynamic range ratio (DRR).

The noise floor of an amplifier chain is, assuming no contribution from external sources, determined by the overall input-referred noise figure, the source impedance, and the bandwidth. Assuming an impedance match at the source, the noise power at 300K is [29]:

$$Noise(dBm) = -174 + NF + 10\log(BW) \qquad \text{Equation 2-6-1}$$

The NF of the overall system normally is dominated by the NF of the first amplification stage (the LNA) of the receive chain, and any losses between the signal source and its input (such as losses in the TRSW). This is demonstrated by the Friis noise formula, which gives the overall NF of a series of stages with known gains and NFs [29]:

$$F_{total} = F_1 + \frac{F_2 - 1}{G_1} + \frac{F_3 - 1}{G_1 G_2} + \dots \qquad \text{Equation 2-6-2}$$

Where in this formula F is noise factor and G is power gain (in linear units). These can be converted to log units by:

$$NF = 10\log(F) \qquad \text{Equation 2-6-3}$$

$$G_{dB} = 10\log(G) \qquad \text{Equation 2-6-4}$$

In a receive chain, it is desirable for the first stage (called the low noise amplifier, or LNA) to have high enough gain that the expression for F_{total} is dominated by F_1. It should also be noticed that any signal attenuation before the first gain stage will effectively add to the NF.

One of our principle design goals was broadband performance, which allows operation with a wide range of magnetic fields and different nuclear species. We aimed for an upper frequency limit of at least 64 MHz, which would allow ^{1}H experiments in common 1.5 T MRI scanners. We chose an upper frequency limit of 80MHz in order to ensure sufficient margin for this requirement. For a lower frequency range we chose 5 MHz. This corresponds to a field strength of 117 mT for ^{1}H, which is easily attainable with small permanent magnet arrays. Due to our desire for a wide operating bandwidth, we chose the MAR-6SM+ amplifier from Minicircuits for our LNA stage, with a rated NF of 2.3 dB, Gain=21 dB, and operating frequency range of DC-2 GHz. The MAR-6SM+ is rated for an absolute maximum input power of +20 dBm (100 mW).

The upper limit of the dynamic range is dependent on the various stages of the RF chain. Each stage has its own maximum signal power beyond which its effective gain will begin to decrease significantly. This is often characterized as the input-referred 1 dB compression point (IP1dB). The RF chain must be designed such that no stage exceeds its compression point when the maximum signal power is applied. Therefore for the nth stage of the RF chain, its IP1dB must exceed some level:

$$IP1dB_n \geq Pin_{max} + \sum_{i=1}^{n} G_i \qquad \text{Equation 2-6-5}$$

Where G_i is the gain (in dB) of the ith stage of the chain, and Pin_{max} is the maximum expected power (in dBm) at the input of the chain.

Determining the maximum input power Pin_{max} required estimating the nature of the actual NMR signal, which is dependent on the sample, the magnet, the coil, and the sequence. We consider an example experiment performed on the 8.35 MHz surface sensor and solenoid volume coil (see table 2-2-2) which is designed to yield maximum signal:

f_0	8.35 MHz
G_0	6.52 T/m
RF bandwidth	100 KHz
Sample	De-ionized Water (DI water)
Maximum sample radius	5.2 mm
B_1 efficiency	1.24 mT/A
Coil ESR	0.95 Ω

Table 2-6-1) Experiment parameters for hypothetical NMR signal power.

For this analysis we will use methodology proposed by [12] to estimate experimental signal and noise power.

The power delivered by a coil with equivalent series resistance R into a matched load is equal to:

$$P = \varepsilon^2 \Big/ 4R \qquad\qquad \text{Equation 2-6-6}$$

Where ε is the electromotive force induced by magnetization. The relationship between ε and the sample magnetic moment is given by:

$$\varepsilon = 2\pi f_0 \times m_0 \times B_1 \qquad\qquad \text{Equation 2-6-7}$$

Where f_0 is the precession frequency, m_0 is the sample magnetic moment, and B_1 is the B_1 efficiency (in Tesla per amp). The thermal equilibrium magnetic moment m_0 from a sample is given by:

$$m_0 = n\gamma^2\hbar^2 I(I+1)\frac{B_0}{3kT} \qquad\qquad \text{Equation 2-6-8}$$

Where n is the number of nuclei, γ is the gyromagnetic ratio of the nuclei, $\hbar$ is Planck's constant, I is the spin of a nuclei, B_0 is the static field strength, k is Boltzmann's constant, and T is absolute temperature. The volume of water excited by the pulses is dependent of the slice thickness Δy selected by G_0 and the pulse bandwidths. For G_0=6.52 T/m and BW=100 KHz, Δy=360 μm, giving an overall excited volume of 3.06×10^{-8} m^3. The abundance of ^1H in water is 6.69×10^{28} per cubic meter, giving an overall n of 2.047×10^{21} nuclei. The resulting m_0 is 1.928×10^{-11} A m^2. The resulting ε will be 1.254×10^{-6} V peak, and the delivered power is 2.08×10^{-13} W, or -96.8 dBm. Therefore for this experiment we needed an overall input referred compression point greater than -96.8 dBm.

For additional gain in the RF signal chain, we chose to use two gain stages after the LNA, each using the AD8331 variable gain amplifier from Analog Devices. The AD8331 allows for a voltage controlled gain between -8.5 dB and 37.5 dB, a NF between 4.5 dB and 40 dB (terminated with 50 Ω at input and output, for Vgain range of 0.1-1.0 V), and active input impedance matching. The AD8331 also has an operating bandwidth from DC to 100 MHz. The wide variable gain range was useful because it allows the upper limit of the dynamic range to be adjusted for different experiments (for example, experiments at high field strengths may require a lower gain to avoid compression).

A filter in between the two AD8331 stages may be used in order to limit the bandwidth of the RF output. This is useful because at high gain settings, large amounts of noise may cause the output to exceed its $IP1_{dB}$ point. By using a filter to limit the bandwidth of the receive chain, the total noise power on the output will be decreased, thus preventing compression without affecting the bandwidth of interest. For all

experiments discussed in this work, we used a 3rd order Chebyshev lowpass filter with f_c=20 MHz.

The RF receive chain had a two-way balanced power splitter on its output, allowing it to connect to the two RF ports of the downconversion stage (see section 2-7). The loss of the splitter was measured at -3.1 dB, which reduced the overall gain of the RF chain by 3.1 dB (measured from the input to each of the outputs).
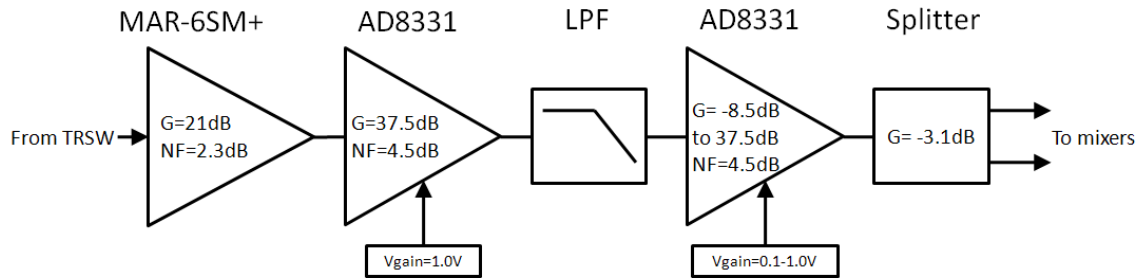
Figure 2-6-1) Simplified diagram of the RF amplifier chain

The gain of the entire receive chain, including the TRSW, LNA, two AD8331s, and the splitter were measured using the VNA, and are plotted below.
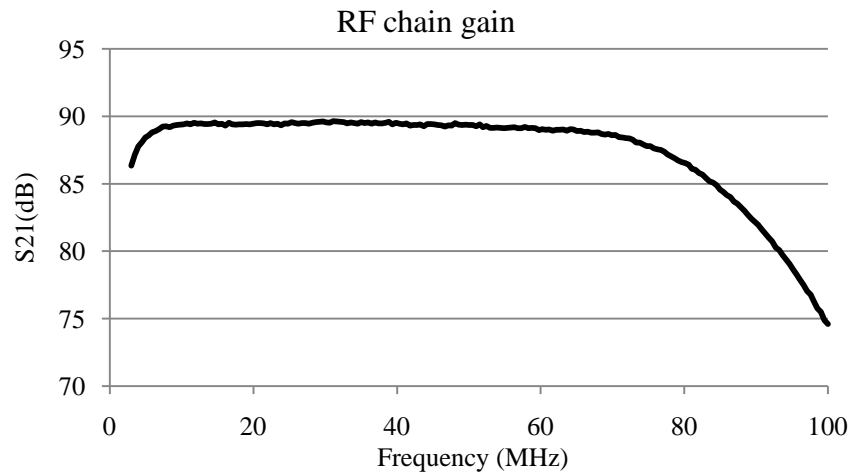
Figure 2-6-2) Gain of the RF amplifier chain, with maximum gain for both AD8331 stages

The output referred 1dB compression point (OP1dB) of the RF chain was measured using the VNA, and was found to be 0.9 dB. So even at maximum gain (89.2 dB at 8.35

53

MHz) the input referred IP1dB will be -90.1 dBm or greater, satisfying the requirements for the experiment above.

We also measured the NF of the entire receive chain using the SA and a noise source (model 346A from Agilent). Measurements were taken over the entire specified bandwidth, as well as at 8.35 MHz and 63.6 MHz (the Larmor frequencies for ^{1}H at 196.1 mT and 1.5 T, respectively). These measurements were taken with the gain control voltage of the second AD8331 stage lowered to 0.8 V, in order to avoid output compression during the test. The results are shown in figure 2-6-3 below:
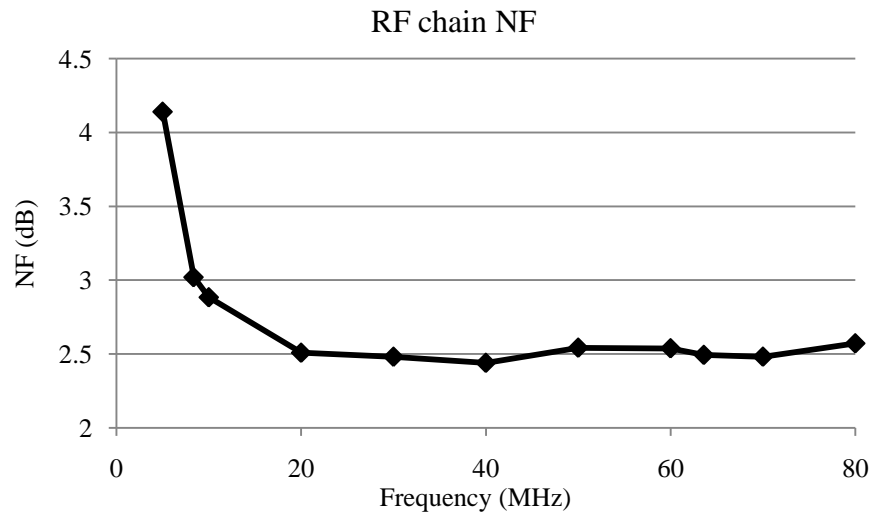
Figure 2-6-3) Measured NF of the RF amplifier chain, including the RXSW

For frequencies above 10 MHz, the NF of the RF chain is less than 3 dB. Under 10 MHz, the NF rises sharply, mostly due to the increased loss of the TRSW at such low frequencies. It should also be noted that the noise source used is not specified for measurement frequencies under 10 MHz, and therefore the NF measurements at lower frequencies may not be accurate.

2-7 Downconversion and sampling

Though the NMR signal is limited to a small bandwidth centered at f_0, the sampled signal is best analyzed in the rotating reference frame. This requires downconverting the signal to baseband. There are various methods of downconversion and filtering, using both analog and digital techniques. The goal of all downconversion methods is to preserve the sampled signal and reject signals outside the bandwidth of interest.

For our system we chose to use frequency mixers. Frequency mixers are devices with three ports, called RF, IF, and LO (respectively abbreviated for radiofrequency, intermediate frequency, and local oscillator). The RF signal (centered around f_0) to be downconverted is fed to the RF port, while a carrier signal with frequency f_{LO} is fed to the LO port. The mixer multiplies the signals on the RF and LO ports, and presents the product on the IF port. The result is two images (or sidebands) of the RF signal, now located at (f_0-f_{LO}) and (f_0+f_{LO}), each with half the original amplitude of the RF signal [30]. Normally only one of these images is desired, and the other is filtered off. Figure 2-7-1 shows the process of frequency mixing in the frequency domain.
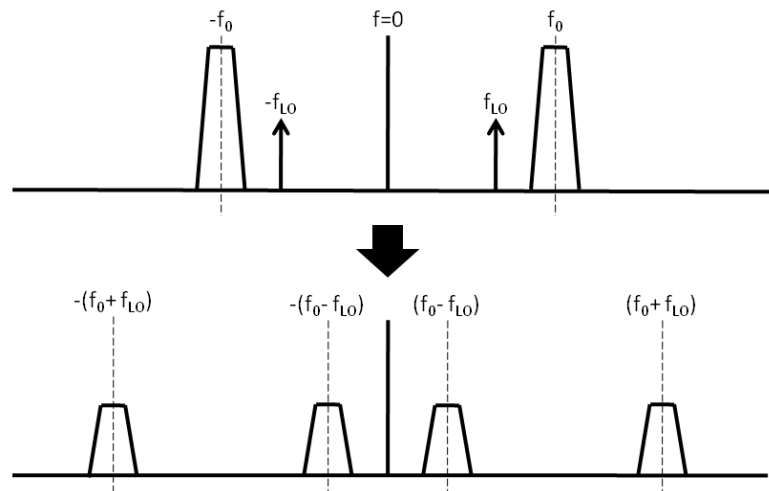
Figure 2-7-1) Frequency mixing of a real passband signal at f_0 with a LO carrier.

We chose to use a zero-IF downconversion system. In a zero-IF system, f_{LO} is set exactly to f_0, and the downconverted IF signal is centered at 0 Hz, and is therefore a baseband signal. Zero-IF downconversion simplifies the receive chain by eliminating the need for multiple frequency conversion stages, and only requiring lowpass baseband filters (as opposed to bandpass IF filters). To recover all information from the RF signal, two mixers are needed with orthogonal LO carriers, and both their outputs must be sampled together. This is referred to as quadrature detection [31].

For our frequency mixers, we chose to use the ADE-1L from Minicircuits. The RF ports were fed from the outputs of the 1:2 splitter in the RF receive chain. The LOs of the mixers were derived from the outputs of the direct digital synthesis (DDS) subsystem described in section 2-8 below. The independent DDS channels were used to phase shift the two LOs by 90°, thus allowing the mixers to output the in phase (I) and quadrature (Q) components of the RF signal.

The IF ports of both mixers were terminated with 50 Ω to preserve impedance matching on the RF ports. Baseband amplifiers were then used to amplify, bias, and filter the IF signals before being sampled by the ADC. The baseband filters were implemented as third order Bessel lowpass filters with f_c=180 KHz, and a passband gain of 23.8 dB.

We implemented the analog to digital conversion using a LTC1407A-1 14 bit, 2 channel simultaneous sampling ADC from Linear Technology. The ADC used an external voltage reference of 3.0V, and the baseband amp biased both IQ channels at half the reference voltage. The microcontroller firmware was capable of sampling rates of up to 577 Ksps on each channel, allowing digitization of baseband signals with frequencies up to 288.5 KHz (or RF signals with 577 KHz of bandwidth).
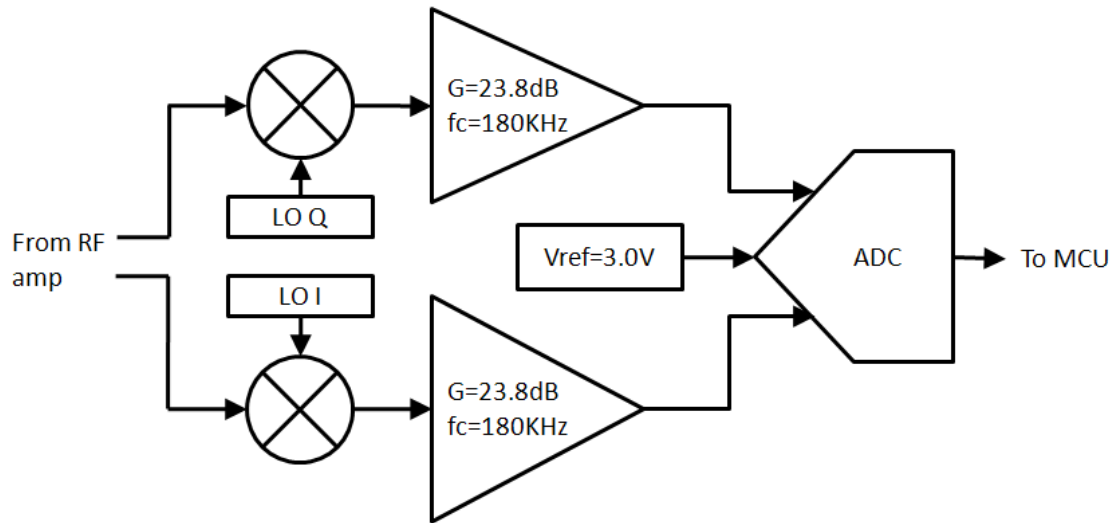
Figure 2-7-2) Simplified diagram of the downconversion stage, baseband amplifiers, and ADC

The overall conversion gain of this system, including the mixers and baseband amplifiers, was 18.5 dB (measured from the RF ports to each of the ADC inputs). Its noise figure is estimated to be 5.3 dB (equal to the conversion loss of the mixers). The large gain of the RF chain ensures that the contribution of the downconverters to the overall signal chain NF is negligible.

The downconversion and baseband stage has its own compression point, which in this case is dominated by the 3.0 V (or 13.55 dBm) full scale range of the ADC. This gives an IP1dB at the downconverter RF inputs of -3.95 dBm. This is lower than the OP1dB of the RF chain, meaning that the upper limit of the system dynamic range is dominated by the downconversion/baseband stage. Thus at maximum gain, the system IP1dB will be -93.15 dBm, and that will be the upper limit of the system dynamic range (at maximum RF gain).

The lower limit of the dynamic range is given by the input referred noise power within the bandwidth of interest. Applying equation 2-6-1 to this experiment (BW=100 KHz, NF=3.01 dB) yields an input referred noise power of -121 dBm. For maximum

gain, the overall input referred dynamic range will be -121 dBm through -94.15 dBm, and the dynamic range ratio will be 26.85 dB. The example experiment described in section 2-6 fits comfortably within this range. Though the DRR seems low, this is a worst-case result, which can be increased simply by decreasing the gain of the RF amplifier chain. With a the RFamp gain set to minimum (Vgain=0.1 V), the upper limit of dynamic range increases to -48.5 dBm, and the dynamic range ratio increases to 72.85dB.

2-8 Control System

The role of the control system is to synthesize and sample all necessary signals in the NMR system and execute the desired experiments. A control system must have at least a microprocessor (MCU) or programmable logic device (PLD) for timing of sequence events, interface with external peripherals, and various ADC and DAC capabilities. Often the real-time execution of the sequence and the analysis of data are done on separate systems.

Our control system was based on the AT32UC3C1512C microcontroller from Atmel. The MCU has a 32 bit architecture and operates at a maximum clock speed of 60 MHz. The AT32UC3C1512 was chosen mainly because in addition to being much more powerful than 8 bit RISC architecture MCUs, it has a relatively simple toolchain compared to sophisticated ARM MCUs, and therefore was a good compromise between performance and ease of development. The MCU controls the operation of the system through the use of several built in and external peripherals, as shown in figure 2-8-1.
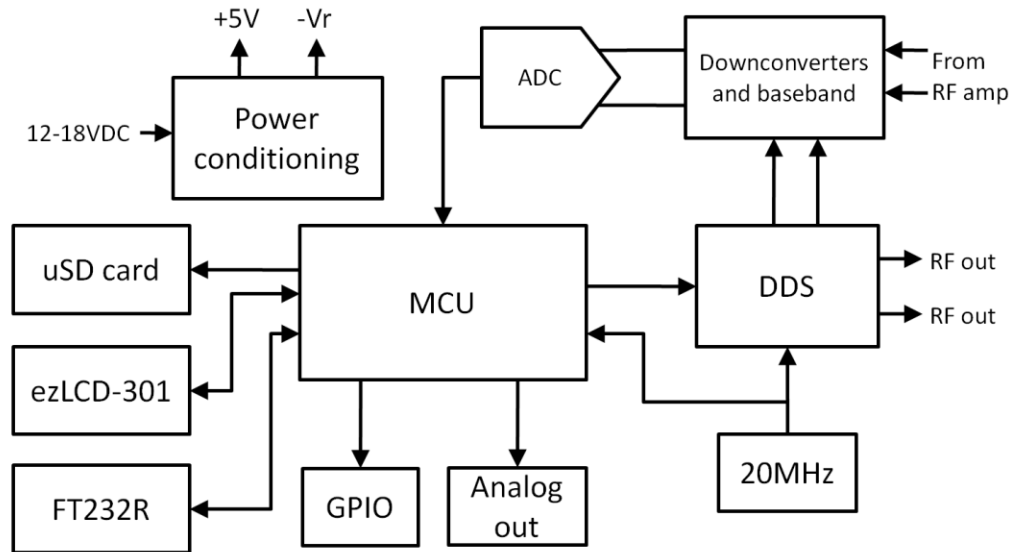
Figure 2-8-1) Block diagram of the control board and its various peripherals

Direct Digital Synthesis (DDS) RF synthesis

In order to create the necessary pulse sequences, it is desirable to have an RF synthesizer that is agile in both phase and amplitude, and has excellent frequency resolution. Direct digital synthesis (DDS) systems fulfill this role. The DDS also provides the LO signals for homodyne downconversion. Because of this requirement for two simultaneous, but separate RF channels, we chose the AD9958 from Analog devices. The AD9958 contains two separate channels (CH0 and CH1) that can be independently configured, but are internally synchronized, allowing them to be phase and frequency agile while eliminating the possibility of frequency or phase offsets between the channels. The AD9958 was controlled by the MCU via a Serial Peripheral Interface (SPI) bus, as well as several GPIO signals. In our application, we configured the DDS to have agile amplitude modulation, allowing the RF amplitude to be controlled by simply toggling GPIO signals, rather than manipulating registers inside the DDS via SPI. This

allowed for excellent timing resolution and consistency to be realized for rectangular RF pulses.

The AD9958 has a master clock frequency range of 100-500 MHz, allowing for synthesis of RF at frequencies of up to 200 MHz. We chose a master clock frequency of 300 MHz (derived from the 20 MHz reference oscillator), which allows for synthesis of frequencies up to 120 MHz. A 3rd order Chebyshev lowpass filter with f_c=80 MHz was fitted to each output, in order to reduce aliased signals propagating to the output ports. The filtered signals are then amplified with AD8008 amplifiers. Each channel was fed to a pair of amplifiers (G=15.7 dB), so that each channel could drive two different loads while preserving isolation between them. The amplifier outputs were given 50 Ω series resistors, since they were intended to drive 50 Ω matched loads. At maximum amplitude, each amplifier provided 4 dBm of RF power into a 50 Ω load. One amplifier from each channel also fed the LO port of one of the mixers. The other amplifier output was fed to a SMC coax connector to the TPA. Together, the DDS and these amplifiers were able to fulfill the role of providing a RF source for the TPA, as well as the LOs for both channels of the downconverter.
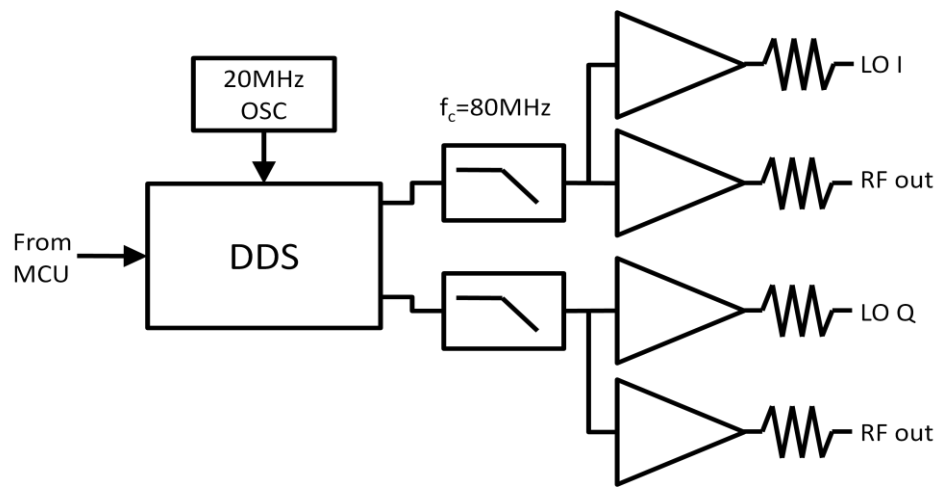
Figure 2-8-2) Simplified diagram of the DDS RF synthesis

USART to USB transceiver

For communication with a PC host, the control platform also included a FT232R universal synchronous/asynchronous receiver/transmitter (USART) to USB transceiver from FTDI. This allows simple communication with USB hosts using the MCU's USART port. While the FT232R was rated for USB 2.0 full speed operation (which would be 12 Mbaud/s), the FT232R is only specified for baud rates up to 3 Mbaud, or an effective 300 KB/s. It was found that when transferring large packets of data, the overall write speed was also impacted by wait states in the host's USB drivers, further limiting the effective write speed to less than 200 KB/s.

SD flash memory

Many of the envisioned NMR acquisitions require more samples than can be stored on the MCU's internal SRAM (64 KB). Therefore sampled data must be stored externally during the acquisition, either by sending it to a PC host via the FT232R transceiver, or by storing it on some external memory. Also in many experiments, the average sampling rate during a sequence was too high for the FT232R to transmit it to an external host. For acquisitions where both of these limitations are present, saving the sampled data to external memory was the only way to avoid losing data.

To solve this problem, we utilized a SD flash memory card on the control board. The MCU interfaced with the SD card via a separate SPI bus. The SD had a higher effective write speed (between 1-2 MB/s vs. 200 KB/s) than the FT232R, and much more capacity than the MCU (up to 32 GB vs. 64 KB). The high capacity also makes standalone operation feasible, since many hours of experimental data can be stored on the SD card for later use by a PC host.

LCD interface

For standalone operation it was necessary to provide an interface which allows the user to operate the system in the absence of a USB host. We selected the ezLCD-301 from EarthLCD, which is a "smart" LCD module including a resistive touch screen, an integrated LCD controller, and a microcontroller. The ezLCD-301 interfaces with the control via a USART, over which ASCII commands are sent. The ezLCD-301 handles all graphics processing, touch recognition, and display routines, which makes for very fast and simple development of the standalone UI.

The LCD is only necessary when operation in standalone mode is desired. For more information on standalone operation, see chapter 3-4.

General Purpose I/O (GPIO)

The control platform also made several of the MCU's general purpose I/O (GPIO) signals available on headers. These GPIO signals were used to control several of the peripheral systems:

- TXSW: controls the state of the TXSW of the TRSW

- RXSW: controls the state of the RXSW of the TRSW

- TPAEN: this enables or disables the operation of the TPA. For the CMCD TPA, this deactivates the gate drive circuitry for the GaN FETs.

- Buck shutdown: this optional signal can put the buck modulator into an idle state in which both FETs are held off. This prevents interference during the sampling period.

Analog output

The MCU contains two integrated digital to analog converters (DACs). Each DAC has 12 bits of resolution and a linear output range of 0.2-2.5 V with a 2.5V reference voltage. Each DAC output controls one of the following:

- Vset: This is the set point for the buck modulator output. It can set the modulator output level to between 1 VDC and 12 VDC.

- Vgain: This adjusts the gain of the second AD8331 stage in the RF amplifier chain. It provides a variable gain range of 46 dB.

Power conditioning

For the operation of the many subsystems, several different DC supply voltages were required. However, we desired to operate from a single DC supply (Vin) between 12-18 VDC. Therefore we required several DC/DC converters in order to derive the various required supply voltages. All of the necessary DC/DC converters were implemented on the control board (with the exception of the buck modulator, and the V_r generator, each of which had its own PCB).

- Vin to +5VDC: The 5V rail is distributed to most of the peripheral systems, including the FT232R, the RF receive chain, and the TRSW. The +5V rail is also used as the input to other DC/DC converters.

- +5VDC to +3.3V (digital): 3.3VDC is used to power the MCU and the DDS I/O port, as well as the ezLCD-301. This is implemented with a LMZ10501 step down module.

- +5VDC to +1.8V: 1.8VDC is used to power the analog and digital cores of the DDS (decoupled from each other with ferrite beads). This is implemented with a LMZ10501 step down module.

- +5VDC to +3.3V (analog): 3.3VDC is used to power the baseband amplifiers, and the ADC. This supply was implemented using a low noise LDO regulator, since the analog systems are sensitive to power supply rejection.

- Vin to V_r: There are two methods by which we produced the negative bias voltage V_r. For low power experiments, we used a LT1054 inverting charge pump to produce a regulated V_r of -13.5 V. When a higher power level is required, we used a Dickinson charge pump to produce an unregulated V_r between -45 V and -58 V.
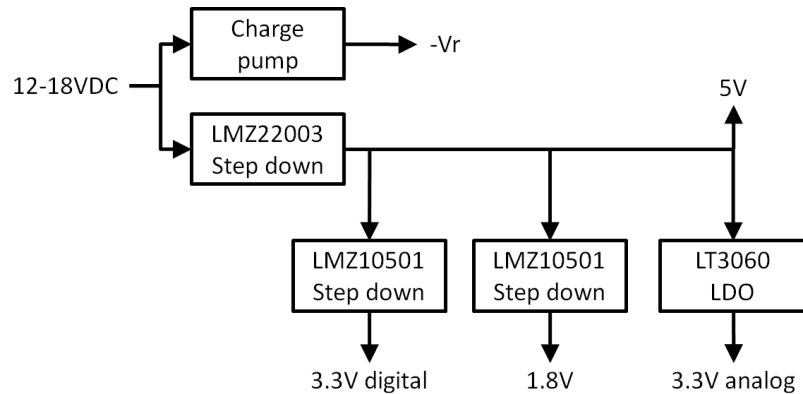
Figure 2-8-3) Block diagram of the power supply conditioning on the control board

The system was designed for use with a battery pack for standalone operation. We selected a 2.2 Ah 14.4 V NiMH battery pack from AA Portable Power Corp. The overall power draw of the system when idle is typically 3 W (2.5 W when the LCD is not used), and the power draw during sequence execution varies greatly depending on the experiment parameters. While power consumption may be very great during the execution of a pulse sequence, the typically low duty cycle of the sequence execution

greatly limits the average power consumption. For all of the experiments presented in this work, we estimate that average power consumption never surpassed 5 W. Thus we expect that a fully charged battery pack will provide over six hours of continuous experiment execution.

2-9 Enclosure and shielding

A shielded enclosure was necessary both to protect the system from mechanical harm and from electrical interference in the sensitive RF amplifier chain. The largest source of expected interference is not from external sources, but rather from the various switching power supplies within the system, especially the buck modulator. To reduce this interference, we created a compartmentalized enclosure which separates each PCB (the control board, RFamp/TRSW board, TPA board, and buck modulator board) into its own walled off compartment. The enclosure was designed in Google Sketchup, and fabricated using the Projet SD 3000 3D printer. Copper tape was applied to the inside of the compartments for the RFamp/TRSW, the TPA, and the buck modulator boards. A lid for the enclosure was laser cut out of acrylic. Copper tape was also applied to the bottom of the lid above the RFamp/TRSW compartment, for additional shielding of the most sensitive parts of the system. The LCD module is mounted to the acrylic lid, above the control board compartment (see figure 2-9-3).

To test the effectiveness of the shielding, the entire system was assembled and powered as if in operation. A shielded 50 Ω terminator was applied to the coil port, and one of the RF amp outputs was connected to a signal analyzer. To accurately emulate operating conditions during an ADC sampling period, the RXSW was forced on, and the

buck modulator was set to 6 V out, while the TPA was disabled. It was found that this shielding greatly reduced interference from all sources within the system. Figure 2-9-1 below shows the output spectrum of the RF amp without shielding applied:
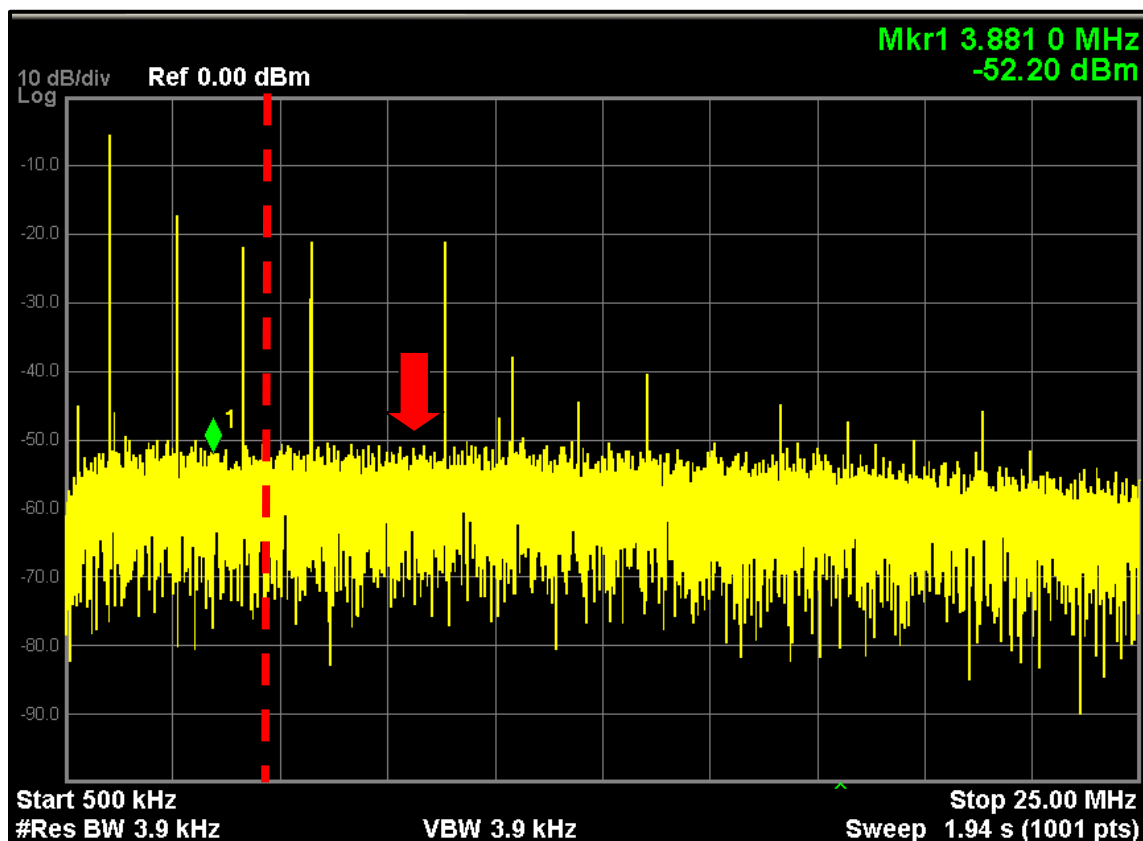
Figure 2-9-1) Output spectrum of the RFamp without shielding applied. The dashed red line shows 5 MHz, the lower end of the platform's specified bandwidth. The red arrow shows 8.35 MHz. Almost all interference is from the buck modulator, with some contribution from the LMZ22003

It can be seen that the interference from the buck modulator (1.54 MHz) is particularly strong. Though this frequency is out of the specified operating bandwidth of the system (5-80 MHz), it is nearly strong enough to cause compression in the RF amp at high gain settings, thus indirectly interfering with the NMR signal reception. There are also several harmonics of the switching frequencies within the operating bandwidth that are capable of interfering directly with the NMR signal if they happen to occur within the experiment's bandwidth of interest.
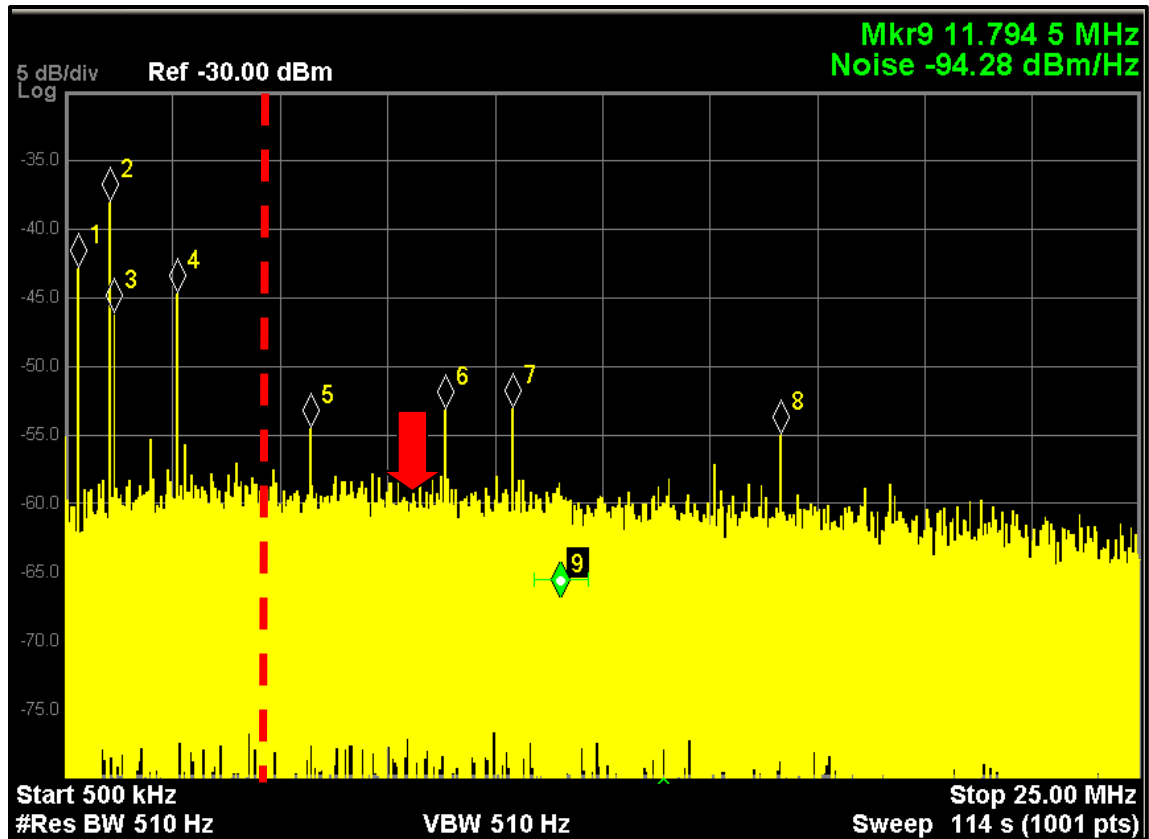
Figure 2-9-2) Output spectrum of the RFamp with shielding applied. The dashed red line shows 5 MHz, the lower end of the platform's specified bandwidth. The red arrow shows 8.35 MHz. All interference is significantly suppressed.

Figure 2-9-2 shows the output spectrum with shielding applied. All interference signals have been reduced to less than -35 dBm; low enough that none can contribute to compression at full gain. The harmonics within the bandwidth of interest were also greatly suppressed, the largest one being -50.81 dBm at 10.692 MHz. The spectral density of the noise floor was measured at -94.28 dBm/Hz. This interference signal contains power equal to 22.2 KHz of noise, and for any experiment with a bandwidth of interest greater than that, the interference will be below the thermal noise floor.

If this level of interference is unacceptable, then the buck modulator may be deactivated during the ADC readout, thus eliminating its interference completely. However, the buck modulator will take longer to recover from shutoff, and therefore care

must be taken when using this option in order to avoid distorting the RF pulses. Alternatively, the switching frequency of the buck modulator may be shifted slightly to avoid its harmonics falling within the experiment's bandwidth of interest.

A photograph of the fully assembled platform is shown in figure 2-9-3 below. The system measures 239 x 157 x 46 mm, and weighs approximately 3.0 lbs.
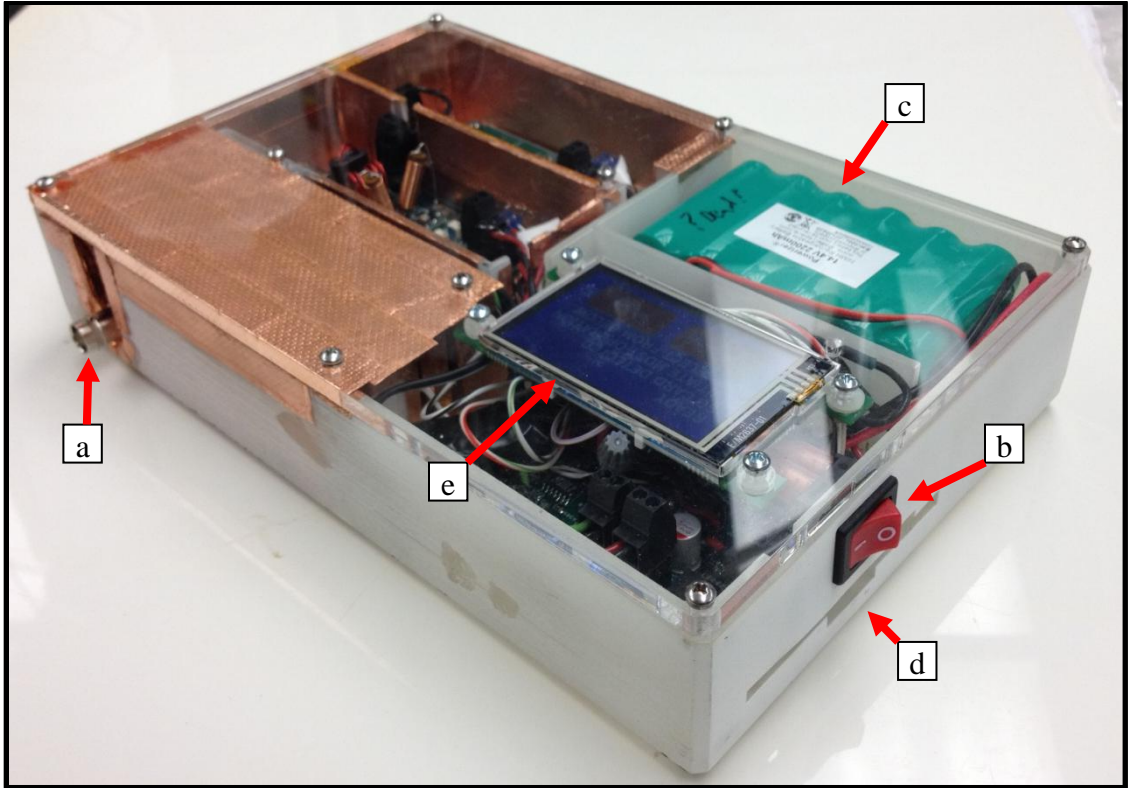
Figure 2-9-3) Photo of the fully assembled platform hardware. a) BNC Coil port of TRSW b) System power switch c) Battery pack d) Access slot for USB connector and SD card e) LCD module

Chapter 3: Sequence design, execution, and platform operation

This chapter will cover how the platform's hardware and firmware perform various experiments, and how data from those experiments is analyzed. First we will discuss the design of pulse sequences that allow us to observe various relaxation mechanisms. Second, we will explain how the platform hardware and firmware executes these sequences from a generalized experiment structure. Finally, we will discuss how the platform's user interface works, and how data is stored and transferred for analysis.

3-1 NMR sequence design

The design of a pulse sequence determines how the various NMR properties of a subject affect the sampled signal. Through proper design, a sequence can give rise to signal dependence on certain parameters, while rejecting dependence on other parameters. By fitting sampled data to models of NMR behavior, specific properties of the SUT can be determined.

The Carr-Purcell-Meiboom-Gill (CMPG) Experiment

A single sided NMR system such as ours was limited to sequences based on spin echoes due to the high spatial inhomogeneity in our main magnetic field. For maximum SNR, it was desirable to acquire many spin echoes per sequence. For this reason, we implemented a Carr-Purcell-Meiboom-Gill (CPMG) echo train in every pulse sequence. A CPMG echo train consists of a series of refocusing (180°) RF pulses spaced apart by echo time TE, with one spin echo occurring per pulse. The CPMG echo train begins with some initial magnetization, which may be provided by an excitation pulse, which is then followed by a series of refocusing pulses. The phase of the refocusing pulses should be

such that B_1 is in the same direction as the initial magnetization in order to prevent loss of signal due to flip angle errors in the refocusing pulses [32]. During the echo train, the echo amplitude will decay exponentially according to the following formula:

$$M_{xy}(t) = M_{xy}(0)e^{-t/T_{2a}}$$

<div align="right">Equation 3-1-1</div>

Where $M_{xy}(0)$ is the initial transverse magnetization at the beginning of the CPMG, and T_{2a} is the effective decay rate of the spin echoes in the CPMG. Figure 3-1-1 below shows a sequence diagram of a CPMG that begins with a spin echo (created by some preparation sequence, not shown):
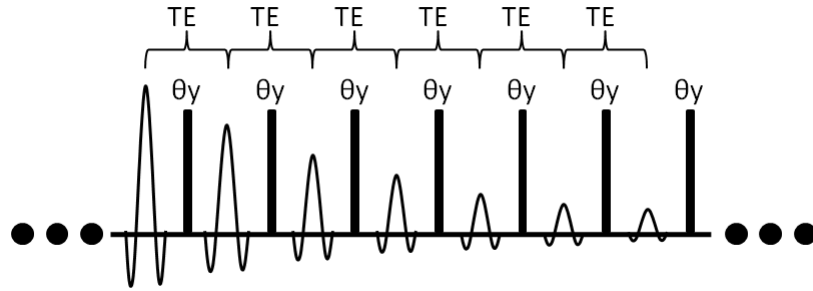
Figure 3-1-1) CPMG readout sequence diagram, showing decay in spin echo amplitude

The apparent decay rate T_{2a} is determined by the spin-spin relaxation time T_2, as well as self diffusion (D) in the static gradient (G_0). T_{2a} is given by [11]:

$$T_{2a} = \left(\gamma^2 G_0^2 TE^2 D / 12 + 1 / T_2 \right)^{-1}$$

<div align="right">Equation 3-1-2</div>

The above formula shows that the decay rate of the echo train is weighted by T_2 and D, making it useful for measurement of those parameters. Also, by sampling many echoes and fitting them to an exponential model, the initial transverse magnetization $M_{xy}(0)$ can be measured with an improved SNR compared to simply sampling a single echo with no echo train [7].

CPMG with simple excitation pulse

In addition to the CPMG, a preparation sequence is used to create the initial magnetization. The simplest preparation sequence is a simple 90° excitation pulse, spaced τ=TE/2 before the first refocusing pulse of the CPMG. The phase of the refocusing pulses is orthogonal to the excitation pulse, as described by [32]. Figure 3-1-2 below shows a simple CPMG sequence diagram:
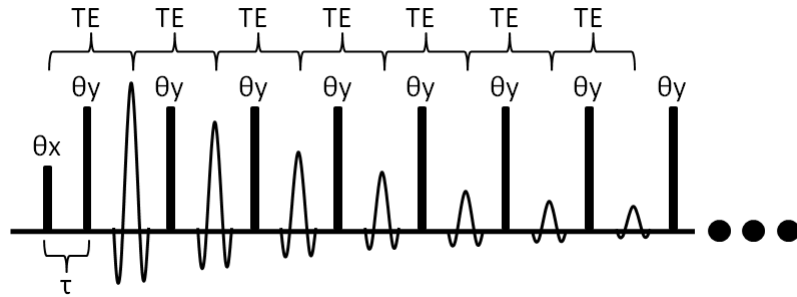
Figure 3-1-2) CPMG sequence starting with a simple excitation pulse

In this sequence, the amplitude of the CPMG echoes will follow the formula:

$$M_{xy}(t) = M_z(0)e^{-t/T_{2a}}$$

Equation 3-1-3

Where $M_z(0)$ is the longitudinal magnetization just prior to the magnetizing pulse. This sequence yields information on $M_z(0)$, as well as spin density ρ_0. By doing several CPMGs with different TE and measuring its effect on T_{2a}, the values of T_2 and D can be determined by fitting the data to equation 3-1-2.

In reality, the measured T_{2a} resulting from a CPMG will always be somewhat longer than that predicted by equation 3-1-2. This is because imperfect RF pulses will tip the spins with a wide distribution of flip angles, rather than just 0°, 90°, or 180° as desired. This leads to some magnetization evolving along echo pathways not accounted for in the model above. For example, magnetization in the longitudinal axis will not dephase due to self diffusion, but will relax according to T_1 towards the equilibrium

magnetization M_0 [33]. Thus if T_2 and D must be known accurately, the variable TE CPMG is not suitable for surface magnet experiments. However, if weighted contrast is merely desired, and the actual values of T_2 and D are not important, then the variable TE CPMG is still applicable.

Inversion recovery

T_1 can be measured by using an inversion recovery sequence. This sequence consists of the simple CPMG sequence described above, with the addition of an inversion pulse placed at a time TI before the excitation pulse, shown in figure 3-1-3 below:
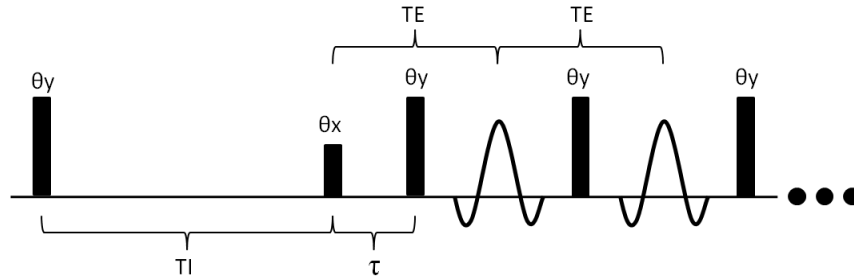
Figure 3-1-3) Inversion recovery preparation, and start of a CPMG readout

This results in the longitudinal magnetization being weighted by both T_1 and TI according to the following equation:

$$M_z(TI) = M_0 - (M_0 + M_z(0))e^{-TI/T_1}$$

Equation 3-1-4

Where $M_z(TI)$ is the longitudinal magnetization at time TI, just prior to the excitation pulse, M_0 is the equilibrium longitudinal magnetization, and $M_z(0)$ is the longitudinal magnetization just prior to the inversion pulse at t=0. In experiments where TR>>T_1, $M_z(0) \approx M_0$, and the equation reduces to:

$$M_z(TI) = -M_0 e^{-TI/T_1}$$

Equation 3-1-5

By varying TI and measuring its effect on $M_z(0)$, the T_1 of the sample can be determined [11].

Variable relaxation diffusion sequence

One of the simplest methods of measuring both T_2 and D is by using a single spin echo with varying TE_1. The spin echo may then be read out using a CPMG for increased SNR. This sequence is shown below:
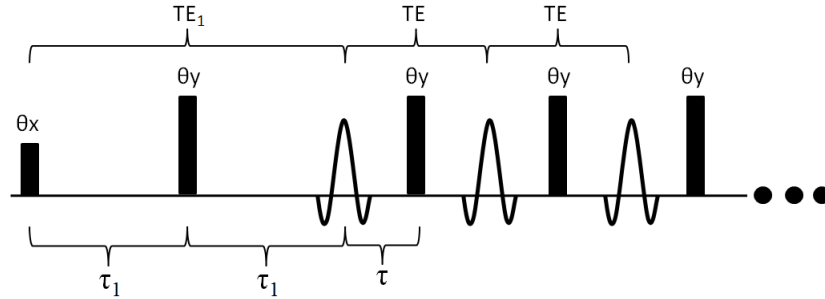
Figure 3-1-4) Sequence diagram for variable relaxation diffusion sequence

For such an experiment, the magnetization of the echo occurring at TE_1 is:

$$M_{xy}(TE_1) = M_z(0)e^{-\frac{2}{3}\gamma^2 G_0^2 D\tau_1^3} e^{-2\tau_1/T_2}$$

Equation 3-1-6

Where τ_1 is half the TE_1 of the spin echo.

A major problem with this experiment is that varying TE_1 affects the weighting of both T_2 and D on the resulting $M_{xy}(TE_1)$, making it difficult to measure D if T_2 is not accurately known, and vice versa.

Constant relaxation diffusion sequence

Another preparation sequence proposed by [34] is a constant relaxation time diffusion weighted sequence. The transverse magnetization from an excitation pulse is refocused twice with τ_1 and τ_2, and an echo at t= $2(\tau_1 + \tau_2)$ results, with magnetization $M_{xy}(2(\tau_1 + \tau_2))$. This is given by:

$$M_{xy}(2[\tau_1 + \tau_2]) = M_z(0)e^{-\frac{2}{3}\gamma^2 G_0^2 D(\tau_1^3 + \tau_2^3)} e^{-2(\tau_1+\tau_2)/T_2}$$

Equation 3-1-7

Where $M_z(0)$ is the longitudinal magnetization just before the excitation pulse. The echo at $t=2(\tau_1 + \tau_2)$ is then refocused with a CPMG. The full sequence is shown in figure 3-1-5 below:
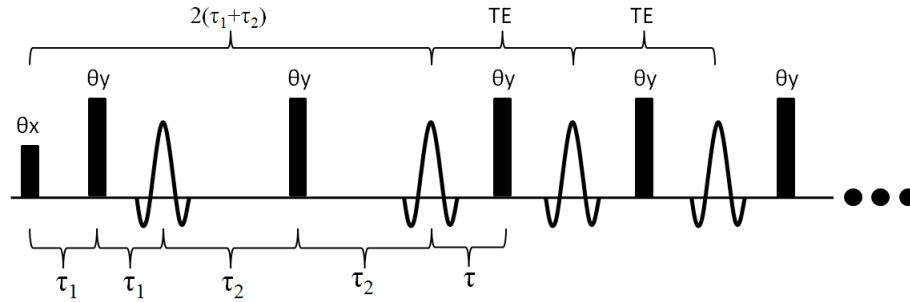
Figure 3-1-5) Constant relaxation preparation sequence, with start of CPMG readout

If τ_1 and τ_2 are varied such that $\tau_1 + \tau_2$ is held constant, changes in $M_{xy}(2(\tau_1 + \tau_2))$ will be weighted by D but there will be no differences in the T_2 contribution, yielding a T_2 independent measure of D.

Phase cycling

NMR sequences with short TEs will often suffer from artifacts in the received signal due to recovery from the RF pulses. Causes of such interference include coil ringing, magnetoacoustic ringing, receive chain recovery and simple DC-level offsets (see chapter 2). The characteristics of such artifacts are usually coherent and depend on the phase and amplitude of the RF pulses. Since they are coherent, they cannot be diminished by successive averaging, but they can be nulled by inverting either the spin echo or the RF pulses between sequence repetitions, and then adding or subtracting them to cancel out the artifacts.

We implemented a phase cycling routine in which sequences were repeated with the excitation pulse phase shifted by 180° in between repetitions. This resulted in the phase of the spin echoes also being shifted by 180°, while the artifacts, which were

coherent only with the refocusing pulses, were unaffected. Taking the difference between the raw data sets yielded the spin echo without coherent artifacts [35].

The figures below show how phase cycling is used to greatly reduce the impact of ringing artifacts on an acquired echo. Figure 3-1-6a is the third echo of a CPMG with the phase of the excitation pulse set to 0°. Figure 3-1-6b is the third echo of an identical CPMG, except the excitation phase is set to 180°. One can see that the spin echo has been inverted, while the large artifact from receiver recovery is not. Taking the difference between the two yields an undistorted spin echo (figure 3-1-6c), while taking the sum shows the artifact alone, without the echo (figure 3-1-6d).
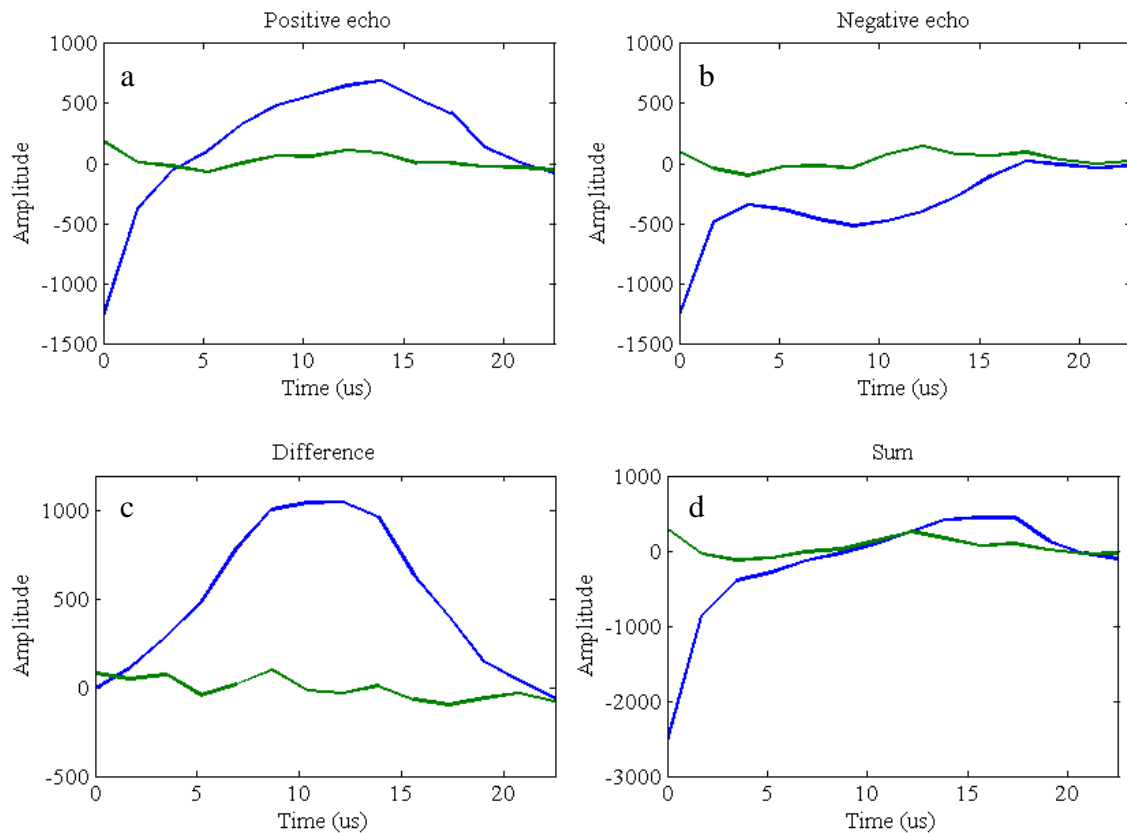
Figure 3-1-6 a-d) Elimination of ringing artifacts from one spin echo via phase cycling

3-2 Hardware sequence implementation

Pulse synthesis

While the delivery of an RF pulse may seem like a simple event, its synthesis is a complex and configurable task which takes place in several stages. This section will describe how an RF pulse is synthesized step by step, and how the properties of the pulse were defined by configurable parameters.

Initial conditions

Before the start of the actual RF pulse routine, it is assumed that the RF signal supplied to the TPA input is disabled (done by amplitude modulating DDS CH0 to zero). The desired phase of the RF pulse is already loaded into the phase offset word (POW) register of the DDS channel, and the desired RF amplitude is programmed into one of the amplitude modulation registers. The set point of the buck modulator has already been set to the desired level for the next RF pulse. The TPA is disabled by de-asserting TPAEN. To conserve power and reduce interference, the buck modulator may be disabled. Also the TRSW starts with both the TXSW and RXSW in the isolated state.

Step 1: TXrise

Before the start of the actual RF pulse, the TXSW must be configured to couple the TX port to the coil port. This interval also provides additional time for the buck modulator to reach a steady state, if it was deactivated during a previous sampling period. This period, in which the TXSW and buck modulator are allowed to reach steady state, is called TXrise.

Step 2: RF and TPA enable

In this step the RF signal to the TPA is enabled, beginning the true RF pulse. This is done by amplitude modulating the CH0 output using the channel profile registers and pins. At the same time, the TPA is enabled by asserting the TPAEN signal.

Step 3: Pulse end

After waiting for the desired length of the pulse, the pulse is terminated. First, DDS CH0 is amplitude modulated back to zero, the TPAEN signal is de-asserted, and the TXSW is switched back to isolated mode. The buck modulator may optionally be disabled at this point.

Immediately after the end of the RF pulse, DDS CH0 is reconfigured for its next task (either another RF pulse, or providing the LO for one of the downconverters). The set point for the buck modulator is changed to the desired level for the next RF pulse. Also, if an echo is to be sampled next, RXSW will be enabled at this point.

A number of user-definable parameters are used for pulse synthesis:

- `TXrise`: The amount of time (in microseconds) between enabling the TXSW and buck modulator and the start of the RF pulse itself. Typically between 4-10 µs.
- `Pulsewidth`: The duration (in microseconds) of the RF pulse itself. Typically between 3 µs and 1000 µs.
- `RFamp`: The amplitude (in LSBs of the DDS ASF register) of the RF given to the TPA input.
- `RFphase`: The phase (in LSBs of the DDS POW register) of the RF given to the TPA input.
- `Vd`: The set point given to the buck modulator. This defines the supply voltage given to the TPA. This value is specified in LSBs of the MCU's DAC.

Echo sampling

The sampling routine is also a highly configurable process which occurs in several steps as follows:

Initial conditions

The start of a sampling period will always follow the end of an RF pulse, and therefore the sampling routine will begin with the DDS already configured for the sampling routing (as described in the previous section). Both DDS channels will be configured to give the desired LO amplitude. The phase of CH0 will be set to the desired phase offset defined by the user, and CH1 will always be set to lead CH0 by 90°.

Step 4: ADC sampling

The MCU commands the ADC to sample and convert both I and Q baseband channels simultaneously by pulsing its CONV pin high. The MCU will then read out a conversion result over the SPI bus. Conversions will repeat for as many times as specified by the user, with the specified sampling period.

Step 5: Reconfiguration

After the end of the last sample and transfer, the DDS will again be reconfigured for its next task (the next pulse of the CPMG). CH0 will be amplitude modulated back to zero, and its POW will be set to the desired phase of the next RF pulse.

The following parameters are used for echo sampling:

- `LOamp`: The amplitude (in LSBs of the DDS ASF register) of the RF given to both LO ports.
- `LOphase`: The phase (in LSBs of the DDS POW register) of the LO given by CH0 to the quadrature downconverter's LO. The phase of the imaginary downconverter's LO will be set to lead this phase by 90°.
- `dt`: The time (in microseconds) between ADC samples.

- `Nsamp`: The number of ADC samples per echo.
- `samp_offset`: The timing offset (in microseconds) given to the sampling routing. This allows the user to compensate for delay in the RF chain so that the center of the echo is in the center of the sampling period.

Figure 3-2-1 below shows a detailed diagram of the steps of sequence execution. The diagram covers the synthesis of a RF pulse and the sampling of a spin echo in the middle of a CPMG readout.
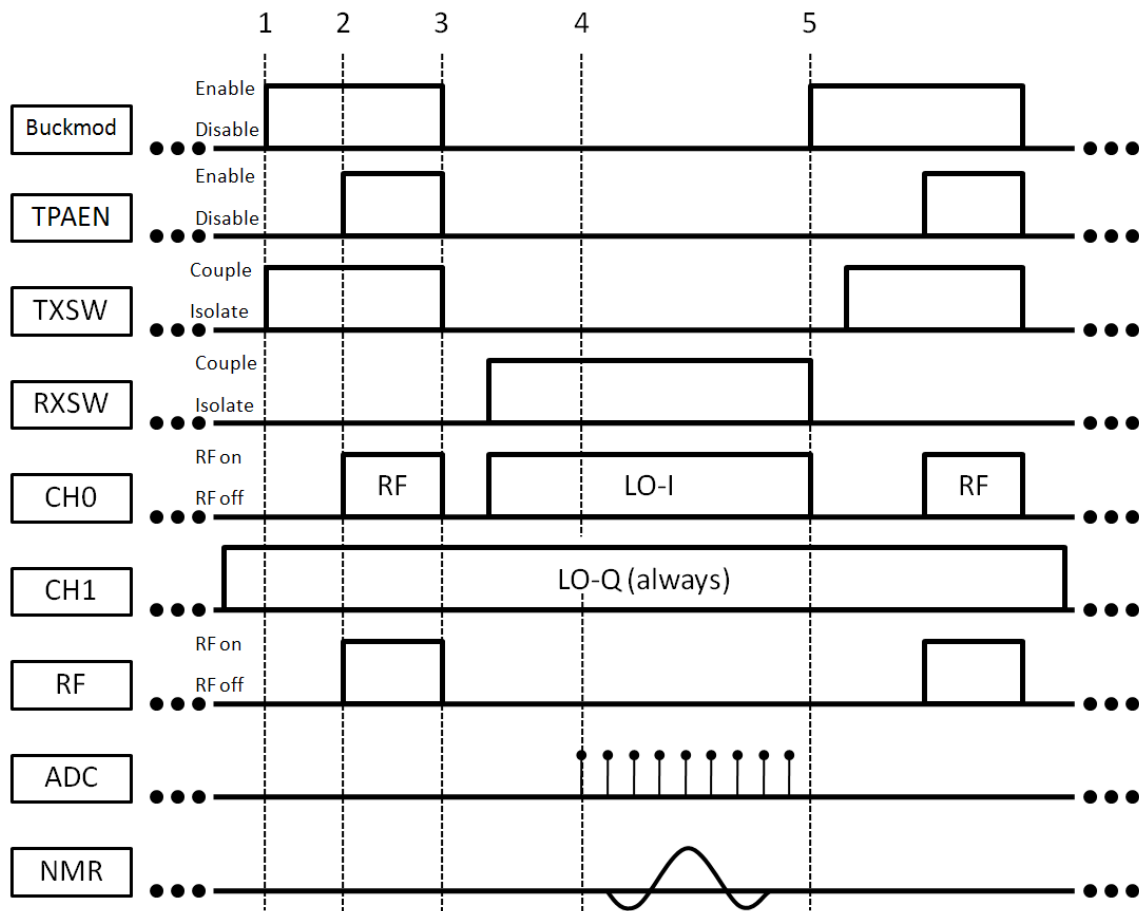
Figure 3-2-1) Detailed operation of the peripherals platform I/O for synthesizing a RF pulse and sampling a spin echo during a CPMG. The five steps of the process, as described above, are labeled in the diagram.

Offset readout

DC offsets in the baseband signals were observed due to offsets in the baseband amplifiers, and interference at f_0 in the receive chain. We desired to compensate for this offset by performing a short readout of the baseband signals at steady state (in the absence of any RF pulses or spin echoes). This was done with the same configuration as is used in the sampling period of the CPMG. The offset readout was also governed by the following firmware parameters:

- `Noffsetsamples`: Number of samples to take during the ADC readout.
- `dt_offsetsamples`: Sampling period of the offset samples.

3-3 Firmware sequence implementation

To accommodate a wide variety of desired experiments, we have implemented a very flexible method of defining sequence parameters in the MCU firmware. In the firmware, all the properties of a desired NMR experiment were contained in a single data structure called `experiment`. The following section will explain how this structure was organized from top down:

`experiment`:

- `sequence[1:8]`: `experiment` contained 8 sequences, each of which was a `sequence` structure.
- `TXrise`: `TXrise` was the time (in microseconds) given for the TXSW to reach steady state before the start of a RF pulse.
- `Nsequences`: The number of actual sequences to perform per experiment.
- `Nexperiments`: The number of times to repeat the experiment. Used in standalone mode only.
- `Noffsetsamples`: The number of samples to take during each offset readout.
- `dt_offsetsamples`: The sampling period (in microseconds) of the offset samples.
- `Vgain`: The voltage given to the RF amplifier chain which determines its gain.

`sequence:`

- `f0`: The RF and LO frequency during the entire sequence.
- `preppulse[1:4]`: Each `sequence` may have between 1 and 4 preparation RF pulses, each of which is a `preppulse` structure.
- `Npreppules`: The number of preparation pulses actually used in the sequence.
- `CPMG`: The `CPMG` structure describes the parameters of the sequence's CPMG readout.
- `TR`: The time (in seconds) between the first pulse of each sequence. This parameter was used only in standalone mode.
- `Echofirst`: Determined whether the sequence uses a CPMG starting with an echo sample, or a refocusing pulse

`preppulse:`

- `Pulsewidth`: The duration (in microseconds) of the preparation RF pulse
- `RFphase`: The phase of the preparation RF pulse.
- `RFamp`: The amplitude of the RF fed to the TPA.
- `Vd`: The bias voltage set point of the buck modulator.
- `tau`: The delay until the next RF pulse. Defined as the time between the centers of the pulses.

`CPMG:`

- `Pulsewidth`: The duration (in microseconds) of the refocusing RF pulse
- `RFphase`: The phase of the refocusing RF pulse.
- `RFamp`: The amplitude of the RF fed to the TPA.
- `Vd`: The bias voltage set point of the buck modulator.
- `tau`: The time between the center of the refocusing RF pulses and the center of the expected echo. Always equal to TE/2.
- `LOamp`: The amplitude of the LO fed to the downconverters.
- `LOphase`: The phase of the quadrature LO.
- `Nsamp`: The number of samples per echo.
- `dt`: The sampling period of the ADC.
- `samp_offset`: Offset of the sampling window from the expected echo time
- `Nechos`: The number of echoes in the CPMG.
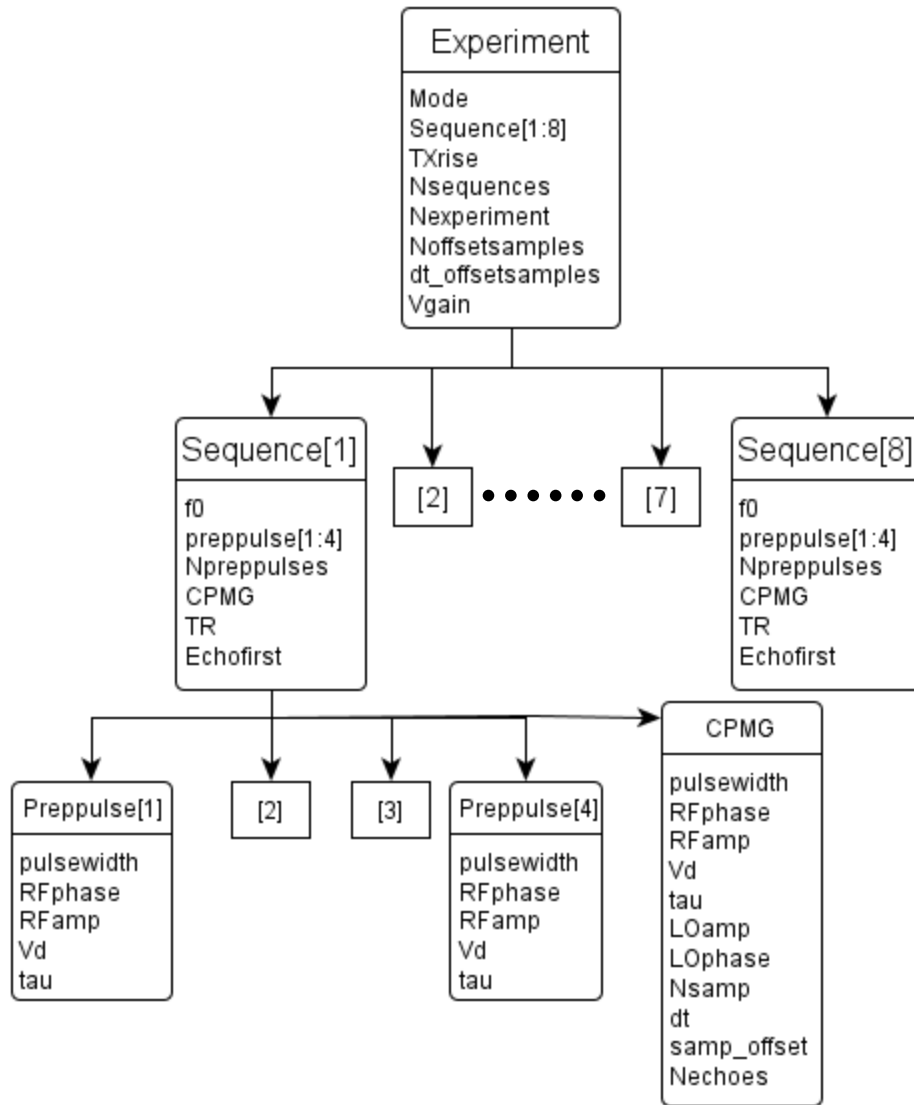
Figure 3-3-1) Hierarchy of the `experiment` structure

Experiment verification and conversion

When beginning a new experiment in standalone mode or host mode, the MCU first runs a verification and conversion routine on the experiment structure. First the firmware ensures that all of its parameters are within tolerable range and that the parameters together create feasible sequences. If it fails this verification it will show an error message on the user interface and halt execution.

If `experiment` passes verification, it will convert many of the parameters of experiment into forms which can be directly used by control system peripherals. For example, phase parameters, such as RFphase and LOphase (which are specified by the user as single precision floating point numbers, in degrees), are converted to 14 bit integers for use by the POW registers of the DDS. Various timing parameters (which are specified by the user as single precision floating point numbers, in microseconds) must be converted to unsigned 16 bit integers for use in the MCU's Timer/Counter (TC) peripherals. Some groups of timing parameters are compiled into single time intervals, for more convenient use by the MCU. The results of this conversion are stored in a new structure called `t_experiment`. `t_experiment` contains all data that is directly used by the MCU firmware to execute the sequence.

The final step of the process takes the contents of `t_experiment` and converts it back into the format of `experiment`. This result will be similar to the original experiment specified by the user, but will accurately reflect any changes in floating point parameters due to truncation and rounding in the conversion process. The contents of this "true" experiment structure are used when analyzing the sampled data.

SD flash memory and sampling operation

In order to accommodate sequences that demand high sampling rates and high sample counts, an external flash memory micro-SD card was used for the temporary storage of sampled data. This section details how the memory was handled during the sequence execution.

To achieve a high overall write speed to the SD flash memory, sampled data was transferred in clusters of 32 blocks, with each block consisting of 512 bytes of data. The

MCU firmware defines two data banks, each 16KB in length, called `bank0` and `bank1`. At any given time during a sequence, one of these banks (for example, `bank0`) will be designated a sink, and will be written with new data from the ADC. At the same time, the other bank (`bank1` in this case) will be designated as a source, and will have its contents transferred to the SD card as one cluster. When a sink buffer is filled with new ADC data, the banks will switch roles automatically. New ADC samples will be stored in `bank1`, and the contents of `bank0` will be transferred to the SD card. The operation of these banks allows data to be transferred from the ADC to the SD card without interruption.

In order for this transfer of data to occur without loss, a cluster transfer must finish before the new ADC bank is filled. This puts an effective limit on the effective sample rate that can be achieved. With fast SD cards, effective write speeds of 2.0Mb/s have been realized. However, during an actual sequence, the SD protocol operations are only executed once per echo, and only up to one block can be transferred per operation. Thus the sampling rate is also limited by 512 bytes per TE of the CPMG, or 128 samples per echo. This limitation becomes relevant for sequences with long TEs, but is not a significant limitation because 128 samples per echo was determined to be more than adequate for the experiments performed during this work. With faster sequences with shorter TEs, the overall sampling rate will be defined more by the SD card's own timings, and the speed of the SPI bus. Overall sampling rates in excess of 250 Ksps have been realized.

Under certain conditions, a read or write operation of the SD card may take much longer than usual (up to 250 ms). These "rogue operations" are a result of the internal operation of the SD card's memory controller, and are impossible to prevent entirely.

While extremely rare, these events will often result in losses of entire clusters, likely making the sequence data useless. When this occurs, the firmware will recognize that a buffer overrun has occurred and will flag the entire sequence as corrupted. When this occurs, the firmware fills the SD memory dedicated to the current sequence with 0xFF, but subsequent sequences should not be affected.

Data transfer to host

In host mode, sampled data is transferred to the host after the completion of each sequence. Similar to the way in which ADC samples are stored to the SD card, the SD card contents are read into one of the two data banks, while the other data bank sends read data to the host PC via the FT232R USART to USB converter. The time required for this transfer is determined by the FT232R, which has a much lower transfer rate than the SD card. Therefore the TR of the experiment must be enough to allow this transfer of data to take place after each sequence.

In standalone mode, the first cluster of the SD card is written with the experiment structure before the start of the actual experiment. As the experiment progresses, sampled data clusters are written to the SD card until the experiment ends. In order to export the sampled data to the host for analysis, the control board must connect to the host via USB and the host must command the MCU firmware to transfer the data (including the experiment structure) via USB.

On rare occasions, it was observed that the SD card would enter a "corrupted" state in which data read from the SD card was incorrect, despite the SD card not returning any error flags during operation. The frequency of this problem varied greatly depending on the specific type of SD card and the average data rate of the sequence. Once in such a

state, the SD card will continue to return incorrect data until it is erased or reformatted. When necessary, this was done by connecting the SD card to a computer running a Windows operating system and choosing to reformat the memory. We believe this is a fault in the internal memory controller of the SD card. It is likely that using a 4-bit SD interface instead of a 1-bit SPI interface would solve this issue.

3-4 User interface

The platform has two user interfaces (UI). One is provided by a host PC running MATLAB, and another is provided by the platform hardware in the form of a touch LCD module controlled by the MCU firmware. Together, these interfaces allow the user to operate the system in both standalone and host modes.

Upon powering up the system, the MCU firmware enters an idle state in which it waits for commands from either UI. From this idle state, a number of operations can be done:

Check SD card

This command can be issued by either UI. The firmware will check the status of the SD card, and will report it via the UI from which it received the command.

Program experiment to SD card

This command is issued by the host UI. It takes an experiment structure defined in MATLAB and sends it to the platform via USB. The platform checks the SD card and validates the experiment, and if both pass validation, the firmware will store the experiment in the SD card for later use.

Begin standalone operation

This command is issued by the LCD UI. If a valid SD card with a valid experiment is recognized, the UI will prompt the user to begin standalone execution of the experiment.

During standalone execution, the LCD will display the progress of the experiment. The specified experiment will run until the user manually halts the experiment via the LCD interface, the experiment finishes its specified number of iterations, or the firmware is manually reset (by a hard reset, or by loss of external power).

Begin host mode

This command, issued by the host UI, initiates the platform for host mode operation. Upon receiving the command, the firmware will report the status of the SD card back to the host. If the SD card is valid, the host will then send an `experiment` structure to the platform, which is validated by the firmware. If `experiment` is valid, the firmware will adjust it to be usable by the firmware, and report the "true" `experiment` back to the host.

Once in host mode, the firmware will enter a host mode idle state await further specialized commands from the host:

Sequence start token

This command from the host instructs the firmware to begin executing a single sequence from the experiment structure. The command token contains a number that identified the sequence to be executed. After the sequence is executed, the firmware

will automatically transmit the sampled data from the sequence to the host. The firmware will then return to the host mode idle state.

Restart

This command from the host indicates that the platform firmware should return to its idle state. The Restart command should be issued both at the beginning of host mode operation, and at the conclusion of a host mode experiment.

Upload experiment data

This command, issued by the host UI, tells the firmware to read the contents of the SD card and transmit it to the host. This is intended to retrieve data stored during standalone operation. If a valid SD card is detected by the firmware, then the `experiment` will first be read from the SD card, and validated. If `experiment` is valid, then the first cluster of the SD card (which contains the `experiment` structure) will be transmitted to the host. The firmware will then use `experiment` to determine how many more clusters to read from the SD card and transmit to the host (this information is also sent to the host, and is used by the host script to parse the incoming data). The firmware will then continuously read the data from the SD card and transmit it to the host.

Chapter 4: Hardware verification and experimental results

Chapter 4 contains discussion on the analysis of data acquired from the relaxometry platform, and how some sequence parameters can be calibrated for optimal SNR. We will also compare the theoretical predictions of transmit power requirements and experimental SNR with empirical measurements. Finally, we will demonstrate four example relaxometry experiments, showing the usefulness of the platform in various applications.

4-1 Data analysis

All NMR experiments performed with the system are based on exponential fitting of the spin echo amplitudes in CPMG readouts. In order to perform such a fit, each echo must be analyzed in a way that describes its overall amplitude or energy with optimal SNR. Since the acquired data is complex, we consider two options for amplitude measurement.

As discussed in chapter 1-3, the large spatial field gradient present during readout effectively maps spatial magnetization in the $\hat{y}$ direction to frequency. Performing the inverse DFT of the acquired echoes gives back the distribution of transverse magnetization as a function of y. For our experiments we assume that the sample properties are uniform in the $\hat{y}$ direction, and therefore we merely need to combine all signal in the bandwidth of interest into one overall amplitude measurement. To accomplish this we considered two methods of analyzing acquired echoes.

Magnitude amplitude measurement

In this method, we first zero pad the sampled echo to increase its length to 100 samples. We then perform the complex DFT of each complex echo, and calculate the magnitude of the DFT. In order to estimate this overall echo amplitude, we window the magnitude into a bandwidth of interest (chosen based on the expected bandwidth of each echo), and average the magnitude within that bandwidth. The average is then taken as the amplitude of the echo.
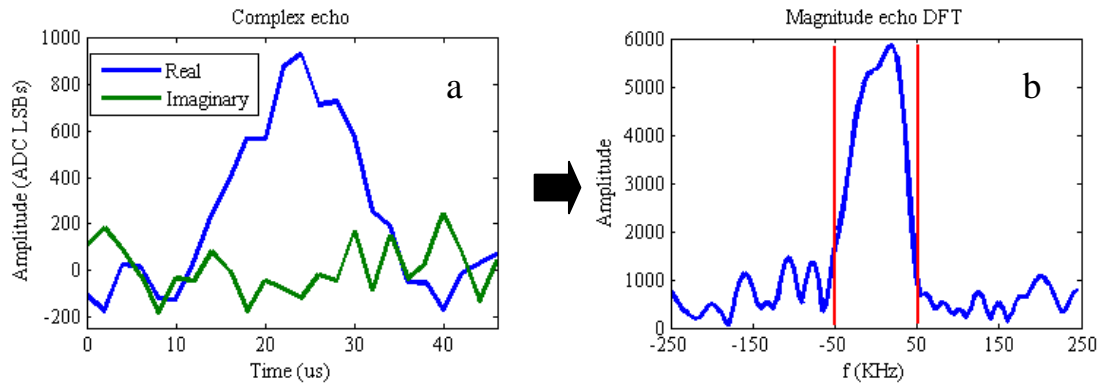
Figure 4-1-1) a) Acquired complex data from a single spin echo. b) DFT magnitude of the acquired echo, after zero padding to N=100. The red lines show the bandwidth of interest in which the magnitude is averaged to give the echo amplitude value.

The advantage of this approach is that it accounts for power contained in both in-phase and quadrature (I and Q) channels, and therefore the LO does not need to be calibrated. Small misalignment of the echoes within the ADC readout also does not affect the results. However, since this is a magnitude measurement, the results will always be positive, and the resulting CPMG decays will always be given a positive offset due to noise power. This is problematic when fitting the CPMG data to exponential decay models, since this can distort the shape of the data and lead to significant errors in the fitting results [36]. This is especially severe when the data has low SNR, but the magnetization has a high dynamic range.

I/Q amplitude measurement

In this method, we again zero pad and perform the complex DFT of each complex echo, but we do not take the magnitude of the DFT. We then window the data to a bandwidth of interest, and take the average of the real or imaginary (I or Q) data within that bandwidth as the echo amplitude.
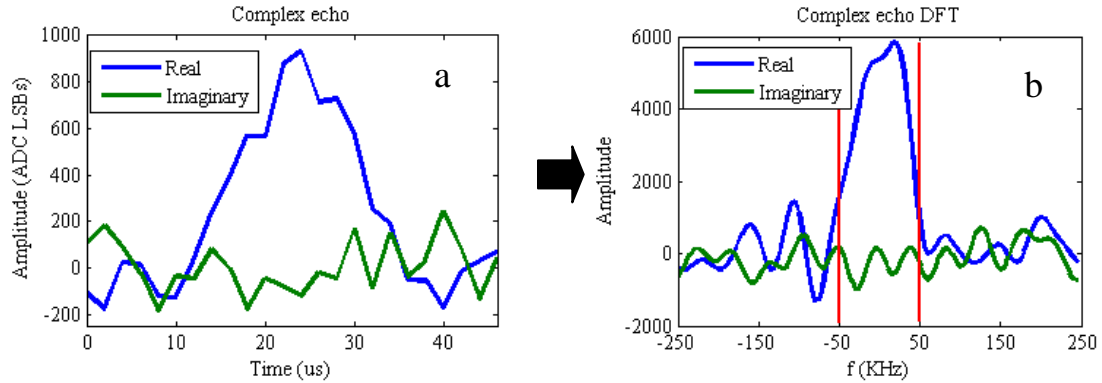
Figure 4-1-2) a) Acquired complex data from a single spin echo. b) Complex DFT of the acquired echo, after zero padding to N=100. The red lines show the bandwidth of interest in which the real part of the DFT is averaged to give the echo amplitude value.

This method has the advantage of being a true amplitude measurement that can be either positive or negative, and is not biased by noise. However, it requires proper calibration of the sequence, or post-hoc corrections to the data. The LO should be tuned such that all the echoes' energy appears on either the I or Q channel. The echo must be centered in the ADC readout in order to avoid modulation of the DFT result. It is also important for all flip angles to be calibrated properly so that all echo pathways in the CPMG have the same phase.

Another major benefit of the I/Q amplitude method is that it inherently has a 3 dB SNR advantage over the magnitude measurement (assuming the LO phase is properly tuned), since only information from either the I or Q channel is used, rather than both.

Because of these benefits, we used the I/Q amplitude method for all subsequent experiments.

Exponential curve fitting

For every sequence in an experiment, all the echoes within that sequence were converted to their equivalent amplitudes, resulting in a series of echo amplitudes. Since all the sampled data in our sequences came from CPMG echo trains, we expected the echo amplitude within each CPMG sequence to follow an exponential decay model similar to equation 3-1-1. In order to extract $M_{xy}(0)$ and T_{2a} from the echo amplitude series, we fit each series to an exponential model in MATLAB. Though the echo amplitudes ideally approach zero as $t \rightarrow \infty$, we have observed that this is not always the case with our acquired data. Small offsets in the measured echo amplitudes sometimes persisted even after applying offset nulling (see section 3-2). Such offsets were only observed with sequences involving high power pulses (>20 W) and short inter-echo spacings (<100 μs). We believe these offsets are the result of disturbances in the DC biasing of the RF amplifier chain due to leakage of the RF pulses through the RXSW.

In order to prevent small DC artifacts from causing errors in the exponential fitting results, we used a three-parameter exponential model including an offset term.

$$M_{xy}(t) = M_{xy}(0)e^{-t/T_{2a}} + Offset \qquad \text{Equation 4-1-1}$$

Where $M_{xy}(0)$ is the fit initial transverse magnetization, T_{2a} is the fit apparent T_2, and *Offset* is the fit offset of the decay. This three-parameter model was used for all experimental results presented in this work.

4-2 System calibration

LO phase calibration

When using I/Q amplitude measurement, the LO phase should be tuned such that all the NMR echo power is in either the I or Q channel. Calibrating the LO is done by first doing a simple CPMG experiment with an arbitrary LO phase. The echo I/Q amplitudes are calculated using the I/Q amplitude measurement described above, and exponential decay fits are done on both the imaginary and real data, yielding an initial magnetization value for each. The fit amplitudes, M_Q and M_I, can be used to find the phase of the NMR signal relative to the LO phase:

$$\theta_{LO-RF} = \arctan\left(M_Q/M_I\right) \quad \text{for} \quad M_I \geq 0 \qquad \text{Equation 4-2-1}$$
$$\theta_{LO-RF} = 180 - \arctan\left(M_Q/M_I\right) \quad \text{for} \quad M_I < 0 \qquad \text{Equation 4-2-2}$$

This correction factor can then be subtracted from the LO phase to bring the echoes into the I channel. This method may also be applied to uncalibrated data post-hoc, by performing the same measurement, and then applying the correction in the form of a twiddle factor to the raw complex data.

It should be noted that the phase of the NMR signal is sensitive to the tuning of the RF coil, especially when the coil has a high quality factor. For experiments where the coil tuning may change over time, maintaining proper LO calibration may not be feasible, and therefore I/Q amplitude measurement may not be robust.

Flip angle calibration

Calibration of the RF pulses should be performed before any experiment, especially when any changes to the hardware, magnet, or coil have been made. We approached flip angle calibration by using a simple CPMG experiment in which the excitation pulse amplitude (controlled by V_D) was varied and the CPMG magnetization

was observed. The properties of the refocusing pulses were approximated to give 180°
flip angles, and were held constant throughout the experiment. The initial magnetization
of each experiment was fit to the model:

$$M_{xy}(\theta) = M_z \sin(\theta)$$
<div align="right">Equation 4-2-3</div>

$$\theta = V_D \cdot k_{B_1} \cdot t$$
<div align="right">Equation 4-2-4</div>

Where t is the RF pulse width, ω_1 is the tip rate in radians per second, and V_D is the TPA
drain voltage. We wished to derive the so-called B_1 coefficient k_{B1}, which can then be
used to calculate the appropriate V_D for the desired flip angles.

Using this approach, we performed an experiment using the surface magnet and
solenoid volume coil to estimate k_{B1}. The experiment was performed using a sample of
de-ionized water.
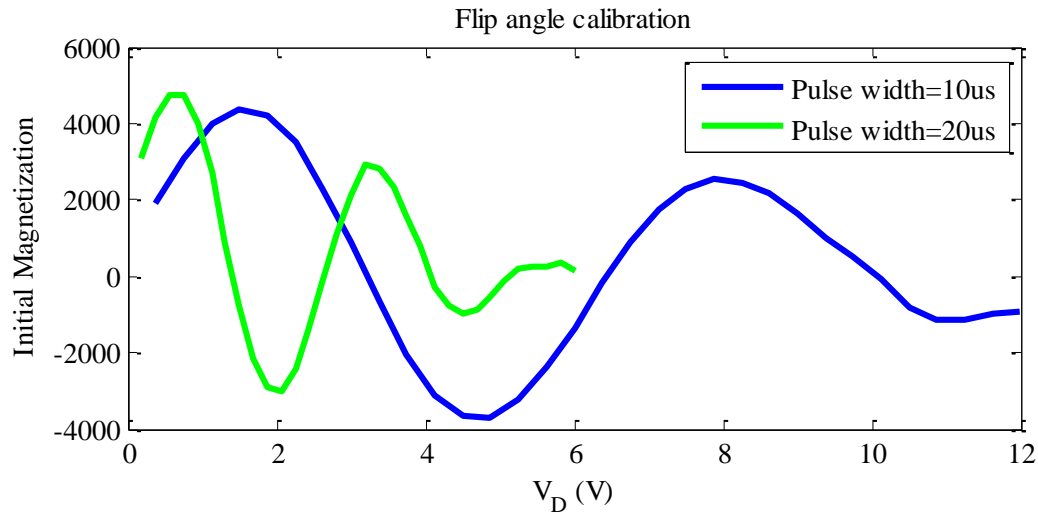
Figure 4-2-1) Results of flip angle calibration experiment for pulse width=10 µs and pulse width=20 µs

It can be seen that the data in figure 4-2-1 corresponds roughly to the expected sinusoidal
shapes, but the functions are not perfectly periodic, and amplitude appears to diminish at
higher flip angles. This can be attributed to B_1 inhomogeneity of the solenoid coil in the
$\hat{z}$ and $\hat{x}$ directions. At higher values of B_1, this causes large flip angle inhomogeneity

that attenuates the overall NMR signal. However, for flip angles up to 180° the model fits well and is sufficient for calibration.

It should be noticed that the flip angle θ is not necessarily proportional to pulse duration. This is especially true for short pulses that approach or exceed the effective bandwidth of the TPA and RF coil. For this reason, it is wise to perform the flip angle calibration with the same pulse width as required by the desired experiment.

4-3 System performance verification

Transmit chain verification

We can use the above flip angle calibration data to calculate the B_1 efficiency of the system, and compare it to the theoretical B_1 efficiency of the solenoid coil. Recall that the coil had an ESR of 0.95 Ω, and a simulated B_1 efficiency of 988 µT/A. For a 20 µs RF pulse with a FA of 180°, a B_1 of 1.176 mT is required (recalling that the solenoid coil generates a linearly polarized field, and thus requires twice as much B_1 as a circularly polarized field [11]). Therefore the required power of the RF pulse is expected to be 0.647 W. Our calibration experiment (figure 4-1-2) shows that a 180° flip angle is realized with V_D=1.406 V. Using the data of the data of TPA output power vs. V_D (figure 2-4-5) predicts the output power to be 0.7222 W. The measured loss of the TXSW (-0.4 dB at 8.35 MHz, see figure 2-3-4) lowers the output power at the coil port to be 0.659 W, which is very close to the theoretical value predicted above. The small difference can be explained by cable losses and measurement error.

System noise performance

The ability of the hardware to sample the NMR signal with optimal SNR is of great importance to any NMR system. To determine the noise performance of the system, we performed a simple NMR experiment and compared the SNR of the acquired data to the theoretical SNR of for that experiment.

For this experiment we again used the 196.1 mT surface magnet and the solenoid volume coil (see table 2-2-2) with a sample of deionized water. This sequence was designed to provide a simple CPMG readout with a 90° excitation pulse and 180° refocusing pulses. All RF pulses had an estimated bandwidth of 100 KHz. The flip angles were calibrated beforehand using the methodology described above. The LO phase was also calibrated so that all of the echo signals were real in value. A detailed description of the experiment parameters is given in appendix A.

By using the methodology in [12] , we calculated that for a perfect excitation and refocusing of the magnetization M_0, the initial magnetization M_{xy} of the echo train should be 1.79×10^{-11} A m^2, giving an induced voltage of 9.28×10^{-7} V peak in the coil. The noise voltage density of the coil will be 0.125 nV/$\sqrt{\text{Hz}}$. For a bandwidth of 100 KHz, this gives a theoretical SNR of 23.48, or 27.41 dB. It is assumed that both the sample and coil are at ambient temperature (measured at 295.6 K).

To measure experimental SNR, we performed the sequence sixteen times. The TR of each repetition was set to TR=30 s to ensure that M_z relaxes very close to its steady state value of M_0 (within a few ppm). Each echo of each repetition was evaluated using the real amplitude measurement method described above, with a measurement bandwidth of 100 KHz. We then used the amplitudes of the CPMG echoes in the three-parameter

exponential decay fit in order to determine the initial signal M_{xy}. The power of the noise is determined by subtracting the fit signal from the raw echo amplitude values, leaving an error signal. The ratio between the fit initial signal M_{xy} and the standard deviation (σ) of the error signal is the signal to noise ratio.
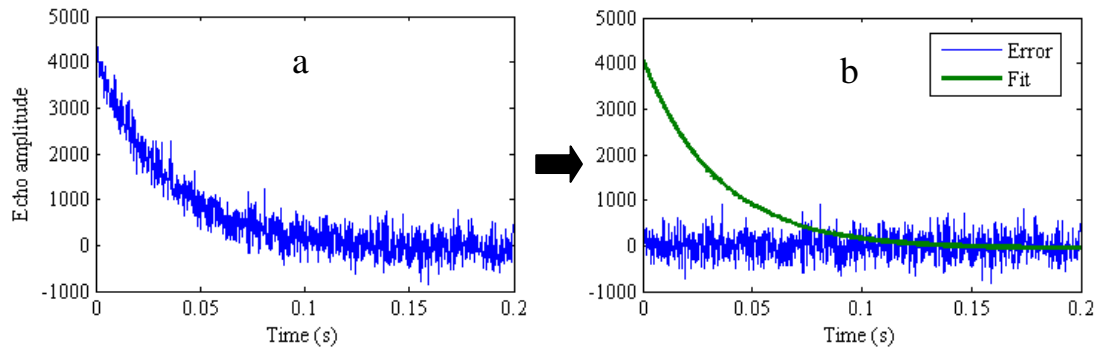
Figure 4-3-1) a) Measured echo amplitude for the above CPMG sequence. b) exponential fit and error signal of the CPMG echoes.

Our experiments yielded an average measured SNR of 15.03 (standard deviation of 0.3), or 23.54 dB per repetition. It was expected that the experimental SNR would be lower than theoretical SNR by at least the NF of the RF chain (3.09 dB at 8.35 MHz), and therefore we adjusted our theoretical SNR down to 24.32 dB. The actual experimental SNR was lower than the theoretical SNR by 0.78 dB (after accounting for the NF of the receive chain). This discrepancy may due to a variety of factors, including loss in the coil matching network and cable, B_1 inhomogeneities, or external interference.

We examined the variation of the exponential decay fits of each repetition. We performed fits on all 16 repetitions, and the results are presented in table 4-3-1 below:

	Mean	σ	SNR
Initial magnetization	4133.2	53.46	77.31
T_{2a} (ms)	34.30	0.768	44.66
Offset	-86.5	39.9	2.17

Table 4-3-1) Results of a single shot experiment for SNR measurement

Here we see that the SNR of the exponential fit results is much higher than the signal

SNR, due to the large number of echoes per repetition. The SNR of the fits can be further

improved by increasing the number of echoes (by decreasing the TE of the CPMG).

Further improvements to SNR can be gained by averaging the data from multiple

repetitions of the same experiment, though this extends the time required for the

experiment. Ultimately what is desired is the best SNR efficiency, measured in SNR per

unit time squared. SNR efficiency is a function of the sequence TR, the length of the

sequence T_{CPMG}, and the sample T_1. In practice, the T_1 of the sample should be measured

or estimated before attempting a long experiment, and the TR of the experiment adjusted

to give optimal SNR efficiency. Assuming that the longitudinal magnetization is

completely spoiled by the CPMG refocusing pulses, the optimum SNR efficiency can be

found by solving equation 4-3-1 for TR:

$$\ln\left(\frac{T_1}{2TR+T_1}\right) = -\left(\frac{T_{cpmg}-TR}{T1}\right)$$
<div align="right">Equation 4-3-1</div>

For experiments in which T_{CPMG} is much less than TR, equation 4-3-1 reduces to:

$$TR_{opt} \approx 1.256 \times T_1$$
<div align="right">Equation 4-3-2</div>

4-4 Example application: measurement of G_0 by diffusion weighted experiment

The quantitative measurement of a sample's self-diffusion coefficient D requires

an accurate measure of the static gradient in the sensitive volume. In order to verify our

previous measurement of the magnet's G_0, we performed a diffusion weighted experiment

on samples with known D, and used the results as an alternative measurement of G_0. For

this experiment we used the constant relaxation diffusion preparation sequence described

in chapter 3-1. Three samples with known D were chosen: deionized (DI) water, acetone

and glycerol [37]. Each sample was measured four times in order to estimate the error in the measurements. The details of the experiments can be viewed in appendix A. The results for the experiments are displayed in figures 4-4-1 a-c, and in table 4-4-1.
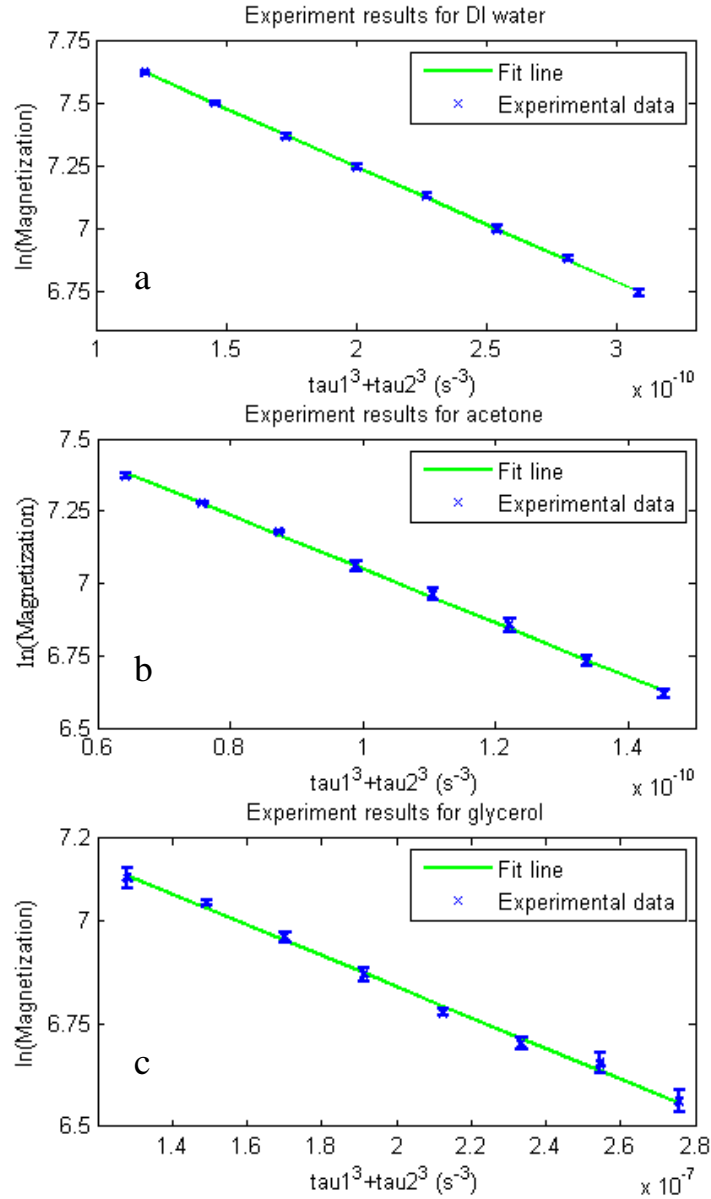
Figure 4-4-1 a) Constant relaxation diffusion experiment results for a) DI water, b) acetone, and c) glycerol

The calculated G_0 from the DI water and acetone experiments show good agreement with the previously measured value of G_0 at $B_0 = 196.1$ mT of 6.52 T/m. The most likely explanation for the significant difference in the glycerol experiment is a

larger temperature coefficient of D than for the other samples. The experiments were conducted at ambient temperature (typically 22.4C°), so the literature values for D given in table 4-4-1 will not be the actual values in our experiment.

Sample	D at 25C° (m^2/s) [37]	Mean G_0 (T/m)	σ
DI water	2.299e-9	6.4589	0.0402
Acetone	4.57e-9	6.5497	0.0235
Glycerol	2.2e-12	5.9646	0.0573

Table 4-4-1) Results of self diffusion coefficient measurement for three samples

4-5 Example application: Spoiling of milk

NMR relaxometry has been used in quality control of food products extensively. Here we observe the dependence of NMR relaxation on the shelf age of two samples of pasteurized milk (0% fat free and 8% whole milk). We prepared five pairs of milk samples, each with one fat free (0% fat) and one whole milk (8% fat) in sealed glass vials. Initially, four of the sample pairs were refrigerated, while the fifth was stored at room temperature. After each passing day, one more pair of samples was removed from the refrigerator and stored at room temperature. This was continued until the fifth day, resulting in samples of both fat free and whole milk with room temperature storage times of between zero and four days. On the fifth day, we performed a set of measurements on every sample. The measurements included an inversion recovery experiment to measure T1 (TI=50-3000 ms), and a variable TE CPMG (t=40-100 μs) experiment to estimate T_2 and D. The detailed parameters of these experiments can be found in appendix A. The experiments were performed using the solenoid volume coil.

After the measurements were performed and the results observed, we decided to extend the experiment for one more day. On the sixth day, the "oldest" sample was again measured and the results added to the trends. The results of all the experiments are shown

below. Errors in the measurements were estimated by performing each measurement on one milk sample four times and calculating the standard deviation of the results.
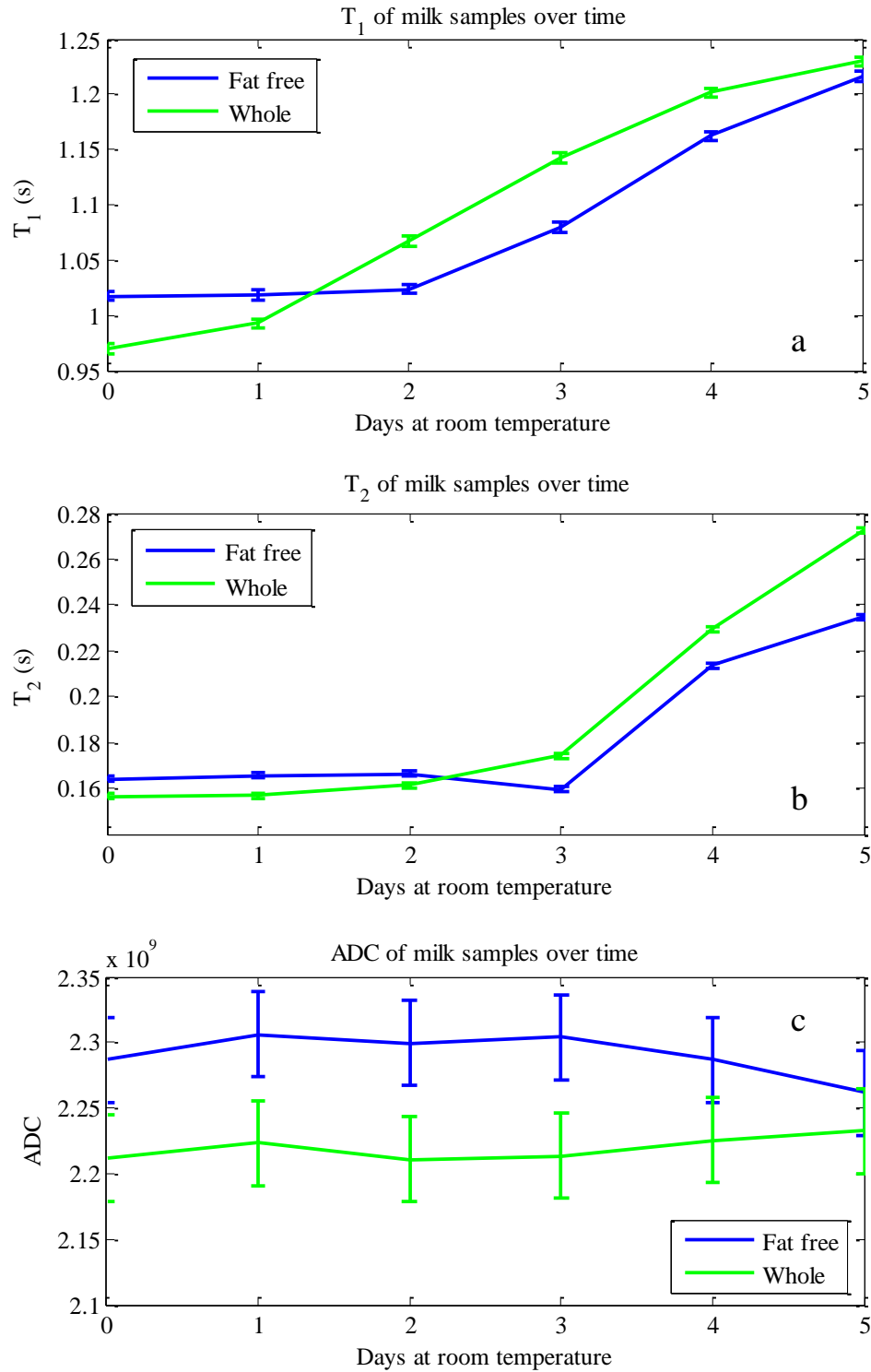
Figures 4-5-1 a-c) Plots of experimental results for the fat free and whole milk samples with different room-temperature storage times.

The results show very significant trends in T_1 (figure 4-5-1 a) and T_2 (figure 4-5-1 b) for both types of milk. There was no statistically significant trend for ADC in either sample (figure 4-5-1 c). We hypothesize that these trends are due the lipids and various proteins in the milk coming out of emulsion and aggregating on the inside of the sample container, leaving a water-based fluid with longer overall relaxation times.

4-6 Example application: Curing of adhesives

Investigation of adhesives using surface NMR scanners has been proposed in previous publications [3]. Here we demonstrated the use of the system for detecting the process of setting and curing in common adhesives. Because the object to which the adhesive will be applied will often be much larger than the volume of interest for the magnet, we used a spiral surface coil for these experiments.

Our first adhesive sample was J-B mini epoxy from J-B Weld company. Epoxy adhesives are composed of two separate chemicals, a compound and a hardener, which are combined upon use. The compound is composed of short polymer chains called monomers, with epoxide groups at each end. The hardener is also a monomer chain with two or more amine sites. Normally the monomers are allowed to tumble isotropically, leading to weak dipolar interaction and a relatively long T_2. When the compound and hardener are combined, the epoxides of the compound monomer react with the amine sites of the hardener monomer to form covalent bonds. This creates a densely crosslinked polymer to form, which becomes stiff and strong. This crosslinking also decreases the freedom of the monomers to tumble, and causes their motion to be anisotropic, leading to

increased dipolar interaction and a lower T_2. Because of this phenomenon, the process of epoxy hardening and curing can be measured via NMR relaxometry.

For this experiment we applied a layer of J-B mini epoxy to a small piece of FR4 fiberglass (1.62 mm thick), and placed it on the surface coil, adhesive side facing up. The thickness of the FR4 was such that the epoxy occupied the sensitive volume of the magnet and coil at 8.35 MHz. A simple CPMG sequence was used with phase cycling to measure T_2. The detailed sequence parameters are given in appendix A.
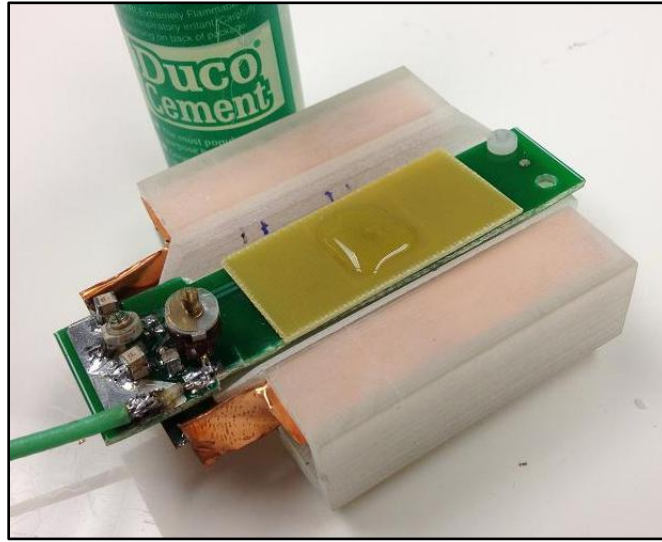
Figure 4-6-1) Photo of experimental setup for measuring curing of adhesives. The adhesive (Duco Cement in this photo) is applied to a small sheet of FR4, which is set on top of the surface coil.

To operate with such a short TR, standalone operation was used. The experiment was repeated 1800 times, for a total time of one half hour. The raw data was then imported into MATLAB where it was analyzed. Groups of 30 experiments were averaged together, giving an overall measurement time of 30 seconds per point. Details of the experiment can be found in appendix A. Exponential fitting was performed on each average, giving its initial magnetization and T_2. The results are plotted below in figure 4-6-2.
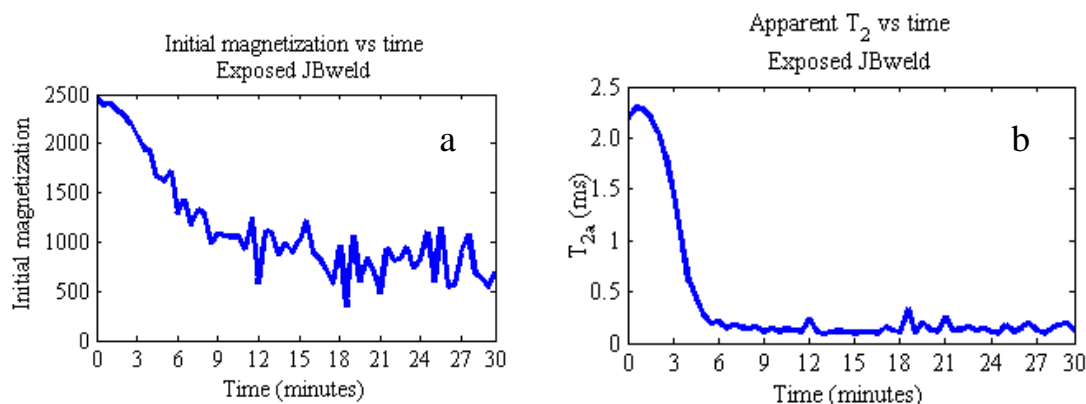
Figure 4-6-2) Plots of a) initial magnetization and b) apparent T_2 for JBweld epoxy

As expected, the apparent T_2 drops off sharply as the epoxy sets. The initial magnetization also decreases significantly over time. This is most likely due to changes in the contributions of different bound and unbound spin populations in the setting epoxy. As the epoxy sets, the T_2 of some of the spins will decrease far below what the system is capable of measuring with TE=60 μs. This results in a decrease in overall apparent magnetization in the CPMG. The apparent T_2 of the sample reaches a steady state approximately 300 seconds from the start of the experiment, which is in agreement with the advertised setting time of five minutes. Presumably the T_2 of the adhesive continues to slowly drop further during the curing process (which can span many hours), but this trend is likely not detectable with the above sequence parameters and analysis techniques.

We also performed a similar experiment to observe the drying of Duco Cement (from ITW Devcon). Unlike an epoxy, Duco Cement is a polymer-solvent solution. As the cement sets, the solvent evaporates, leaving behind the polymer chains which begin to crosslink and harden. The evaporation of the solvent reduces the overall ^{1}H abundance in the sample. Therefore we expect to see a decrease in both overall magnetization and T_2 as the cement sets.

We first performed an experiment in which a layer of cement was applied to the top of a piece of fiberglass, similar to the epoxy experiment. The cement was allowed to dry while exposed to the air. It was initially determined that the wet Duco Cement has a much longer T_2 than the J-B mini epoxy, and thus we chose a longer TR of 3 seconds, and operated the experiment in host mode. The sequence used was a simple phase cycling CPMG with $\tau=50$ µs, TR=3 seconds, and Nexperiments=8. This experiment was performed 18 times every two minutes, for a total experiment time of 36 minutes. Details of the experiment can be found in appendix A. For each measurement the initial magnetization and apparent T_2 were derived by exponential fitting. The results are shown below:
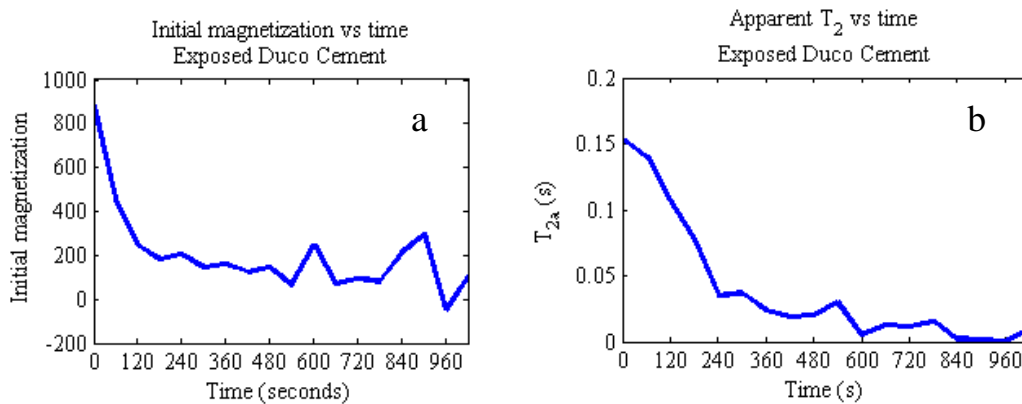
Figure 4-6-3) Plots of a) initial magnetization and b) apparent T_2 for exposed Duco Cement

The two plots clearly show the transition from the setting phase and the curing phase. During the setting phase, the evaporation of the solvent is evident by the rapid drop in magnetization and T_2. At around 200 seconds, the solvent has mostly finished evaporating, and only the polymer remains. In the curing phase, polymerization slowly occurs, and the T_2 continues to drop.

We also performed an experiment with Duco Cement in which a thick layer of cement was applied to a fiberglass piece, and another piece of fiberglass was placed on

top of the cement. Care was taken not to press the two pieces together, so that a generous thickness of cement still remained in between them. We used a similar sequence to that described above with a total duration of six hours. Details of the experiment can be found in appendix A.
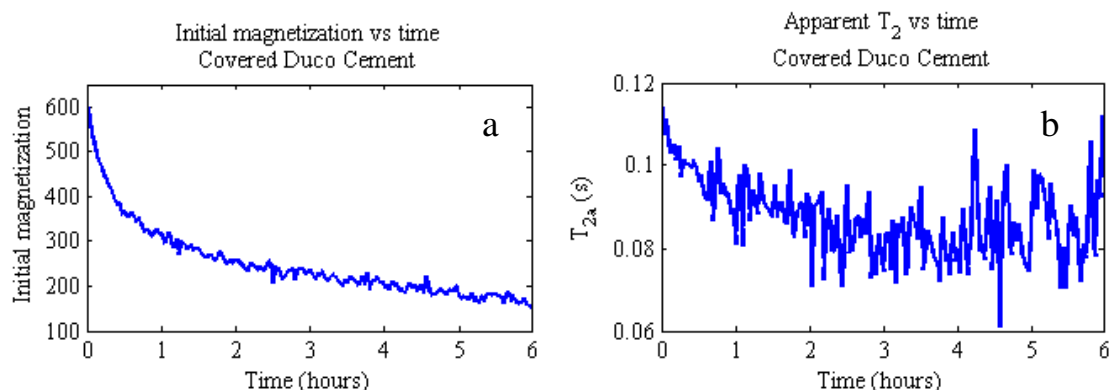
Figure 4-6-4) Plots of a) initial magnetization and b) apparent T_2 for Duco Cement in between two fiberglass layers

The results differed greatly from those seen in the exposed-cement experiment. The magnetization initially drops quickly, but the rate of loss drops after about an hour. The magnetization continues to gradually decline for the remainder of the experiment. The T_2 also has an initial drop in the first couple of hours, but reaches a relatively steady state. The overall change in T_2 for this experiment is far less than that seen in the exposed cement.

The trends suggest that the setting process is greatly slowed by the fiberglass cover, which drastically lowers the cement's exposure to air. Only a small amount of the cement is exposed to the air, leading to a diffusion gradient for the solvent from the center of the cement slice towards the edge. Therefore the distribution of solvent in the cement will change over time, and so will the rate of polymerization. Initially, the outer edge of the cement layer, which is in contact with air, will dry quickly leading to the

initial fast drop in magnetization and T_2. Once the outer cement is relatively dry, the solvent from the inner cement will begin diffusing towards the edges, leading to an overall slower setting process. The plots show that even after six hours, solvent is still evaporating, and polymerization has not occurred in most of the cement.

Upon close examination of the CPMG echo decays, it could be seen that the decays appeared to not be monoexponential, but rather were a superposition of two or more exponential decays. This supported our theory of a heterogeneous setting process. Use of a biexponential fitting model may allow more insight into the nature of the setting process.

4-7 Surface probe for biosensor applications

We also desired to see the performance of the system when used in a configuration that does not require a shielded enclosure for the NMR probe, and may be used on a very large SUT. For this experiment we used the screened surface scanning probe described in section 2-2, and performed several simple CPMG experiments to determine the sensitivity of this probe. The sequence for each experiment was a simple CPMG calibrated to give maximum signal with 16 μs pulse widths. Phase cycling was used, and two repetitions of the sequence were averaged together (for a total of four individual CPMG sequences). Detailed experiment parameters can be viewed in appendix A. This experiment was first performed with the surface scanner inside the shielded enclosure, using a phantom made of saline in a rubber balloon, set on the probe surface. Second we performed the experiment outside of the shielded enclosure, with the same phantom. Finally, we performed the experiment outside of the enclosure and used the

Author's bare hand as the SUT. The results of the of the three experiments are shown

below:

Experiment	Signal (N=4)	Noise (N=4)	SNR (N=4)	SNR (N=1)
Saline, inside enclosure	1595	328.3	4.860	2.430
Saline, no enclosure	1562	391.3	3.991	1.996
Skin, no enclosure	2066	577.3	3.579	1.789

Table 4-7-1) Changing sensitivity and noise for the surface probe under different conditions.

The results show that taking the probe out of the shield increased the noise level slightly,

likely due to the increased ambient interference. When the phantom was replaced with a

human SUT, the noise floor increased substantially due to the Author's entire body

coupling additional interference into the probe. The signal level also increased

substantially, which was likely due to a better filling factor with the Author's hand versus

the balloon phantom. Overall, the decrease in SNR between a shielded phantom

experiment and the unshielded in vivo experiment was 2.7 dB.

This short demonstration shows that by properly designing the NMR probe, the

platform can be used without the need for large shielded enclosures, and can even be used

for in vivo biosensor applications in human subjects.

Chapter 5: Conclusions and future directions

We have presented the design and operation of a hardware platform for performing NMR relaxometry experiments. The platform is capable of executing a wide variety of relaxometry experiments with a wide variety of magnet and coil combinations. Experiments can be performed while connected to a PC host, or in a standalone mode. The platform can also be powered from a battery pack, allowing experiments to be performed for mobile and even wearable applications. The platform also operates over a frequency range of 5-80 MHz, with the only components requiring tuning being the TPA and the RF coil. The platform uses almost entirely off-the-shelf components and is estimated to cost less than $750. The hardware and firmware is open source [1], allowing anyone with the proper materials and skills to replicate our results. Table 5-1 below shows the general specifications of the platform.

Parameter	Min	Typical	Max	Units
Frequency range of RF chain	5	-	80	MHz
Noise figure	2.5	3.0	4.2	dB
IP1$_{dB}$	-93.15	-	-47.15	dB
Maximum echo bandwidth	-	-	500	KHz
Dead time	-	20	-	μs
Average data throughput	-	-	250	ksps
Supply voltage rage	12	-	18	VDC
Idle power consumption	2.5	-	3	W
Platform dimensions	239L x 157W x 46H			mm
Platform weight	3.0			lbs.

Table 5-1) Overall specifications of the NMR relaxometry platform

Our motivation for the development of the relaxometry platform was to promote NMR relaxometry in new applications that were previously inaccessible to NMR due to constraints on cost, size, or complexity. In particular we hope that the platform will provide a basis for portable NMR-based biosensors, which could potentially provide a new means of non-invasive analysis of patient physiology.

While the platform is already suitable for a wide variety of NMR applications, there is still a great deal of room for optimization in the platform hardware and firmware, especially with regards to in-vivo biosensor applications. The following list contains many possibilities for improving the platform's flexibility, performance, and robustness:

- Improvements in the RF front end, especially the TRSW and RF receive chain, would allow for higher pulse power and faster recovery time, which would yield higher SNR data with less baseband artifacts.

- Optimization of the magnet and coil design for biosensor applications.

- Extending the frequency of operation for the system to lower frequency ranges, allowing for use with smaller magnets and greater penetration depths.

- Drastically reducing size and weight through use of more integrated layout and more lightweight batteries, making the platform even more attractive for mobile applications.

- Utilize a 4-bit SD interface to the SD card, increasing its maximum data rate and robustness

- Addition of a gradient system, allowing for true imaging applications.

- More powerful processor for standalone analysis of sampled data.

Appendix A: Selected experiment parameters

SNR measurement experiment

`experiment`

Nsequences	1
TXrise	10.54
Noffsetsamples	100
dt_offsetsamples	10
Nexperiments	16
Vgain	1.875

`experiment.sequence[1]`

f0	8350000
Npreppulses	1
echofirst	0
TR	30

`experiment.sequence[1].preppulse[1]`

tau	100
puslewidth	10
pulsephase	0
pulseamp	512
Vd	525

`experiment.sequence[1].CPMG`

tau	100
pulsewidth	10
pulsephase	90
pulseamp	512
Vd	1050
LOphase	228.9
LOamp	1023
Nsamp	24
Nechoes	1000
dt	2
sampoffset	5

Constant relaxation diffusion measurement (DI water)

Phase cycling was performed by repeating this experiment with

`preppulse[1].pulsephase` alternating between 0 and 180.

```
experiment:
```

Nsequences	8
TXrise	5
Noffsetsamples	100
dt_offsetsamples	10
Nexperiments	8
Vgain	1.875

```
experiment.sequence[1]
```

f0	8350000
Npreppulses	3
echofirst	1
TR	5

```
experiment.sequence[1].preppulse[1]
```

tau	450
puslewidth	10
pulsephase	0
pulseamp	512
Vd	550

```
experiment.sequence[1].preppulse[2]
```

tau	750
puslewidth	10
pulsephase	90
pulseamp	512
Vd	1210

```
experiment.sequence[1].preppulse[3]
```

tau	300
puslewidth	10
pulsephase	90
pulseamp	512
Vd	1210

```
experiment.sequence[1].CPMG
```

tau	50
pulsewidth	10
pulsephase	90
pulseamp	512
Vd	1210
LOphase	236.4
LOamp	1023
Nsamp	16
Nechoes	7500
dt	1.7
sampoffset	5

All sequences are identical except for the tau of their preparation pulses

```
(preppulse[])
```

	preppulse[1].tau	preppulse[2].tau	preppulse[3].tau
sequence[1]	450.00	750	300.00
sequence[2]	507.96	750	242.04
sequence[3]	547.43	750	202.57
sequence[4]	579.42	750	170.58
sequence[5]	607.03	750	142.97
sequence[6]	631.70	750	118.3
sequence[7]	654.19	750	95.81
sequence[8]	675.00	750	75.00

Constant relaxation diffusion measurement (acetone)

All sequence parameters for acetone are identical to the DI water experiment, except for

the `tau` of their preparation pulses (`preppulse[]`):

	preppulse[1].tau	preppulse[2].tau	preppulse[3].tau
sequence[1]	375.00	600	225.00
sequence[2]	409.79	600	190.21
sequence[3]	435.95	600	164.05
sequence[4]	457.83	600	142.17
sequence[5]	477.03	600	122.97
sequence[6]	494.34	600	105.66
sequence[7]	510.23	600	89.77
sequence[8]	525.00	600	75.00

Constant relaxation diffusion measurement (glycerol)

All sequence parameters for glycerol are identical to the DI water experiment, except for

the `tau` of their preparation pulses (`preppulse[]`)::

	preppulse[1].tau	preppulse[2].tau	preppulse[3].tau
sequence[1]	4750.0	7500	2750.0
sequence[2]	5141.9	7500	2358.1
sequence[3]	5445.6	7500	2054.4
sequence[4]	5702.6	7500	1797.4
sequence[5]	5929.4	7500	1570.4
sequence[6]	6134.8	7500	1365.2
sequence[7]	6323.9	7500	1176.1
sequence[8]	6500.0	7500	1000.0

Inversion recovery experiment for milk

Phase cycling was performed by repeating this experiment with

`preppulse[1].pulsephase` alternating between 0 and 180.

`experiment`

Nsequences	8
TXrise	5
Noffsetsamples	100
dt_offsetsamples	10
Nexperiments	4
Vgain	1.875

`experiment.sequence[1]`

f0	8350000
Npreppulses	2
echofirst	0
TR	10

`experiment.sequence[1].preppulse[1]`

tau	20000
puslewidth	10
pulsephase	0
pulseamp	512
Vd	1200

`experiment.sequence[1].preppulse[2]`

tau	50
puslewidth	10
pulsephase	0
pulseamp	512
Vd	550

`experiment.sequence[1].cpmg`

tau	50
pulsewidth	10
pulsephase	90
pulseamp	512
Vd	1200
LOphase	230.4
LOamp	1023
Nsamp	16
Nechoes	7500
dt	1.7
sampoffset	5

All sequences are identical except for the `tau` of `preppulse[1]`

	preppulse[1].tau
sequence[1]	20000
sequence[2]	445710
sequence[3]	871430
sequence[4]	1297100
sequence[5]	1722900
sequence[6]	2148600
sequence[7]	2574300
sequence[8]	3000000

Variable TE CPMG experiment for milk

Phase cycling was performed by repeating this experiment with `preppulse[1].pulsephase` alternating between 0 and 180.

`experiment`

Nsequences	8
TXrise	5
Noffsetsamples	100
dt_offsetsamples	10
Nexperiments	4
Vgain	1.875

`experiment.sequence[1]`

f0	8350000
Npreppulses	1
echofirst	0
TR	10

`experiment.sequence[1].preppulse[1]`

tau	40
puslewidth	10
pulsephase	0
pulseamp	512
Vd	550

`experiment.sequence[1].cpmg`

tau	40
pulsewidth	10
pulsephase	90
pulseamp	512
Vd	1100
LOphase	229
LOamp	1023
Nsamp	16
Nechoes	9375
dt	1.7
sampoffset	5

All sequences are identical except for the `tau` of `preppulse[1]` and the `tau` and

`Nechoes` of `cpmg`

	preppulse[1].tau	cpmg.tau	cpmg.Nechoes
sequence[1]	40.00	40.00	9375
sequence[2]	52.92	52.92	7087
sequence[3]	63.25	63.25	5929
sequence[4]	72.11	72.11	5200
sequence[5]	80.00	80.00	4688
sequence[6]	87.18	87.18	4302
sequence[7]	93.81	93.81	3998
sequence[8]	100.00	100.00	3750

Simple CPMG experiment for JBweld

Phase cycling was performed by using two sequences in each experiment.

`sequence[2]` was identical to `sequence[1]`, except that

`sequence[2].preppulse[1].pulsephase` was equal to 180.

`experiment`

Nsequences	2
TXrise	4
Noffsetsamples	100
dt_offsetsamples	75
Nexperiments	1800
Vgain	1.875

`experiment.sequence[1]`

f0	8350000
Npreppulses	1
echofirst	0
TR	0.5

`experiment.sequence[1].preppulse[1]`

tau	30
puslewidth	6
pulsephase	0
pulseamp	512
Vd	1350

```
experiment.sequence[1].cpmg
```

tau	30
pulsewidth	6
pulsephase	90
pulseamp	512
Vd	2700
LOphase	216.10
LOamp	1023
Nsamp	12
Nechoes	300
dt	1.7
sampoffset	4.533

Simple CPMG experiment for Exposed Duco Cement

Phase cycling was performed by repeating this experiment with

`preppulse[1].pulsephase` alternating between 0 and 180.

```
experiment
```

Nsequences	1
TXrise	4
Noffsetsamples	100
dt_offsetsamples	75
Nexperiments	8
Vgain	1.875

```
experiment.sequence[1]
```

f0	8350000
Npreppulses	1
echofirst	0
TR	3

```
experiment.sequence[1].preppulse[1]
```

tau	50
puslewidth	6
pulsephase	0
pulseamp	512
Vd	1300

```
experiment.sequence[1].CPMG
```

tau	50
pulsewidth	6
pulsephase	90
pulseamp	512
Vd	2600
LOphase	240.095

LOamp	1023
Nsamp	16
Nechoes	5000
dt	1.7
sampoffset	4.533

Simple CPMG experiment for covered Duco Cement

Phase cycling was performed by repeating this experiment with

`preppulse[1].pulsephase` alternating between 0 and 180.

`experiment`

Nsequences	1
TXrise	4
Noffsetsamples	100
dt_offsetsamples	10
Nexperiments	10
Vgain	1.875

`experiment.sequence[1]`

f0	8350000
Npreppulses	1
echofirst	0
TR	5

`experiment.sequence[1].preppulse[1]`

tau	50
puslewidth	6
pulsephase	0
pulseamp	512
Vd	1350

`experiment.sequence[1].CPMG`

tau	50
pulsewidth	6
pulsephase	90
pulseamp	512
Vd	2700
LOphase	216.1
LOamp	1023
Nsamp	16
Nechoes	7500
dt	1.7
sampoffset	4.5

Simple CPMG experiment for surface probe sensitivity measurement

Phase cycling was performed by repeating this experiment with

`preppulse[1].pulsephase` alternating between 0 and 180.

`experiment:`

Nsequences	1
TXrise	10.54
Noffsetsamples	100
dt_offsetsamples	10
Nexperiments	16
Vgain	1.875

`experiment.sequence[1]`

f0	8350000
Npreppulses	1
echofirst	0
TR	3

`experiment.sequence[1].preppulse[1]`

tau	50
puslewidth	16
pulsephase	0
pulseamp	512
Vd	1900

`experiment.sequence[1].cpmg`

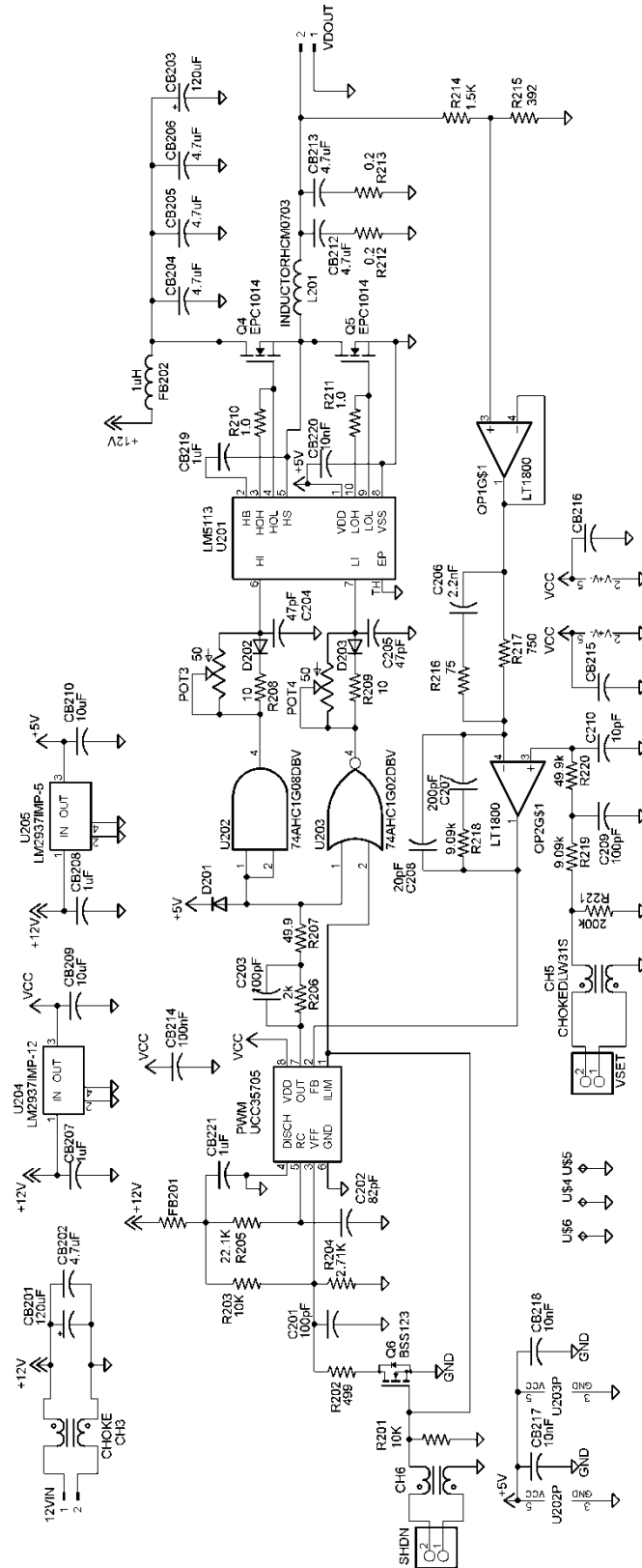| tau	50
pulsewidth	16
pulsephase	90
pulseamp	512
Vd	3800
LOphase	110
LOamp	1023
Nsamp	20
Nechoes	3000
dt	2
sampoffset	3

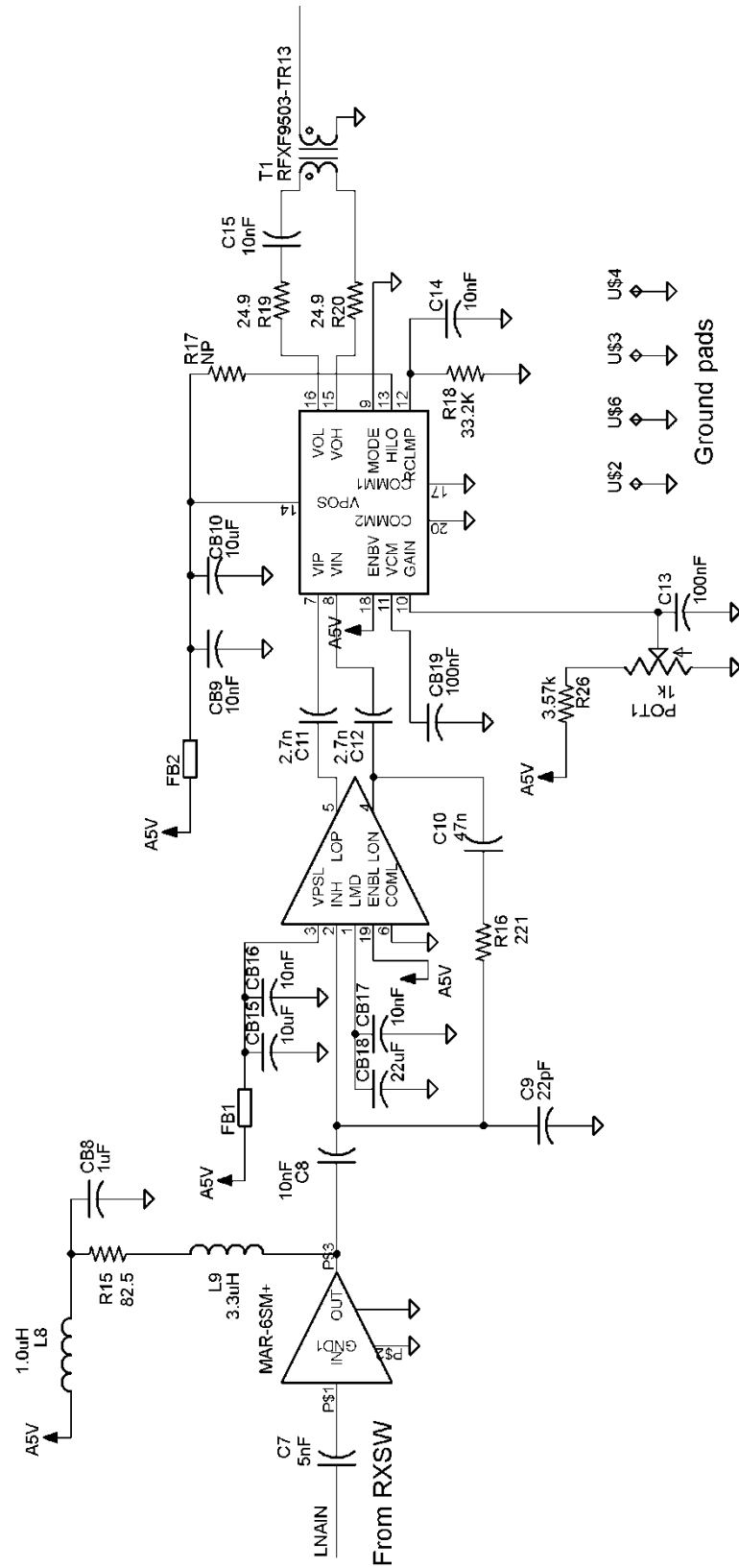# Appendix B: Circuit schematic diagrams

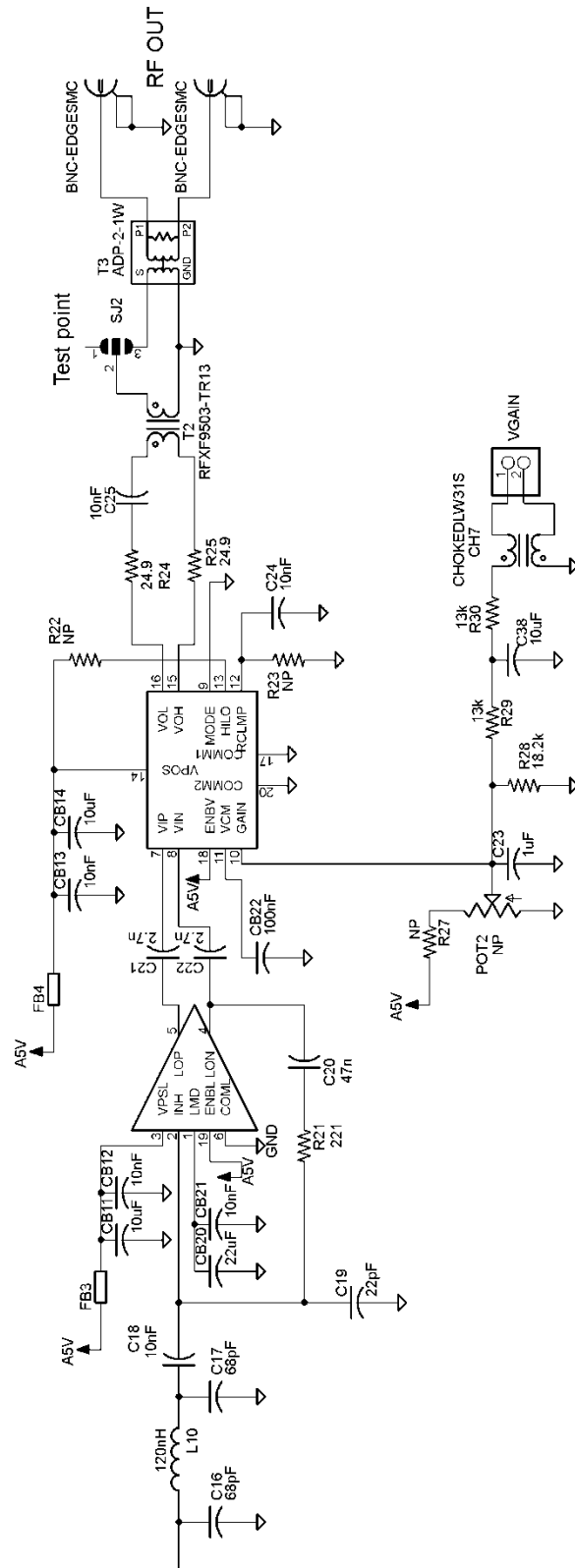## TRSW schematic
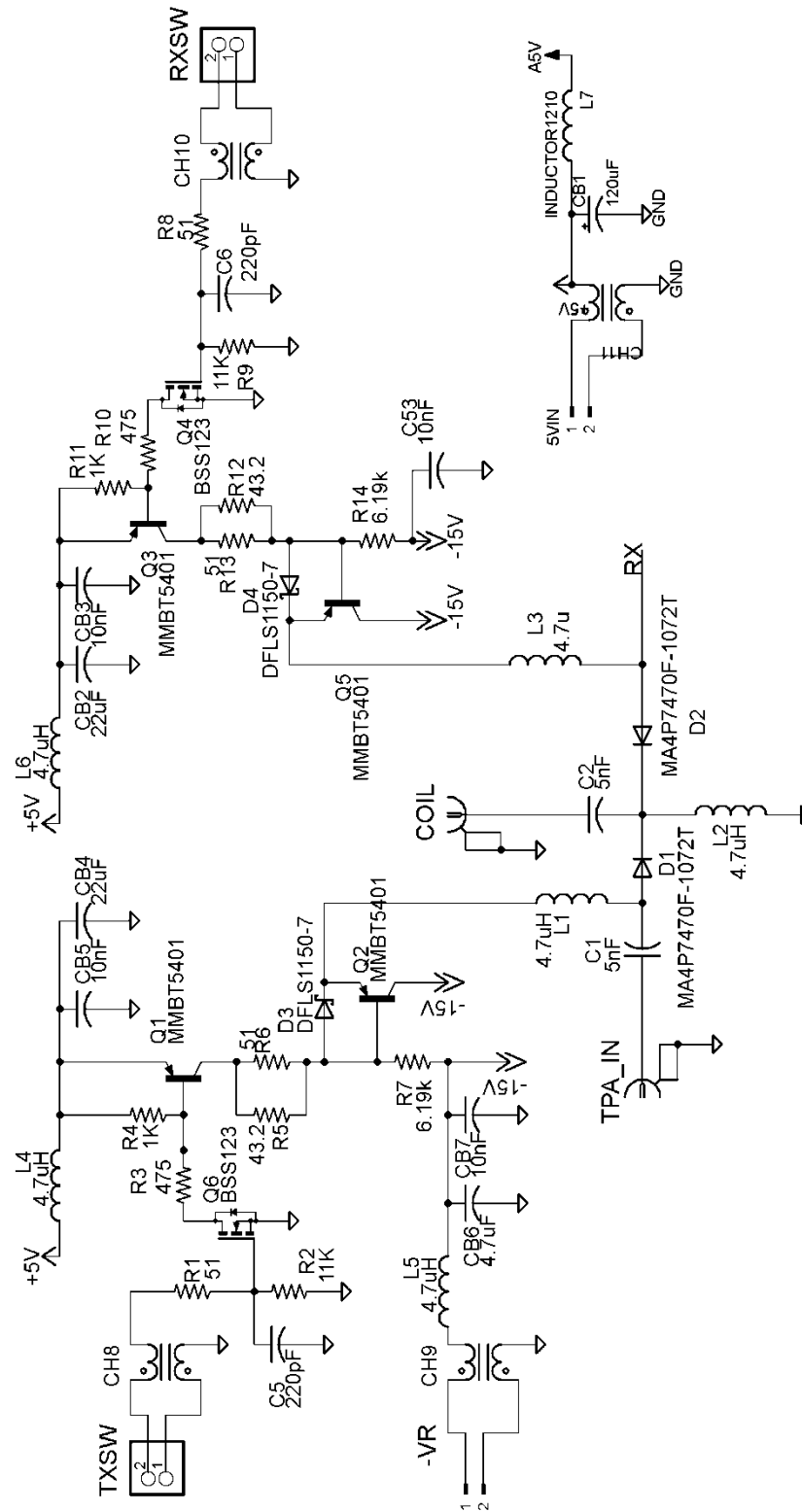
8.35MHz CMCD TPA schematic
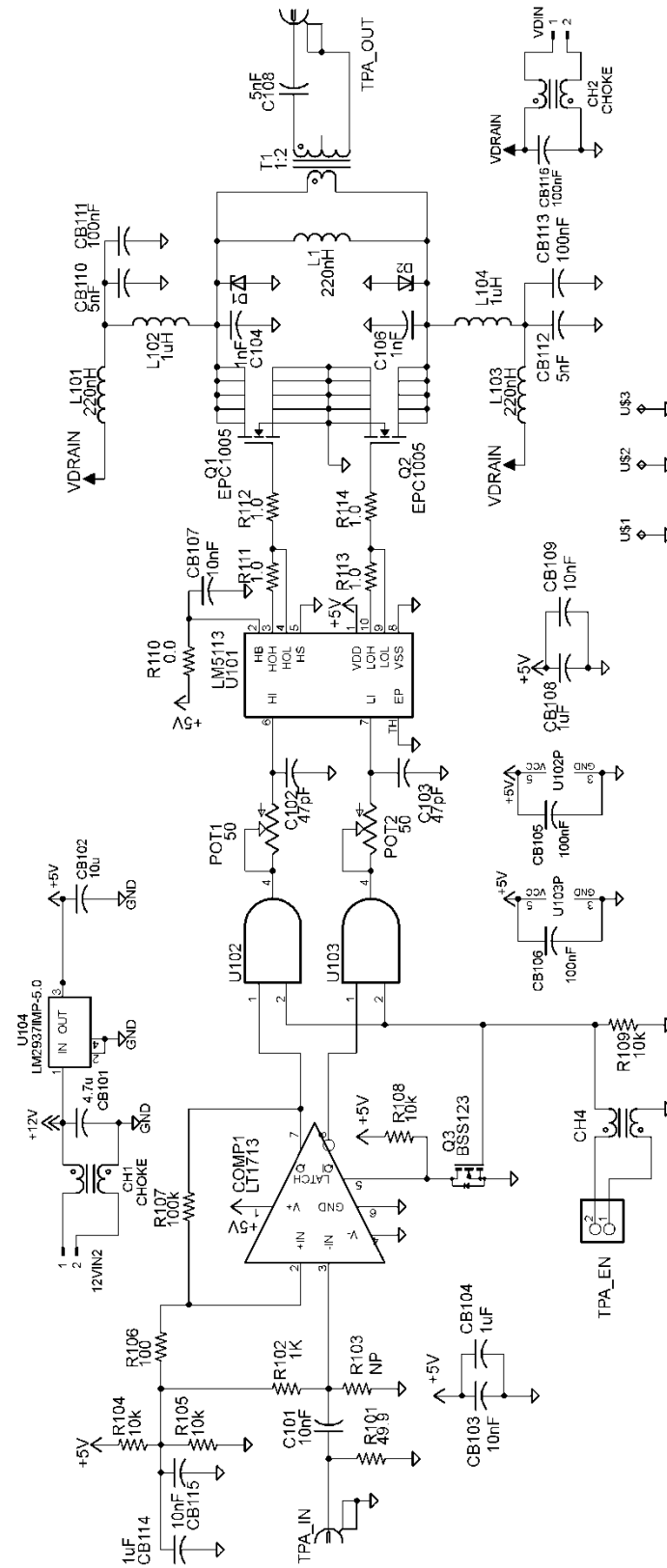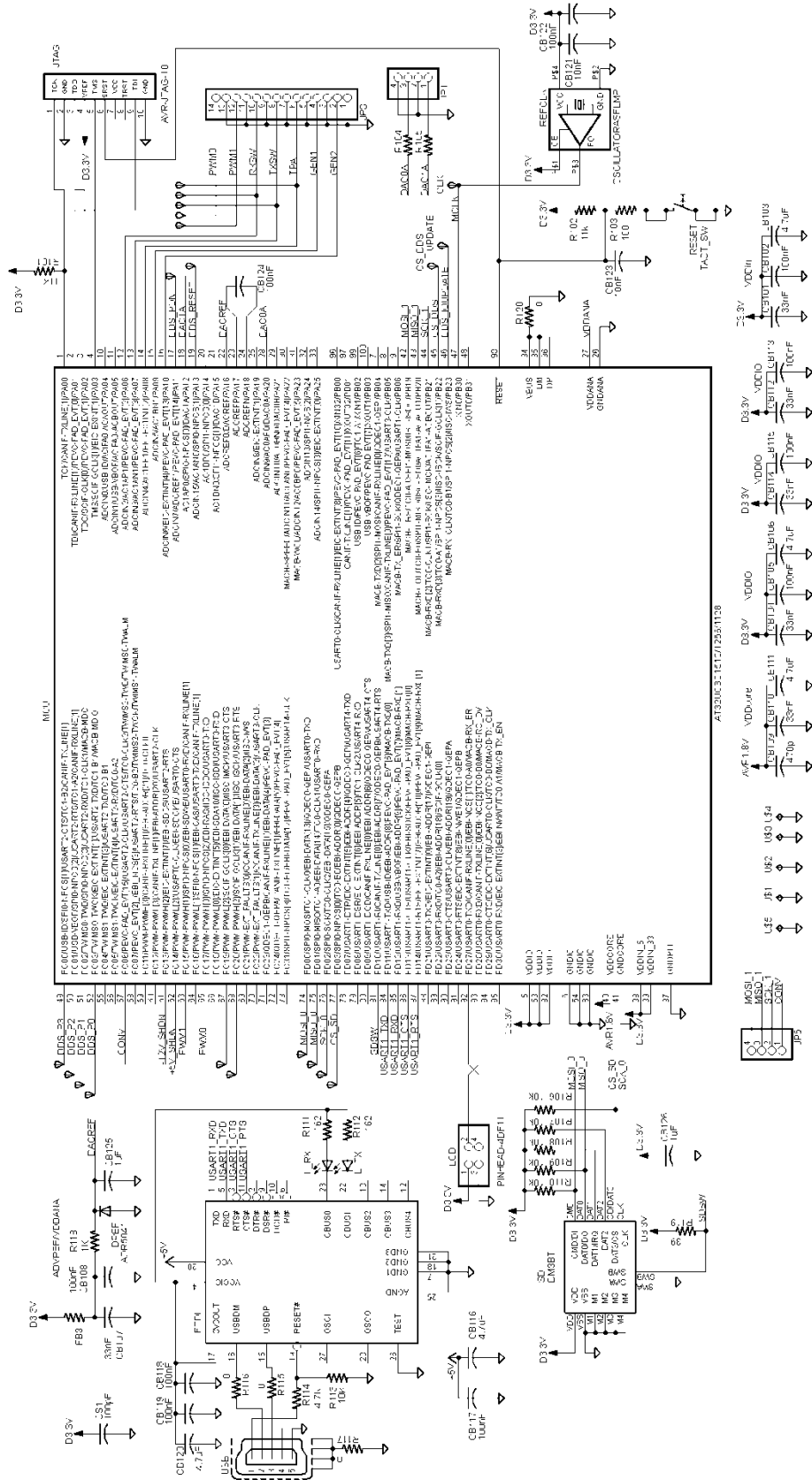
Buck Modulator schematic

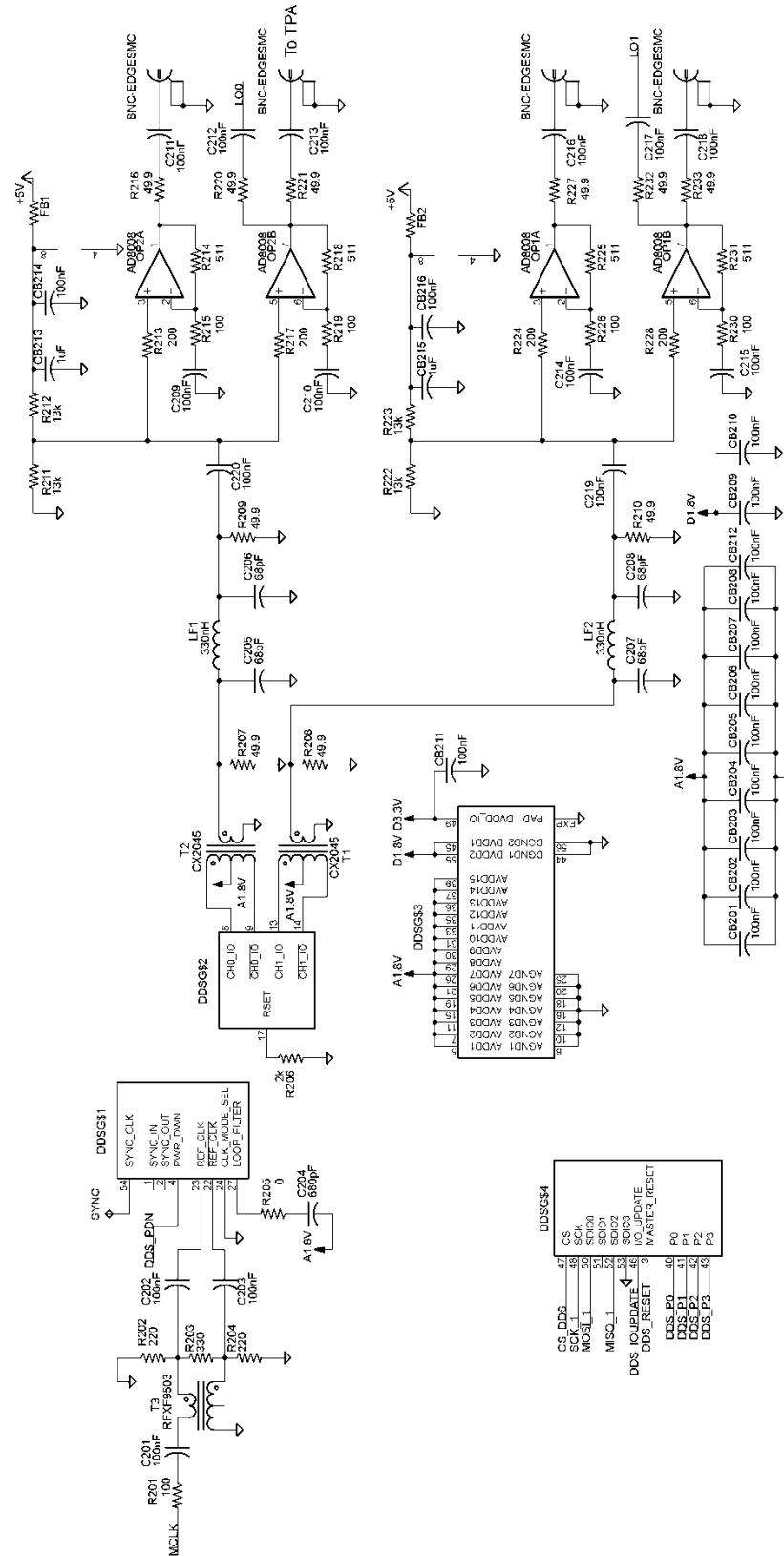# RF amplifier schematic, part A

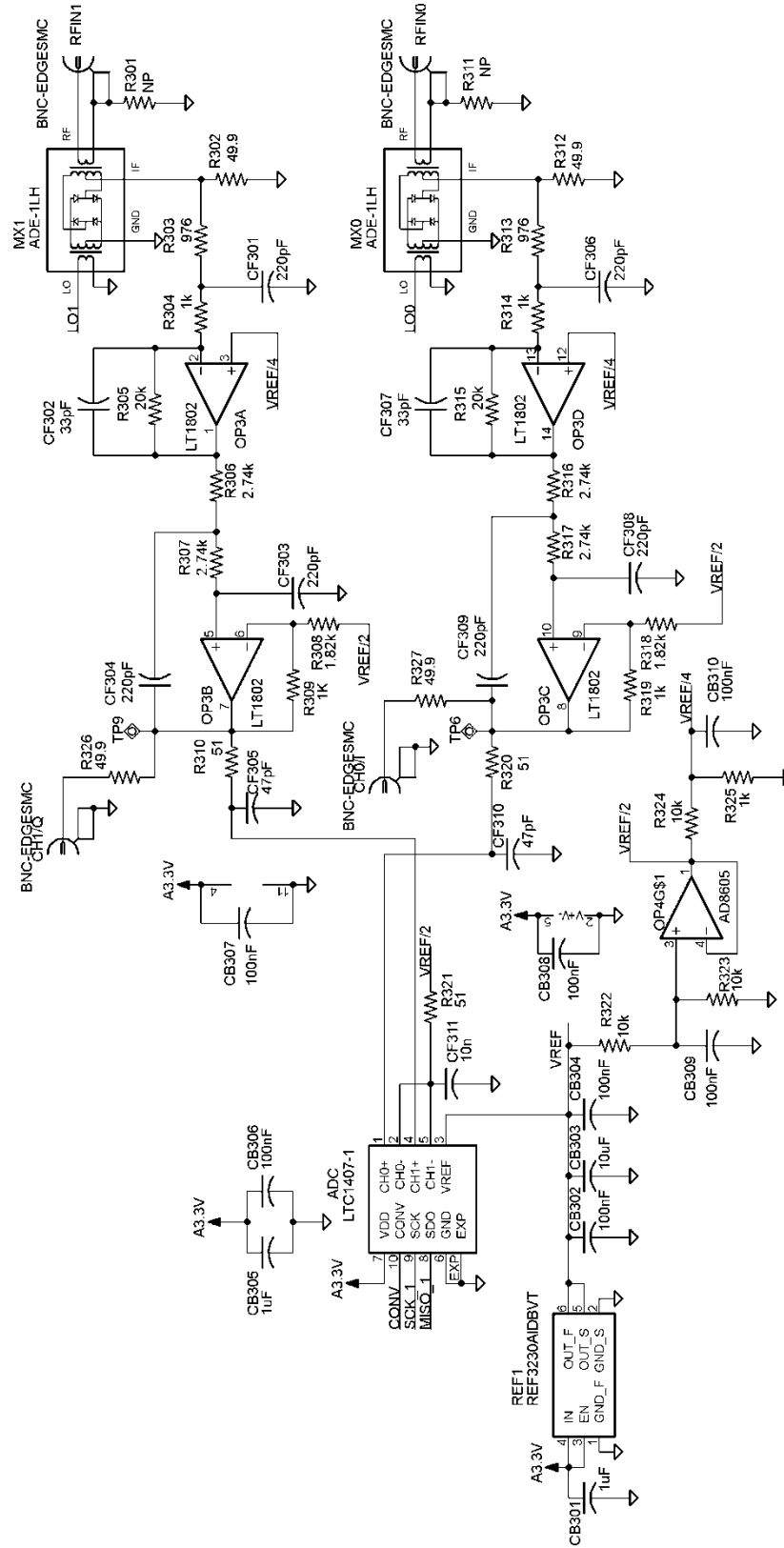**RF amplifier schematic, part B**

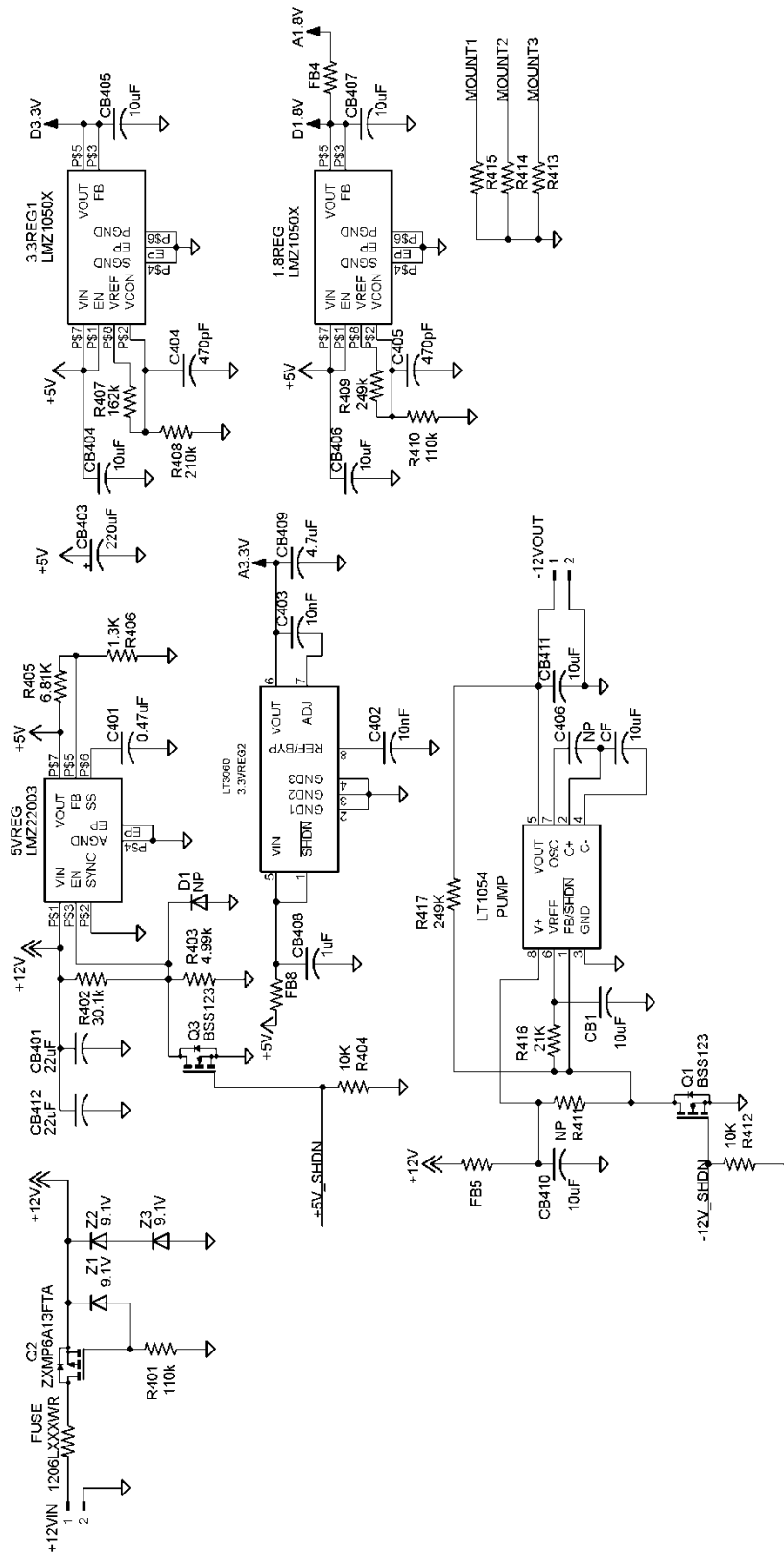# Control board schematic, part A (MCU and interface)

Control board schematic, part B (DDS)

Control board Schematic, part C (mixers, baseband, and ADC)

Control board schematic, part D (Power conditioning)

Bibliography

[1]   M. Twieg, "Low Cost NMR Development," Jul-2012. [Online]. Available: http://ccir.case.edu/Research/mri/lowcostmr/V2intropage. [Accessed: 09-Jul-2012].

[2]   B. Blümich, F. Casanova, J. Perlo, S. Anferova, V. Anferov, K. Kremer, N. Goga, K. Kupferschläger, and M. Adams, "Advances of unilateral mobile NMR in nondestructive materials testing," *Magn Reson Imaging*, vol. 23, no. 2, pp. 197–201, Feb. 2005.

[3]   K. Kremer, B. Blümich, F.-P. Schmitz, and J. Seitzer, "Nondestructive Testing of Adhesive Curing in Glass–Metal Compounds by Unilateral NMR," in *Adhesion*, W. Possart, Ed. Wiley-VCH Verlag GmbH & Co. KGaA, 2006, pp. 435–443.

[4]   Bruker Optics, "Solid Fat Content (TD-NMR)," 2012. [Online]. Available: http://www.brukeroptics.com/solidfat.html. [Accessed: 21-Jun-2012].

[5]   H. Stork, A. Gädke, and N. Nestle, "Single-sided and semisingle-sided NMR sensors for highly diffusive samples: application to bottled beverages," *J. Agric. Food Chem.*, vol. 54, no. 15, pp. 5247–5252, Jul. 2006.

[6]   M. Flaum, "Fluid and rock characterization using new NMR diffusion-editing pulse sequences and two dimensional diffusivity-T2 maps," 2007. [Online]. Available: http://hdl.handle.net/1911/20607.

[7]   D. G. Rata, F. Casanova, J. Perlo, D. E. Demco, and B. Blümich, "Self-diffusion measurements by a mobile single-sided NMR sensor with improved magnetic field gradient," *J. Magn. Reson.*, vol. 180, no. 2, pp. 229–235, Jun. 2006.

[8]   A. Guthausen, G. Guthausen, A. Kamlowski, H. Todt, W. Burk, and D. Schmalbein, "Measurement of fat content of food with single-sided NMR," *Journal of the American Oil Chemists' Society*, vol. 81, no. 8, pp. 727–731, 2004.

[9]   Oxford Instruments, "Measurement of Oil and Moisture in Seeds According to ISO 10565." 2009.

[10]   N.-O. Goga, "Non-destructive characterization of materials by single-sided NMR," Disseration, Rheinisch-Westfälische Technische Hochschule Aachen, 2007.

[11]   E. M. Haacke, R. W. Brown, M. R. Thompson, and R. Venkatesan, *Magnetic Resonance Imaging: Physical Principles and Sequence Design*, 1st ed. Wiley-Liss, 1999.

[12]   D. . Hoult and P. C. Lauterbur, "The sensitivity of the zeugmatographic experiment involving human samples," *Journal of Magnetic Resonance (1969)*, vol. 34, no. 2, pp. 425–433, May 1979.

[13]   E. M. Purcell, H. C. Torrey, and R. V. Pound, "Resonance Absorption by Nuclear Magnetic Moments in a Solid," *Phys. Rev.*, vol. 69, no. 1–2, pp. 37–38, Jan. 1946.

[14]   F. Bloch, "Nuclear Induction," *Phys. Rev.*, vol. 70, no. 7–8, pp. 460–474, Oct. 1946.

[15]   E. L. Hahn, "Nuclear Induction Due to Free Larmor Precession," *Phys. Rev.*, vol. 77, no. 2, pp. 297–298, Jan. 1950.

[16]   E. L. Hahn, "Spin Echoes," *Phys. Rev.*, vol. 80, no. 4, pp. 580–594, Nov. 1950.

[17]   H. Y. Carr and E. M. Purcell, "Effects of Diffusion on Free Precession in Nuclear Magnetic Resonance Experiments," *Phys. Rev.*, vol. 94, no. 3, pp. 630–638, May 1954.

[18]   Casieri, S. Bubici, and F. De Luca, "Self-diffusion coefficient by single-sided NMR.," *Journal of Magnetic Resonance*, vol. 162, no. 2, pp. 348–355, 2003.

[19]   J. Perlo, F. Casanova, and B. Blümich, "Profiles with microscopic resolution by single-sided NMR," *J. Magn. Reson.*, vol. 176, no. 1, pp. 64–70, Sep. 2005.

[20]   Oxford Instruments, "Determination of Solid Fat Content in Edible Oils and Fats by the Official Direct Method (AOCS Cd 16b-93)." 2009.

[21]   D. Meeker, "Finite Element Method Magnetics," 24-Jun-2011. [Online]. Available: http://www.femm.info/wiki/HomePage. [Accessed: 10-Jul-2012].

[22]   S. Anferova, V. Anferov, M. Adams, P. Blümler, N. Routley, K. Hailu, K. Kupferschläger, M. j. d. Mallett, G. Schroeder, S. Sharma, and B. Blümich, "Construction of a NMR-MOUSE with short dead time," *Concepts in Magnetic Resonance*, vol. 15, no. 1, pp. 15–25, 2002.

[23]   I. P. Gerothanassis, *Methods of Avoiding the Effects of Acoustic Ringing in Pulsed Fourier Transform Nuclear Magnetic Resonance Spectroscopy*. Pergamon Press, 1987.

[24]   Microsemi Corp., "The PIN Diode Circuit Designer's Handbook." 1998.

[25]   M/A-COM Technology Solutions, "Establishing the Minimum Reverse Bias for a PIN Diode in a High-Power Switch." .

[26]   N. O. Sokal, "RF power amplifiers, classes A through S-how they operate, and when to use each," in *Electronics Industries Forum of New England, 1997. Professional Program Proceedings*, 1997, pp. 179 –252.

[27]   N. Gudino, M. Riffe, J. Heilman, and M. Grizwold, "1.5T On-Coil Current-Mode Class-D (CMCD) Amplifier with Amplitude Modulation Feedback and Voltage-Mode Class-D (VMCD) Preamplifier," presented at the ISMRM, 2010.

[28]   A. Lidow, J. Strydom, M. de Rooij, and Y. Ma, "EPC Transistors for Efficient Power Conversion." Power Conversion Publications, 2012.

[29]   H. T. Friis, "Noise Figures of Radio Receivers," *Proceedings of the IRE*, vol. 32, no. 7, pp. 419 – 422, Jul. 1944.

[30]   B. P. Lathi, *Modern Digital and Analog Communication Systems*, 3rd ed. Oxford University Press, USA, 1998.

[31]   R. SONI and E. NEWMAN, "The benefits of direct-conversion receiver designs," *Electronic Products*, 01-Jun-2009.

[32]   Meiboom and D. Gill, "Modified Spin-Echo Method for Measuring Nuclear Relaxation Times," *Review of Scientific Instruments*, vol. 29, no. 8, p. 688, 1958.

[33]   M. D. Hürlimann and D. D. Griffin, "Spin dynamics of Carr-Purcell-Meiboom-Gill-like sequences in grossly inhomogeneous B(0) and B(1) fields and application to NMR well logging," *J. Magn. Reson.*, vol. 143, no. 1, pp. 120–135, Mar. 2000.

[34]   M. Klein, R. Fechete, D. E. Demco, and B. Blümich, "Self-diffusion measurements by a constant-relaxation method in strongly inhomogeneous magnetic fields," *J. Magn. Reson.*, vol. 164, no. 2, pp. 310–320, Oct. 2003.

[35]   M. A. Bernstein, K. F. King, and X. J. Zhou, *Handbook of MRI Pulse Sequences*, 1st ed. Academic Press, 2004.

[36]   D. Purdy, "A Simple Equation for the Evaluation of T1 and T2 from Absolute Value MR Images," *SMRM*, vol. 2, pp. 514–515, Aug. 1986.

[37]   Bruker Corporation, "Bruker Almanac 2012." 2012.